

Wireless Electromyogram System for the Shoulder

A Major Qualifying Project submitted to the Faculty of WORCESTER POLYTECHNIC INSTITUTE in partial fulfillment of the requirements for the Degree of Bachelor of Science

Submitted by:

Julia Antocci

Thomas Flanagan

Max Kanefsky

Timothy Walsh

Advised by: Professor Edward A. Clancy

December 2023



This report represents work of one or more WPI undergraduate students submitted to the faculty as evidence of a degree requirement. WPI routinely publishes these reports on its web site without editorial or peer review.

Acknowledgments

The team would like to personally thank:

Professor Edward Clancy, the project advisor, for his contributions and support towards the success of this project. His guidance, feedback, and materials his lab provided made the project possible.

Kiki Rajotte and Marc Rosenthal for their generous technical support they provided over the course of the project duration.

Abstract

This project analyzes the feasibility of a wireless electromyogram (EMG) shoulder sleeve that monitors four shoulder muscles and transmits data to a peripheral monitor. A system was created that attaches four EMG electrodes to a compression shirt and, with the help of analog circuitry, Nordic nRF52840 microcontrollers, and MATLAB, the EMG signals are sent via Bluetooth low energy (BLE) to a PC and processed into viewable data off-line. Through the development and collection of data for each component of this system, alternate studies were completed on viable options for future EMG systems, including the use of a 24-bit ADC and alternate power supply options. Our results demonstrated a feasible wireless EMG shoulder system, but several areas of improvement can be completed to better optimize for a wireless device.

Executive Summary

This paper discusses the development and learning outcomes for a 4-channel wireless EMG and mechanical measurement system designed for short-term use for shoulder rehabilitation. The project combines 4 EMG electrode channels onto a shoulder sleeve package that wirelessly transmits data to a peripheral computer for data collection.

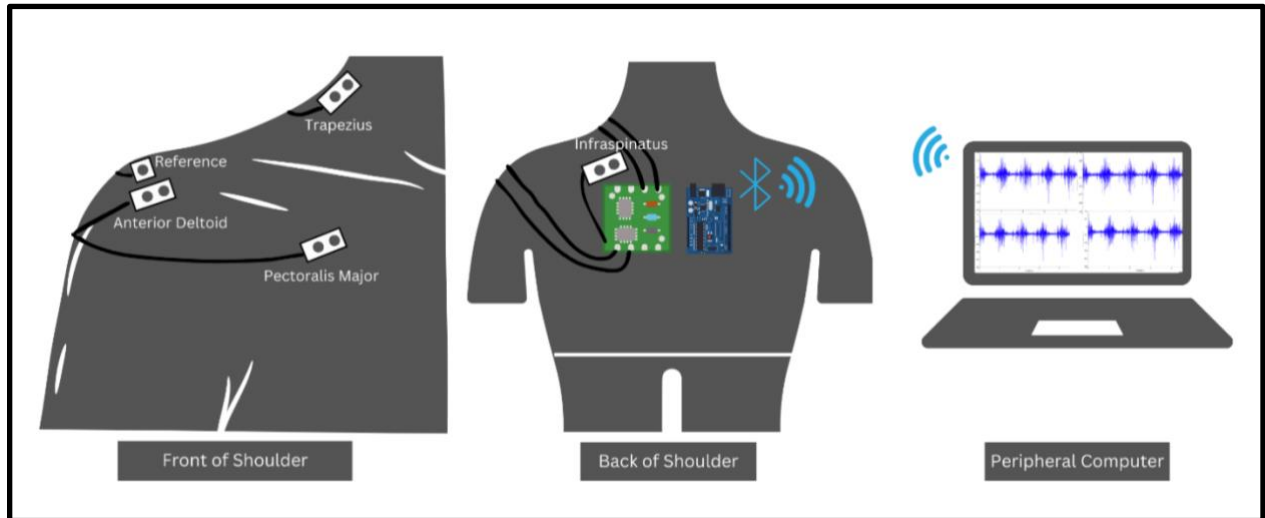


Figure 1: Shoulder EMG System Diagram With Bipolar Electrodes

The device collects EMG data from four major muscles in the shoulder region: the trapezius, pectoralis major, infraspinatus, and anterior deltoid. To do so, an analog EMG front end was created and duplicated for each channel. The design created consists of an instrumentation amplifier, a high and low pass second order filter, and various stages for gain customizable through switches. The front end was prototyped and investigated using a breadboard and then assembled on a solder board for the final 4 channels used in the device. The block diagram below, followed by a photo of the prototype solder board, shows the sequence of analog stages to obtain an analog EMG signal ranging from 0-3.6 V.

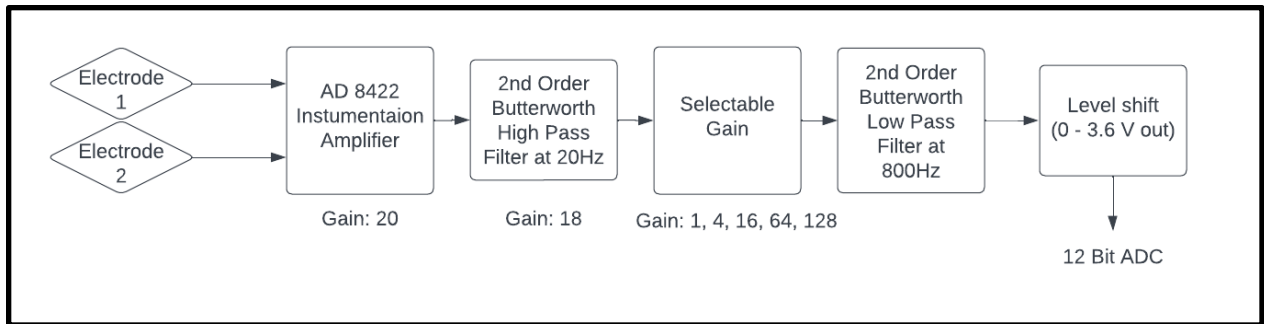


Figure 2: EMG Front end block diagram

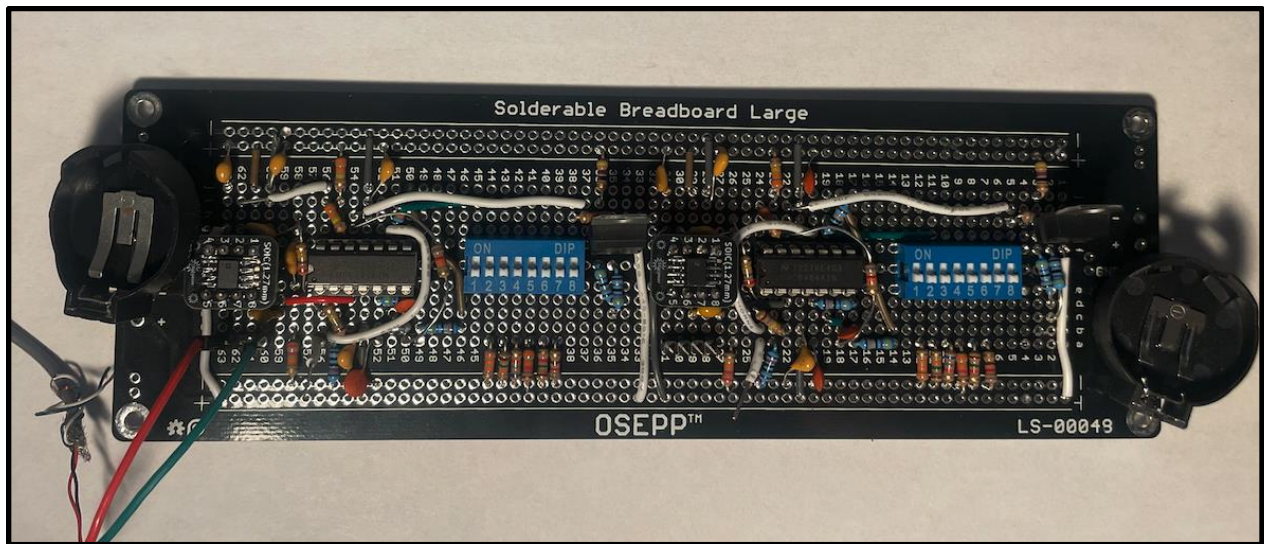


Figure 3: One of two EMG front-end solder boards (2 channels).

Each of the two EMG front-end solder boards houses two EMG channels. Therefore, the implemented analog design successfully created 4 EMG channels meeting all requirements set, including selectable gain for all channels between 360 - 46,000. Through testing and data collection, however, areas of improvement were recognized for future research. An alternative level shifter to the voltage regulator was found to be significantly more power efficient after later tests. In addition, using a charge pump with constant outputs would have produced a bipolar supply of sufficient value for our purposes while using only one of the two coin cell batteries used in the existing circuit.

For data sampling and wireless transmission, a Nordic nRF52840 microcontroller unit (MCU) was used to acquire and digitize these analog signals. This microcontroller received a signal between 0 - 3.6 V, which makes up the full range of the analog-to-digital converter

(ADC). The device was programmed through the Segger Embedded Studio and benefitted from scripts written in previous research. One of these MCUs was placed on the shoulder device (peripheral), while the second (central) was connected to a computer nearby where data were received through Bluetooth. The programming of the microcontroller unit successfully was implemented to receive up to 5 ADC channels sampled at a 2 kHz sampling rate.

All pieces to the project were then combined onto a shoulder sleeve made of a compression shirt and included 4 EMG electrodes connected to each front-end circuit. Each piece of the system was tested individually and then together as a system once integrated. The EMG front-end successfully passed EMG signals with a frequency range of 20 - 800 Hz and provided gains selectable between 360 - 46,000. The figure below shows the frequency response from the system with a minimum gain of 360.

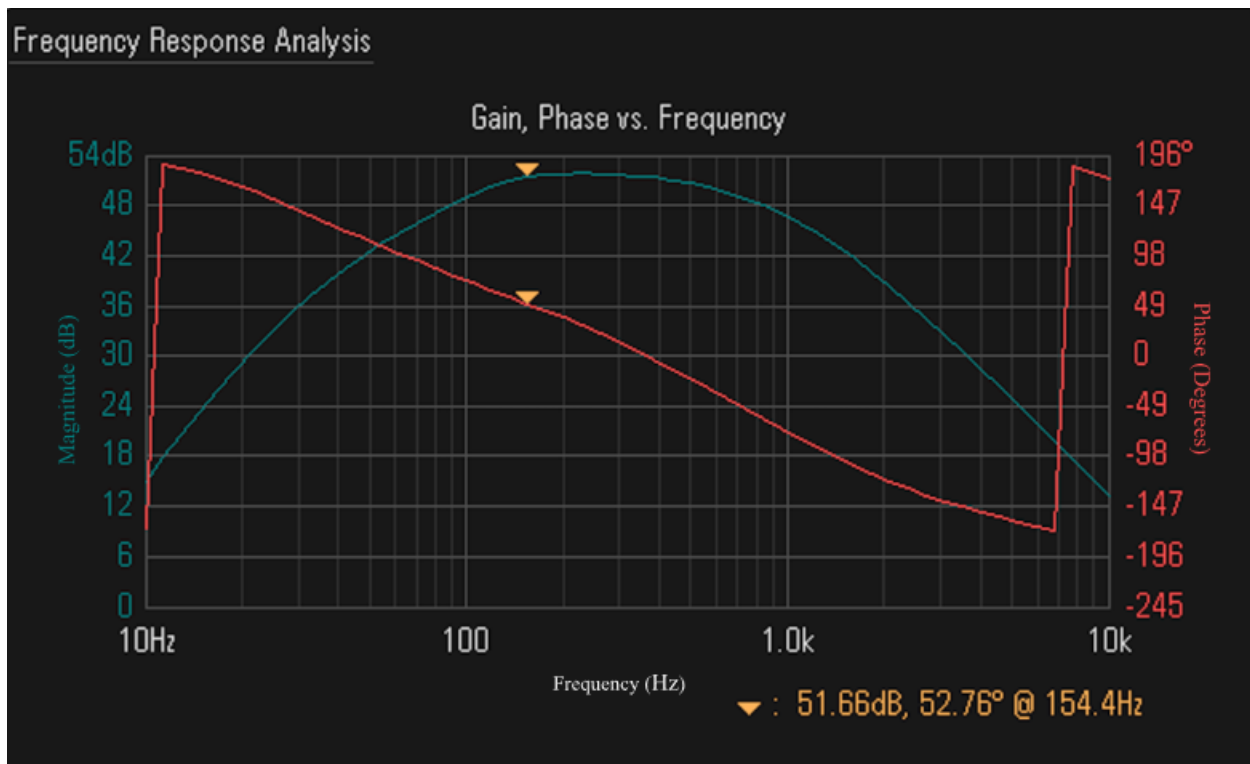


Figure 4: Instrumentation amplifier and bandpass filter circuit frequency response.

With the front end, BLE microcontroller, and compression shirt integrated together, the completed device can acquire EMG from four shoulder muscles of a subject. Figure 5 shows the device and its components in use on a subject.



Figure 5: EMG shoulder sleeve in-use on subject.

Throughout the design process, many decisions and tradeoffs were made on the basis of too many unknowns. As a side portion of this project, an alternate design was considered of using an ADS1292ECG-FE integrated circuit in replacement of many analog components, and the consideration of using a 24-bit ADC, in contrast to the chosen 12-bit converter. For this comparison, an analysis on whether the ADS1292ECG-FE can be used for an EMG application, noise testing, effective number of bits and power spectral density calculations were done. The analysis using an ADS1292ECG-FE evaluation board showed that it can be used for an EMG application for 2 channels with an additional gain stage added on. The noise when compared to the main design option was lower additionally, the effective number of bits was calculated to be about 18 bits, which is two extra bits from common 16-bit design options. These additional bits can be used for an additional gain stage of 4. These specifications along with the quality of the software, size and cost of the board, and limitations of the board were considered when comparing the main design option and using a 24-bit analog to digital converter.

Overall, there were many advantages and disadvantages which make it a hard decision on whether using the ADS1292ECG-FE integrated circuit or a 24-bit ADC would have been a better

option. For this project, the priority was getting a complete product built and it being wireless. Before the project, this option was ruled out due to the lack of experience and knowledge of the ADS1292ECG-FE integrated circuit. After doing the project, since there are still some unknowns due to noisy equipment used in testing, the main design option is still the better design option over the ADS1292ECG-FE integrated circuit. Although after some additional noise testing to find the true noise floor of the system, the noise of the function generator could be significant enough to decrease the measurement of effective number of bits. If this is the case, the true effective number of bits could be 20 bits. If such is the case, then using a 24-bit analog to digital converter is the better option since selectable gain stages would not be needed. Those extra bits could lead to an additional gain stage of 32 which makes the overall selectable gain of the ADC equal 384 which meets our minimum requirement.

The conclusion of this project verifies an EMG wireless shoulder device as a viable device for shoulder muscle monitoring. The EMG front-end created a feasible implementation that meets minimum requirements, while also providing refinements for further advancement. The wireless capabilities and data sampling were proven to work for at least 5 channels and a deeper understanding of how the inner workings were understood. This project sets a path for a more refined and complete EMG shoulder device and reveals the specific drawbacks to consider if an integrated circuit, such as the ADS 1292 were used in the future.

Table of Contents

Acknowledgments	2
Abstract	3
Executive Summary	4
Table of Contents	9
1. Introduction	13
2. Background	15
2.1 ECG and EMG	15
2.1.1 ECG Signals	15
2.1.2 EMG Signals	15
2.2 Why EMG?	18
2.3 Shoulder and Upper Arm Muscles	18
2.2.1 General Movements and Keeping Electrodes in Place	20
2.4 EMG Acquisition Circuits	24
2.5 Bipolar vs Unipolar Leads for Front End Design of ECG	25
2.5.1 Bipolar Leads	25
2.5.1.1 Limb Leads	25
2.4.1.2 Augmented Limb Leads.....	26
2.5.1.3 Bipolar Leads for EMG	26
2.5.2 Unipolar Leads	26
2.5.2.1 Precordial Leads.....	27
2.6 Analog Front End of EMG Systems	27
2.6.1 Operational Amplifiers (Op-Amps)	29
2.6.2 EMG Amplification	31
2.6.2.1 The Instrumentation Amplifier	32
2.6.3 Filtering	33
2.6.3.1 Low Frequency Noise	34
2.6.3.2 High Frequency Noise	35
2.7 Range of Motion and Inertial Measurement Units	36
2.7.1 Goniometers	37
2.8 Microcontroller Overview	38
2.8.1 ADC Limitations	39
2.8.2 Nordic Microcontroller	40

2.8.2.1 ADC Information	40
2.8.2.2 BLE Information	40
3. Design Options	41
3.1 System Requirements and Design Options	41
3.2 EMG Front End	43
3.2.1 EMG Analog Front End Design Option 1	44
3.2.1.1 Instrumentation Amplifier	44
3.2.1.2 Filtering	45
3.2.1.3 Gain	45
3.2.2 EMG Front End Design Options 2.....	46
3.2.3 EMG Front End Design Option 3	47
3.2.3.1 ADS1292ECG-FE Integrated Circuit Description and Application	47
3.2.3.2 Specifications	48
3.2.3.3 Noise Comparison.....	48
3.3 IMU Measurements.....	50
3.3.1 Flex Sensor	50
3.3.2 Accelerometer	50
3.4 Microcontroller.....	51
3.4.1 Sampling rate	52
3.5 Power Supply	52
3.6 Shoulder Sleeve/Strap.....	54
4. Design Selection.....	56
5. EMG Front End	58
5.1 Methods	58
5.2 Instrumentation Amplifier Circuit	59
5.2.1 Common Mode Rejection Ratio (CMRR)	63
5.2.2 Noise	64
5.3 High and Low Pass Filters.....	64
5.4 Selectable Gain	68
5.5 Level shifter	70
5.5.1 Future Improvements.....	71
5.6 Front-End EMG Acquisition.....	79
5.7 Power Performance.....	82
5.8 Front End Discussion	85

5.8.1 Alternative Power Supply System	86
6. ADS 1292 Study Results	91
6.1 Ordering and Software Installation	91
6.1.1 Creating a Texas Instruments Account	91
6.1.2 Downloading Software	91
6.2 Problems with Installation	92
6.2.1 USB Driver Not Properly Installed	92
6.2.2 How USB Driver Problems Were Fixed	92
6.3 Functioning Software and Early Testing	94
6.3.1 GUI of ADS1x9xEVM Software	94
6.3.2 Connecting to Function Generator and Results	95
6.4 EMG Application	97
6.4.1 Instrumentation Amplifier	97
6.4.1.1 Overview.....	97
6.4.1.2 Advantages and Disadvantages of Increasing Gain.....	98
6.4.1.3 Voltage Noise Testing.....	98
6.4.2 Voltage Divider	100
6.4.3 Effective Number of Bits (ENOB)	103
6.4.3.1 Definition.....	103
6.4.3.2 Calculations.....	103
6.4.3.3 Results.....	105
6.4.4 Power Spectral Density (PSD)	108
6.4.4.1 Definition and Calculation.....	108
6.4.4.2 Results.....	108
6.5 ADS1292 Discussion	109
6.5.1 Limitations	109
6.5.2 What Could Have Been Done Better	110
6.5.3 Comparison to 24-bit ADC	111
6.5.4 Additional Noise Testing	112
7. Microcontroller Results	115
7.1 Software overview	115
7.1.1 Microcontroller applications	115
7.1.2 Data processing script	116
7.2 Initial testing	116

7.2.1 DC voltage input	116
7.2.2 Wave input	117
7.3 Adaptation of the software for the task	118
7.3.1 Multiple ADC channels	118
7.3.2 Further optimization	120
7.4 Integration with analog front-end	123
8. Shoulder System Integration	125
9. System Discussion	127
10. Conclusion	129
Appendix A	130
Appendix B	135
Appendix C	136
Appendix D	137
Appendix E	141
References	145

1. Introduction

The shoulder joint is known to be the most mobile joint in the human body and its surrounding muscles support these movements. The muscles of particular interest in the shoulder and upper arm region are the deltoid, supraspinatus, infraspinatus, and subscapularis muscles (Edwards et al., 2021). Due to the amount of rotation and translation of the shoulder joint, it has more potential for injury with respect to the shoulder joint compared to any other joint and supporting muscles in the human body (Chang et al., 2023). In the United States there are more than 500,000 surgeries performed on the shoulder joint (Freehill et al., 2023, Page 1). These surgeries include but are not limited to shoulder joint replacements and rotator cuff tear repairs. Such injuries and surgery recoveries raise the need for doctor as well as physical therapy appointments for upwards of a few months or longer. Therefore, each of these patients have the potential to benefit from our shoulder and arm muscle monitoring device.

The basic idea for this MQP came from seeking a solution to these two issues. Our goal was to design and prototype a sleeve for the shoulder implemented with wireless sensors to monitor the electrical activity of the shoulder and upper arm muscles along with a mechanical parameter of shoulder motion. Such mechanical parameters can include information such as acceleration, gyroscopic motion and magnetic fields, but the parameter of focus is the angle of the shoulder joint. However, the main focus is monitoring the electrical activity of the muscles associated with shoulder and upper arm movement in a way that can be done from home. This device will be completely wireless, being powered by an on-board power source, and all data wirelessly transmitted to a monitoring device.

Monitoring of the electrical activity of muscles is known as electromyography or EMG (Johns Hopkins University et al., 2023, Para. 1). While this type of monitoring is further discussed later in this report, the end goal is a functioning design which can be used from home. Therefore, it is important to note that this test in a clinical setting could use sticky electrodes that adhere to the skin but is not a viable option for at-home. Invasive needle electrodes are even more common in EMG applications as compared to ECG, but this method is also not a viable option for at-home use. In order to have a product of this sort that is ready and suitable for at-home use, the number of non-reusable and moveable parts should be limited - if there are any to

begin with. While any electrode placement is dependent on the exact patient in need of these services, the electrode placement should originally be verified by a clinician to ensure accurate readings. However, stick-on-surface electrodes are generally one time use and are not an easy tool for patients to use themselves since many will not know the proper placement to use. One time use components also add to the cost of the final product over time making it a less desired option to use by a patient. Companies producing such products like one-time use devices as customers must spend more in order to continue using the product. For the purposes of this project, one-time use components are undesirable, and a reusable product is best for an individual patient in terms of money and ease of use. While our project focused on monitoring of non-infectious disabilities, one patient having access to a reusable product also lowers the risk of spreading germs or diseases in other applications.

Our approach is to use a compression shirt attached to four EMG channels, with the additional help of an analog front end and Bluetooth microcontroller, to wirelessly transmit EMG data for four muscles at once. This solution can wirelessly transmit EMG data received on a peripheral device and was further designed to be customizable to individual subjects. Based on our research, we learned that certain components of the project have a much larger and more impact on the overall power consumption and physical footprint of the system that we had originally thought. Such components and design choices can be altered in the future to better accommodate a wireless device.

2. Background

2.1 ECG and EMG

The electrocardiogram (ECG) is the electrical activity of one's heart (Johns Hopkins University et al., 2021). The electromyogram (EMG) is the electrical activity of skeletal muscle, (Johns Hopkins University et al., 2023, Para. 1). EMG tests can be used to monitor many other muscles including those of the arms and legs (Mayfield Clinic, 2018, Para. 8). The focus of this project is EMG, particularly with respect to upper arm and shoulder muscles, however it is important to understand both of these signals since many of the principles used to obtain and evaluate the information are the same. In addition, signals are acquired using very similar electronic components and ECG signals can easily contaminate EMG signals (Chang et al., 2022). Due to this overlap, ECG instrumentation as well as literature can be very useful to EMG applications with slight modifications which will help to close the gap in EMG instrumentation and literature.

2.1.1 ECG Signals

While ECG signals are not the focus of this project, it is still important to note a few key features of these signals. ECG signals measured on the surface of the skin have amplitudes between one and five millivolts before amplification and are generally within the frequency range between 0.05 Hz and 100 Hz (Jamaluddin et al., 2014). However, the majority of this power is below 30 Hz (Murthy et. al., 1978). As mentioned above, the frequency range is one feature that overlaps with that of EMG signals allowing some ECG to create extra noise in EMG signals.

2.1.2 EMG Signals

In general, EMG is created by the contraction and movement of muscles and muscle fibers in the body. These contractions create an electrical signal (BionIT Labs, 2023). Because of this relationship between EMG signal and muscle contraction, EMG can only be measured while the muscle is contracting and not while the muscle is relaxed. EMG can be measured using one

of two main methods; surface electrodes or indwelling (needle or wire) electrodes. It is common for one method or the other to be used, but both can be used in the same test depending on the muscle in question. However, the orientation of the electrodes with respect to the muscle fiber is important to the measurement of surface EMG because the electrodes must be able to sense the signal as it travels through the muscle fibers. Therefore, the best way to place surface electrodes is in parallel with the muscle fibers because that setup allows for the measurements of the action potentials traveling along the muscle fibers (Ng et al., 1998, Page 1). EMG action potential signals do not flow perpendicular to the direction of muscle fibers. An example of proper electrode alignment can be found in Figure 2-4 below.

Motor units (MUs) are comprised of the motor nerve itself along with each of the muscle fibers involved in the transmission of a given motor unit action potential (MUAP) from that motor unit. The electrical activity from each motor unit is superimposed with the others to create a surface EMG signal (Raez et al., 2006). The action potentials associated with each motor unit are combined and result in MUAPs. EMG signals are made up of motor unit action potentials which vary in shape and occurrence rate depending on the specific muscle being tested and the effort associated with the level of muscle contraction that occurs. These characteristics are also highly dependent on each particular patient. After a particular nerve has been activated, in a healthy patient, each of the muscle fibers in the motor unit will also activate.

Each MUAP provides the information associated with the electric potential being conducted in the muscle tissue at the time of measurement (Raez et al., 2006). When EMG is measured from the surface of the skin, the EMG measurement contains many of these action potentials as they are measured from many motor units at once. Individual action potentials and motor units are fired at irregular intervals and the signal is either a positive or negative voltage at any given time (Raez et al., 2006). Due to this random timing of the motor units, many tend to be recorded by standard surface electrodes at any given time resulting in what looks like a random signal.

An example of a characteristic MUAP as recorded by surface EMG electrodes is shown in Figure 2-1 below.

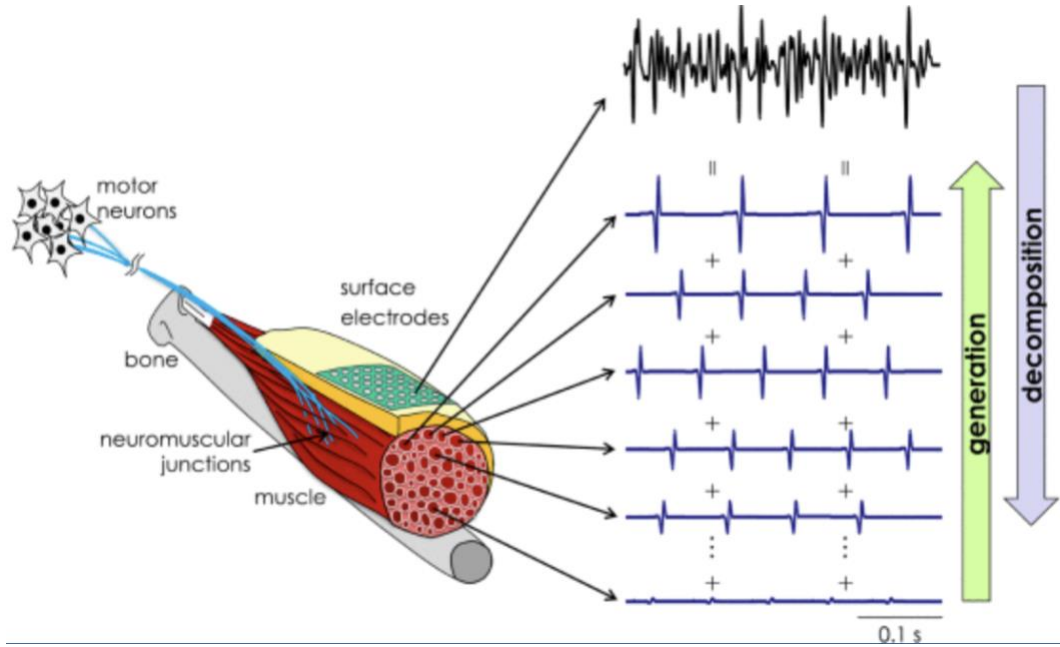


Figure 2-1: Characteristic MUAP Surface EMG Signal Generation and Decomposition (Farina & Holobar, 2016)

In general, an extremely simple surface EMG signal representation is provided by the following equation:

$$x(n) = [\sum_{r=0}^{N-1} h[r]e[n-r]] + w[n] \quad (\text{Eq. 2-1})$$

In this case, $x(n)$ is the modeled signal, $e(n)$ is an impulse train representing the firing times, $h(r)$ is the MUAP, $w(n)$ is the additive noise (typically modeled as zero mean, white and Gaussian distributed), r is the firing times and n is the number of motor unit firings (Raez et al., 2006, Page 3). However, this would be the equivalent of a single motor unit being measured. A true EMG signal would be a sum of many summations of Eq. 2-1, as seen in Eq. 2-2.

$$x_m(n) = \left[\sum_{r=0}^{N-1} h_1[r]e_1[n-r] + h_2[r]e_2[n-r] + h_m[r]e_m[n-r] \right] + w[n]$$

where $m = 1, 2, \dots M$ of motor units recorded (Eq. 2-2)

Surface EMG signals tend to have an amplitude range between one and ten millivolts before any amplification occurs and are found within the frequency range between 20 Hz and

800 Hz (Raez et al., 2006) and (Jamaluddin et al., 2014). In addition, the recommended sampling rate is 2000 Hz, especially in research and academics such as this MQP (Gallina et al., 2022). A sampling rate of 2000 Hz is recommended as you want to sample well above the minimum sampling rate ($2 \times$ maximum signal frequency, which would also be significantly higher than the Nyquist rate and helps to avoid aliasing in the signal (McManus et al., 2020, Para. 30).

2.2 Why EMG?

As previously mentioned, EMG tests are used to aid in the maintenance of recovery from operation or injury. The information collected by conducting an EMG test can include parameters such as the strength of each signal, general function or potential dysfunction of motor neurons, and potential issues with signal transmissions from the nerve to the muscle (Mayo Clinic Staff, 2019). If EMG could be used from home to monitor one's upper arm and shoulder muscles after an injury it would be helpful to more people than it may first seem. Between two and four million people living in the United States each year are affected by some form of rotator cuff injury in need of repair, healing and maintenance (HSS Physicians, 2019).

2.3 Shoulder and Upper Arm Muscles

Before any muscular test can be performed, it is important to note which muscles are most likely to be involved and where they are located. Figures 2-2 and 2-3 provide labeled diagrams of the shoulder and upper arm to reference as EMG and its applications are discussed further.

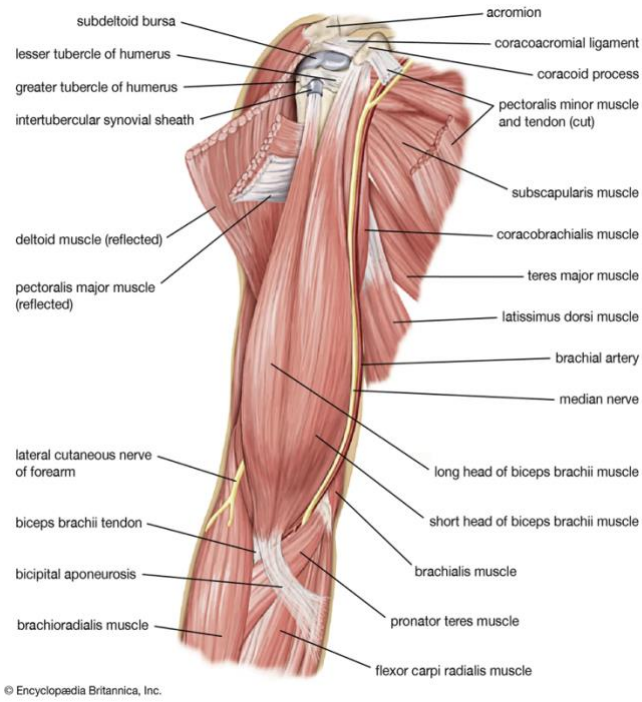


Figure 2-2: Anatomy of the Shoulder Muscles (Right Shoulder) (Crompton et al., 2023)

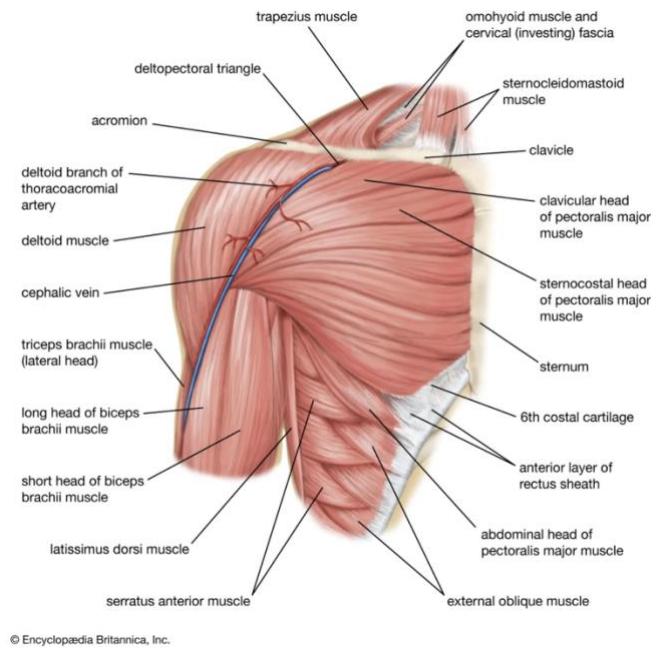


Figure 2-3: Anatomy of the Upper Arm Muscles (Right Shoulder) (Crompton et al., 2023)

In EMG applications, the muscles of particular interest vary based on the exact purpose of the test and condition of the patient. However, it is common to consider the deltoid, supraspinatus, infraspinatus, and subscapularis muscles during shoulder and upper arm motion evaluations (Edwards et al., 2021). These are some of the most common muscles to use in EMG tests pertaining to the shoulder because of their importance to arm movement especially after operations such as rotator cuff repair. In addition, the biceps brachii and triceps brachii muscles can also be used in an EMG test to help evaluate one's range of motion or level of recovery after an injury or operation on their shoulder or upper arm (Chong et al., 2016).

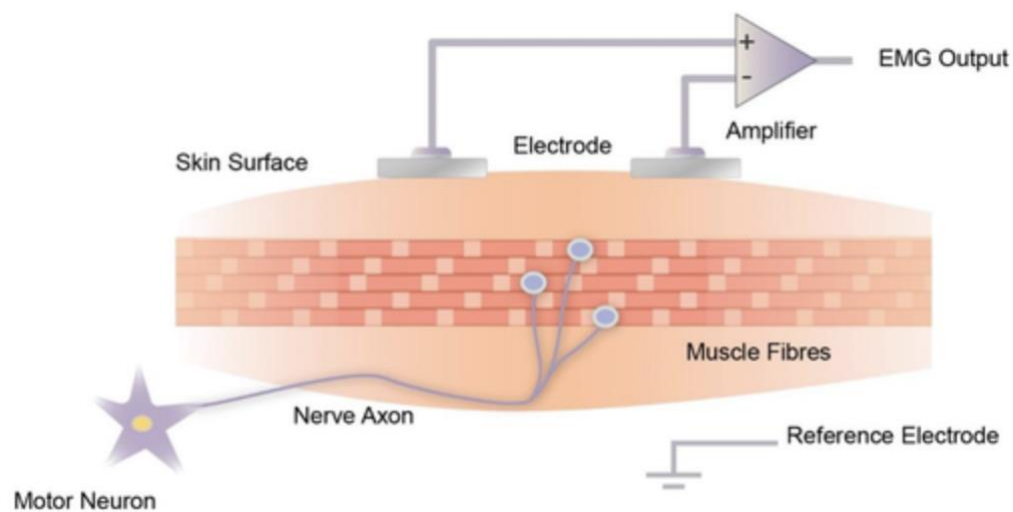


Figure 2-4: Surface EMG Electrode Orientation with Respect to Muscle Fiber Direction (Gao et al., 2022)

2.2.1 General Movements and Keeping Electrodes in Place

While there are various purposes for using EMG to monitor shoulder and upper arm muscles and the exact exercises used in evaluation will differ, some of the most common exercises are depicted in Figures 2-5 through 2-9 (American Academy of Orthopedic Surgeons, 2022).



Figure 2-5: “Pendulum” (American Academy of Orthopedic Surgeons, 2022, Para. 9)



Figure 2-6: “Crossover Arm Stretch” (American Academy of Orthopedic Surgeons, 2022, Para. 10)

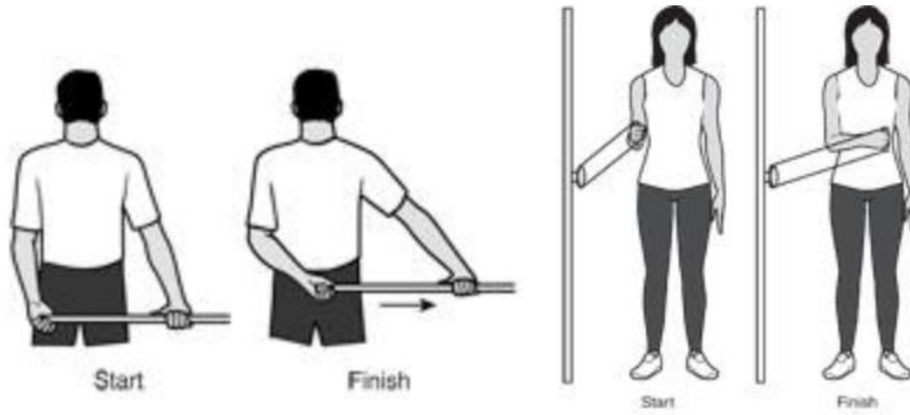


Figure 2-7: Internal Rotations (American Academy of Orthopedic Surgeons, 2022, Para. 11 and 16)

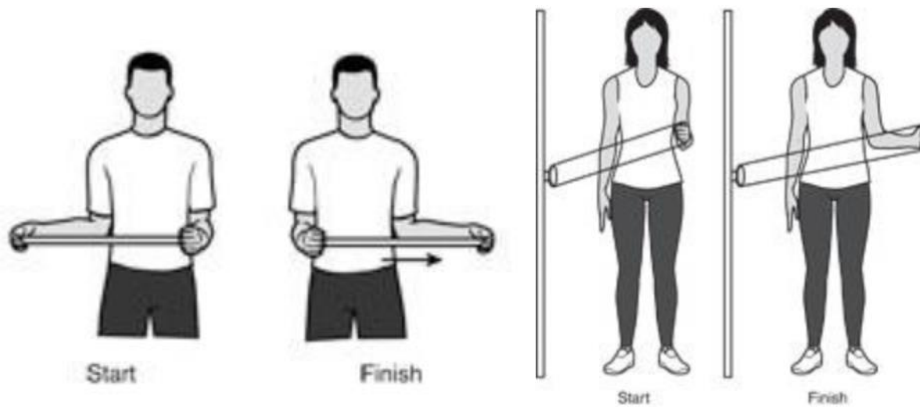


Figure 2-8: External Rotations (American Academy of Orthopedic Surgeons, 2022, Para. 12 and 17)



Figure 2-9: “Elbow Extension” (American Academy of Orthopedic Surgeons, 2022, Para. 19)

Simply by looking at the figures and trying the exercises out for oneself, there are a few additional muscles to consider monitoring for our purposes. The first of these two additional muscles is the trapezius, which supports the general motion (raising and lowering) of one’s shoulder (Varacallo et al., 2023). The pectoralis major has a very similar function to that of the trapezius muscle, but also aids in rotation of the shoulder and arm (The Editors of Encyclopedia Britannica, 2023). Both of these functions are important to being able to perform the exercises outlined in Figures 2-5 through 2-9.

However, before any given EMG measurements can be taken, the electrodes being used must be able to stay stationary even while body movements occur. In the doctor’s office, the electrodes that stick to the skin can be used, but that strategy is not ideal for our at-home application of EMG. There are few existing examples of sleeve applications of EMG, but most of them are very similar and are a variation of using tight-fitting shirts or sleeves to hold electrodes close to the skin (Goncu-Berk & Tuna, 2021). This particular approach can be found in Figure 2-10 where the electrodes go all the way through the shirt. The backside of the electrodes can be seen in the figure and the side of the electrode transducing the EMG is on the inside of the shirt.

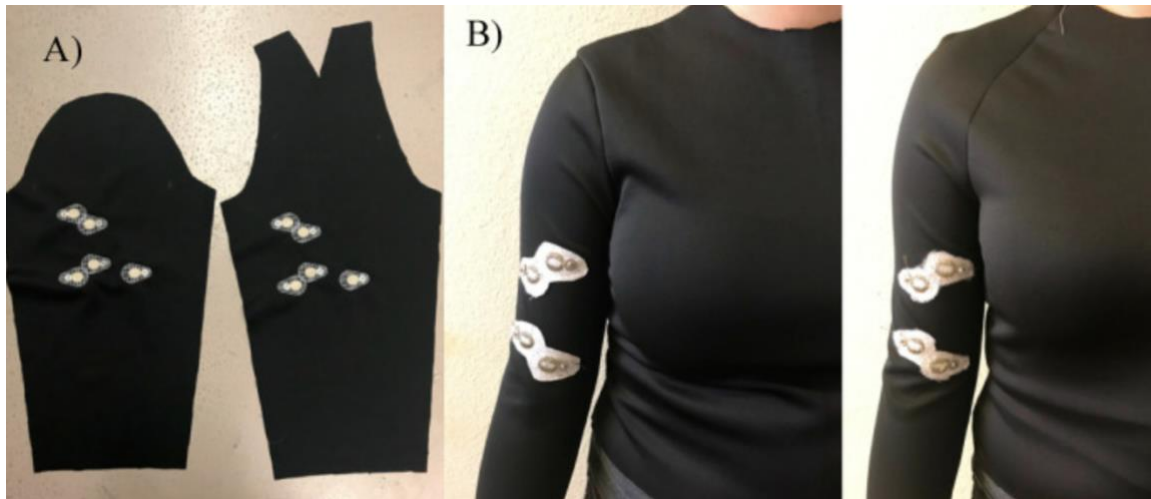


Figure 2-10: Electrode Placement and Mounting (Goncu-Berk & Tuna, 2021)

2.4 EMG Acquisition Circuits

In most cases, the circuits used to measure and evaluate EMG signals have a few major portions. While these circuits can change depending on their exact use and purpose, many follow the signal flow located in Figure 2-11 below (Song et al., 2019). However, this circuit logic in particular is for the analog front end of surface measurements of EMG.

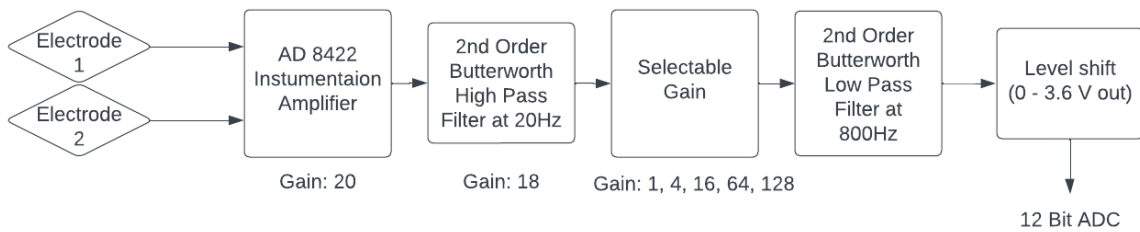


Figure 2-11: High-level block diagram of EMG acquisition front end

2.5 Bipolar vs Unipolar Leads for Front End Design of ECG

2.5.1 Bipolar Leads

2.5.1.1 Limb Leads

Bipolar ECG leads measure the electricity between two electrodes. The electrodes measure the potential difference across the electrodes to see how the heart functions, and to check the heart rate and heart rhythm. Typically, ECG electrodes are placed on each arm between the shoulder and elbow and on the left leg between the torso and ankle (Pahlm et al., 2008). The exact placement makes little difference when measuring the electricity between the electrodes. The three electrodes result in three leads measuring the potential difference either between the two arms, or each arm with the left leg. These three leads form an equilateral triangle, called Einthoven's triangle, around the heart (Al Ghatrif et al., 2012). Figure 2-12 gives a diagram of the placement of the electrodes.

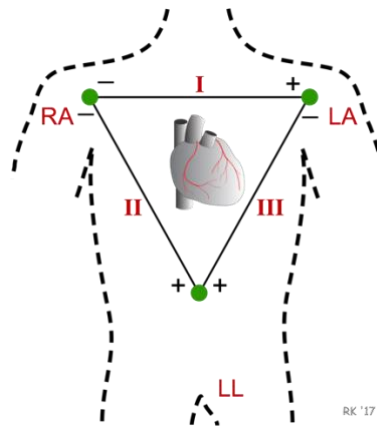


Figure 2-12: Diagram of Bipolar Limb Leads (Klabunde, 2022)

In Fig. 2-12, RA, LA, and LL stand for right arm, left arm, and left leg, respectively, and each of the three leads are numbered. For lead I, which is between both arms, the positive electrode is on the left arm while the negative is on the right arm. For lead II, which is between the right arm and left leg, the positive electrode is on the left leg while the negative is on the right arm. For lead III, which is between the left arm and left leg, the positive electrode is on the left leg while the negative is on the left arm. This placement of electrodes is the standard placement for an electrocardiogram.

2.4.1.2 Augmented Limb Leads

The augmented limb leads are just rotations of Leads I, II, and III. The three augmented leads are aVL, aVR, and aVF. The aVL is -30 degrees relative to the lead I axis, while aVR is -150 degrees, and aVF is +90 degrees (AlGhatrif et al., 2012). A diagram of the augmented leads is shown in Fig. 2-13.

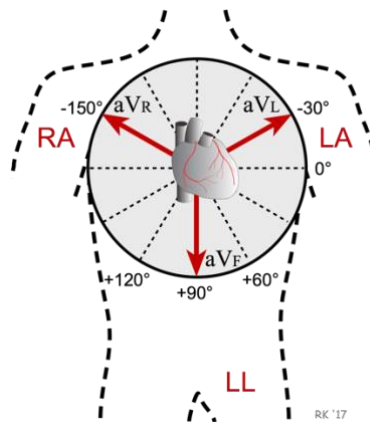


Figure 2-13: Diagram of Limb Leads (Klabunde, 2022)

2.5.1.3 Bipolar Leads for EMG

Bipolar leads for EMG are similar to ECG leads in that there is a three-electrode design. There are two electrodes measuring the signal across the muscle and one used as reference. These electrodes can be placed in a number of different locations including on the biceps, forearms, shoulders, and chest muscles since they are typically the muscles of interest for whatever is being studied. Common optimal placements for the reference electrode is where there is no muscle electrical activity, so over the elbow and wrist since they locations with little muscle and mainly just bone.

2.5.2 Unipolar Leads

Unipolar leads measure the electricity between one electrode and a reference point. The reference point is typically a location that does not exhibit electrical activity. In ECG, the electrode measures the potential difference across the electrode and the reference point to also see how the heart functions, and to check the heart rate and heart rhythm. This reference point is created by connecting the three limb electrodes so that a central negative lead is created.

2.5.2.1 Precordial Leads

Precordial unipolar leads are located on the chest, in six different locations. These six locations are in the fourth intercostal space (ICS) along the right margin of the sternum, in the fourth ICS along the left margin of the sternum, midway between the second and fourth lead, in the fifth ICS along the mid-clavicular line, in the fifth ICS along the anterior axillary line, and in the fifth ICS along the mid-axillary line (Cadogan, 2022). The precordial leads span three different ventricular regions of the heart. The three regions are the anteroseptal, anteroapical, and the anterolateral (Klabunde, 2022). A diagram of the placement of the electrodes is shown in Figure 2-14.

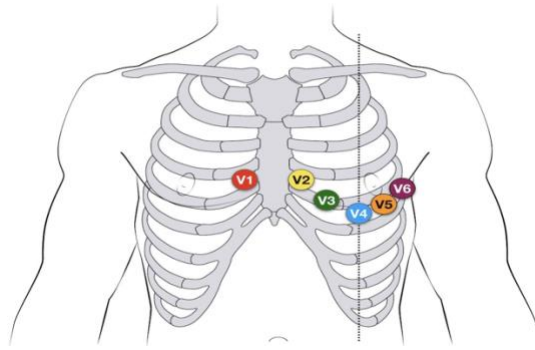


Figure 2-14: Diagram of Unipolar ECG Chest Leads (Cadogan, 2022)

A typical clinical ECG uses all 12 leads: the three bipolar limb leads, three augmented limb leads, and the six unipolar precordial leads.

2.6 Analog Front End of EMG Systems

Collecting electrical signals from the surface of the skin is tricky, and the raw signal contains many artifacts that complicate reading it. The signal generated needs to go through multiple stages of processing in order to make it easily understandable, successfully read by a digital system, and avoid further noise.

While exact numbers vary significantly between application and individual patients, the valuable EMG frequencies are between 20 and 800 Hz, with the bulk of the signal power between 20-200 Hz. Prior to amplification, the amplitude range is typically 0-10 mV, although this range is also subject to vary given the patient and application (Martinek et al., 2021).

Gathered within this signal is lots of noise from outside factors, which are often of greater magnitude than the raw EMG signal. The most common noises picked up by EMG electrodes can be classified into a few categories (Raez, M. B., Hussain, M. S., & Mohd-Yasin, F. 2006):

- Electronic equipment noise: Noise that is generated by surrounding electronic equipment, which can be reduced, but not eliminated.
- Power line noise: Noise generated by AC power sources, typically at 50-60 Hz (and its harmonics).
- Ambient noise: Noise created from electromagnetic radiation.
- Motion artifact: Data within the EMG signal can become skewed when a motion artifact is added to the data collection. Motion artifacts must be reduced through the setup of the system, as reducing it through post-processing is difficult and unreliable.
- Signal Instability: A result of the nature of EMG signals, and their unpredictable nature.
- Electrode-skin noise: Varying impedance of the skin, with factors including sweat and electrode contact.

In order to make an EMG signal contain information that is useful for an operator, or to be read by a digital system with sufficient resolution, the raw data must be transformed to be clearer. The majority of this can, and should, be done prior to conversion to digital data in order for an analog-to-digital converter (ADC) to be able to properly read and convert the signal while minimizing data being lost. To solve the issue, EMG systems need an analog front end that can accomplish the amplification and filtering of the raw signal, while reducing as much noise as possible. A standard implementation of this can be broken down into four parts:

- Differential or comparator amplification: EMG signals need to be amplified immediately after transduction by the electrodes in order to avoid issues with other signal processing stages. This step can also be implemented strategically in order to minimize common-mode noise and noise from the outside environment.
- High-pass filtering: Helps minimize low-frequency noise, such as motion artifacts and DC offsets to negligible amplitude levels.

- Low-pass filtering: Minimizes high-frequency noise that is not a part of the EMG signal. These artifacts typically come from electrical systems apart of the system or in the outside environment.
- Gain stage: Depending on the output amplitude of the previous three stages, additional gain typically will be required to boost the signal to a level that will maximize resolution for analog-to-digital conversion, which will take place after the analog front end.

2.6.1 Operational Amplifiers (Op-Amps)

Op-amps take a differential voltage as an input and output a single-ended voltage. Op-amps take the differential voltage and amplify it using its three terminals. The two input terminals are high impedance while the output terminal is low impedance. The inverting input terminal is marked with the negative sign while the non-inverting input terminal is marked with the positive sign. Op-amps can take current inputs and can convert voltage inputs to current outputs or vice versa, but they are mostly used to amplify voltage inputs to voltage outputs (MonolithicPower, 2022). The nodes labeled +V and -V are connected to a positive voltage supply and negative voltage supply, respectively, and are called the power rails of the op-amp. Fig. 2-15 shows an example circuit diagram of an op amp with the inputs and outputs labeled.

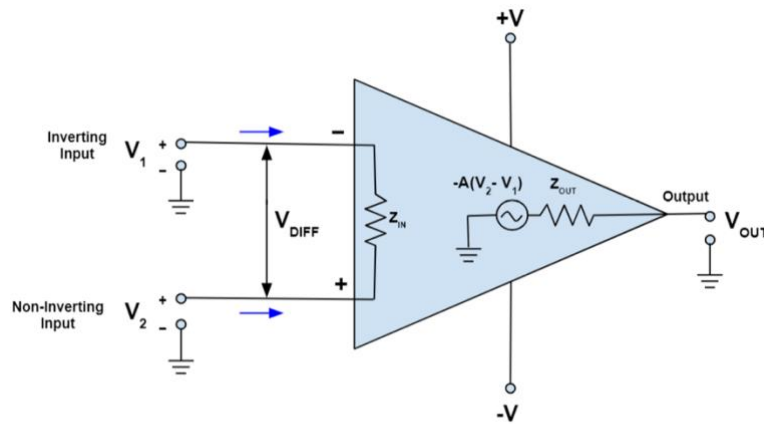


Figure 2-15: Circuit Diagram of an Operational Amplifier (MonolithicPower, 2022)

As mentioned earlier, the differential input is amplified when it passes through an op-amp and this amplification is measured as the gain. When there is no feedback, the gain is called the

open loop gain, and when there is feedback, the gain is called the closed loop gain (MonolithicPower, 2022). The gain is calculated by taking the output voltage and dividing it by the input voltage. In modern op-amps the open-loop gain is quite high. A typical op-amp used in practice is the IC741 which has a voltage open-loop gain of order 200,000.

There are many different types of amplifiers and in the next section we will describe the ones used specifically within EMG applications. The first is the non-inverting amplifier which produces an output signal in phase with the input signal. An example of a non-inverting amplifier is shown in Fig. 2-16.

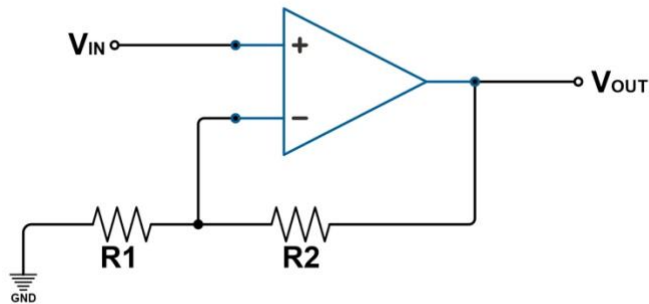


Figure 2-16: Non-Inverting Amplifier

Image Link: [Op-Amp Voltage and Gain Calculator | Newark](#)

In this example the gain is calculated by:

$$A = 1 + \frac{R2}{R1} \quad (\text{Eq. 2-3})$$

The second is the inverting amplifier which produces an output signal out of phase with the input signal. An example of a non-inverting amplifier is shown in Fig. 2-17.

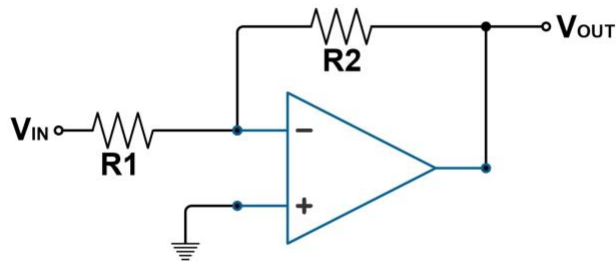


Figure 2-17: Inverting Amplifier

Image Link: [Op-Amp Voltage and Gain Calculator | Newark](#)

In this example the gain is calculated by:

$$A = \frac{-R2}{R1} \quad (\text{Eq. 2-4})$$

Measuring electric signals in a human body is very important to seeing how well the body is functioning. However, these signals are very weak, and the signal is also a differential signal since it is the measurement of the electric potential between two electrodes. An op-amp is the perfect tool to use in an EMG application since it takes in a differential input and outputs a voltage proportional to this difference and amplified. The op-amp makes it possible to acquire electric signals in the body. In the sections below the entire amplification stage of an EMG is explained.

2.6.2 EMG Amplification

With signals obtained from two electrodes on one EMG lead, the first goal of an EMG system is to obtain the difference of the signals, which is what provides valuable information of muscle activation. In the past, this has been completed with standard implementations of differential amplifiers, which are easy to design and intended to achieve this exact goal. The design of these circuits takes an input voltage to both the inverting and non-inverting inputs, which are the two voltages to be differentiated. The inverting input then provides negative feedback to the output by connecting the two terminals together with a resistance in between, R_f . The non-inverting input is then grounded with an added resistance (Raez, Hussain & Mohd-Yasin, 2006).

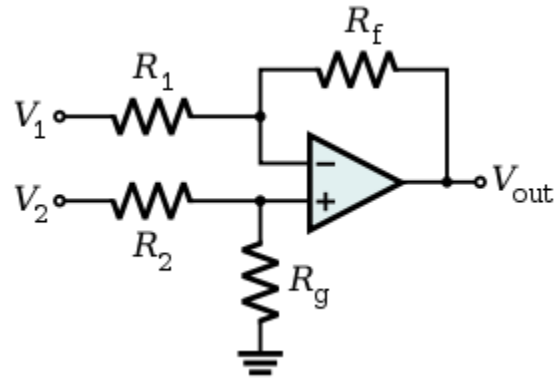


Figure 2-18: Standard configuration of a differential amplifier

(https://upload.wikimedia.org/wikipedia/commons/thumb/a/a2/Op-Amp_Differential_Amplifier.svg/280px-Op-Amp_Differential_Amplifier.svg.png).

2.6.2.1 The Instrumentation Amplifier

An instrumentation amplifier is a specialized version of the differential amplifier that can offer improved performance, especially for EMG applications that need high precision. One of the main advantages for EMG systems is the high input impedance, which is much larger than that of the differential amplifier. Instrumentation amplifiers add input buffer amplifiers that eliminate the need for impedance matching (Kuphaldt, 2004).

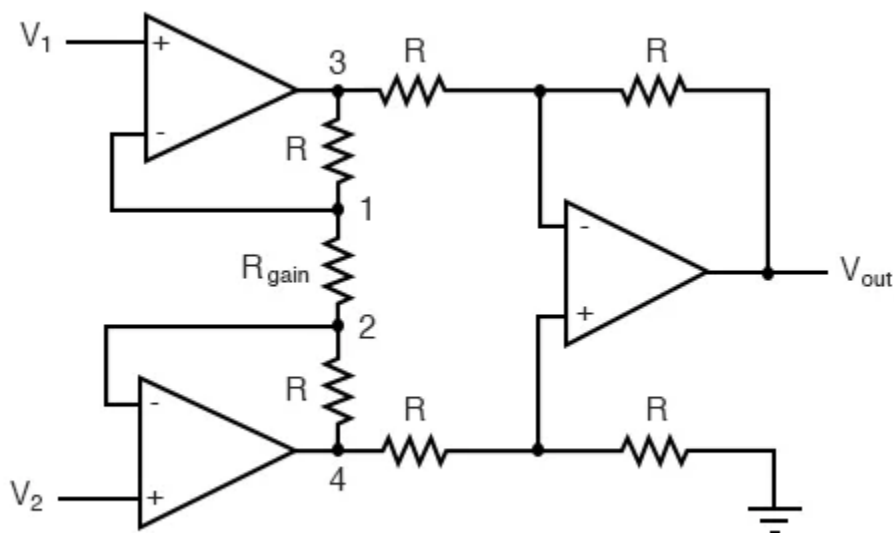


Figure 2-19: Typical instrumentation amplifier configuration.

The configuration for an instrumentation amplifier using the operational amplifiers above is a modified version of the differential amplifier circuit, with added buffer stages for both the inverting and non-inverting input. The buffer stage utilizing the top left op-amp creates a voltage at node 1 to be equal to V_1 and the buffer in the bottom left causes node 2 to equal V_2 . The difference between the two nodes causes current to flow between node 3 and node 4 with a voltage drop across each resistor (Kuphaldt, 2004). The voltage drop across these two nodes can be expressed as,

$$V_{3-4} = (V_2 - V_1) \left(1 + \frac{2R}{R_{\text{gain}}} \right) \quad (\text{Eq. 2-5})$$

After the two buffer stages, the differential amplifier on the right of the schematic above uses the voltage drop between nodes 3 and 4 and then amplifies by a gain equal to the ratio of the R values (Kuphaldt, 2004). The above formulae can be manipulated to achieve the following equation for the overall gain of the instrumentation amplifier based on values for R and R_{gain} ,

$$A_V = \left(1 + \frac{2R}{R_{\text{gain}}} \right) \quad (\text{Eq. 2-6})$$

where R_{gain} is the only resistor that needs to be modified to increase or decrease output amplification, a very desirable property for versatile EMG systems.

2.6.3 Filtering

With all the noise and undesired signals obtained during EMG signal acquisition, the signal needs to be filtered in order to ensure clarity, reliability, and interpretability of the data. The span of complexity of filtering techniques for EMG systems can vary depending on the level of clarity desired for the data, and the muscles being examined. For EMG systems, the range of useful frequencies are often argued by experts, but the consensus is typically in the same proximity for most systems at around 20 Hz - 800 Hz. Thus, it can be assumed that most EMG systems should at the very least provide high pass filtering with a cutoff at around 20 Hz, and low pass filtering with a cutoff around 800 Hz, and done so as soon as possible after signal comparison in the analog front end.

2.6.3.1 Low Frequency Noise

On the low end of about 0-20 Hz, the most common sources of noise come from motion artifacts and offset potentials (0 Hz), which are caused by movement of the electrode across the skin (Roland et al., 2019). Figure 2-19 shows the acquisition of these artifacts both in the time and frequency domain.

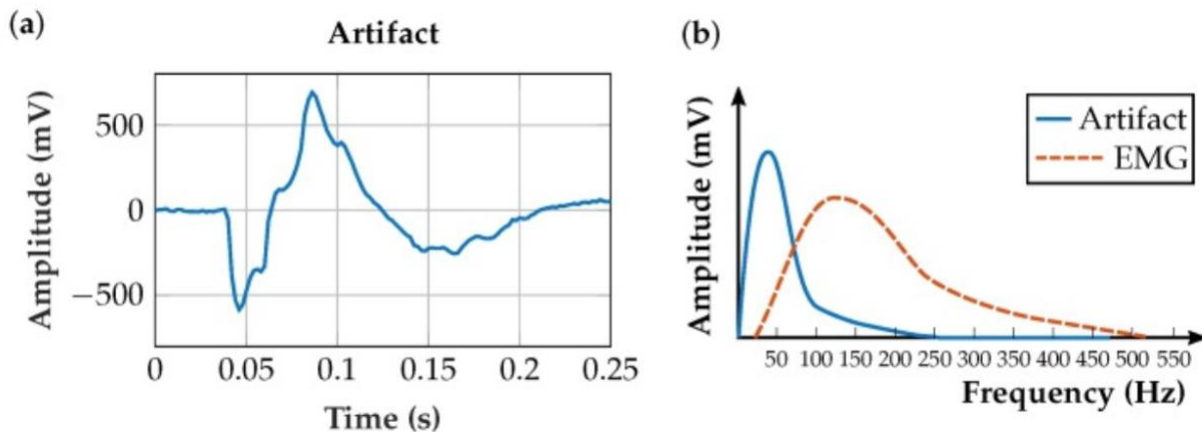


Figure 2-20: Motion artifacts of EMG signals in the time and frequency domain (Roland et al., 2019).

Filtering these motion artifacts early in the front end is important because the low end noise is often many times greater than the EMG data desired, and such significant unwanted noise can cause inconsistency for real time systems, as well as risk saturating the ADC (De Luca et al., 2010). EMG systems can design high pass filters ranging widely in complexity depending on the specifications desired. Generally, a higher order filter will be desired if a sharp transition band is desired. In most cases this will make the system more ideal, but the drawbacks to higher order filters can cause signal delays, and increase power and weight, which is a sacrifice for wearable devices (McManus et al., 2020). One of the common types of filters used for simple analog filtering prior to digitization is a Sallen Key Butterworth filter. Sallen Key is a topology for filters which are often used for their simplicity. Having a simple analog filter allows for small electronic packages that are more wearable, and avoids stability issues that could arise from more complex higher order filters. Figure 2-20 shows a 2nd order Sallen Key high pass filter.

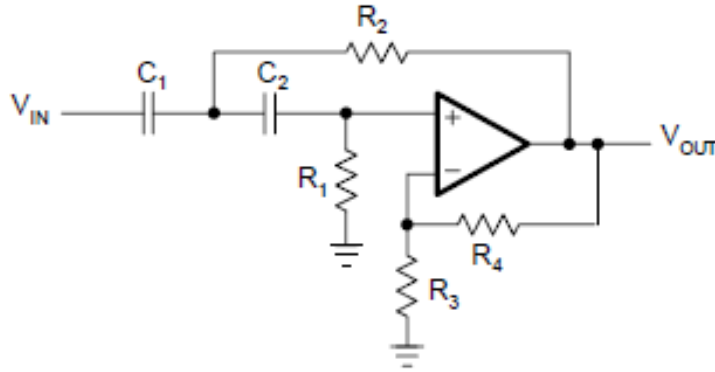


Figure 2-21: Sallen Key Butterworth high pass filter with gain (Fiore, 2021)

The transfer function of this active filter can be expressed through Eq. 2-7, with $C_1 = C_2$.

$$A(s) = \frac{1}{1 + \frac{2}{\omega_c R_1 C} \cdot \frac{1}{s} + \frac{1}{\omega_c^2 R_1 R_2 C^2} \cdot \frac{1}{s^2}} \quad (\text{Eq. 2-7})$$

Through rearranging this equation and assuming a constant C , the two resistor values for a desired cutoff frequency (in Hz), f_c , is (Kugelstadt, 2001).

$$R_1 = \frac{1}{\pi f_c C_1} \quad (\text{Eq. 2-8})$$

$$R_2 = \frac{1}{4\pi f_c C_2}$$

2.6.3.2 High Frequency Noise

Since EMG signals are so small, and the electrodes are so sensitive, there are thousands of outside high frequency signals in the environment that can trump the useful data being gathered. Electronic devices in the environment often transmit signals large enough to be picked up by the EMG electrodes, typically in the kHz range. For our application, low pass filtering is necessary to remove these data before it is sampled by an ADC, which could cause information to be lost. Similar to low frequency noise, a simple 2nd order system can often suffice for the analog filtering stages, so a common approach is with a Sallen Key low pass filter. A Butterworth low pass filter is a similar configuration as the high pass filter, except with the resistors and capacitors swapped.

2.7 Range of Motion and Inertial Measurement Units

The range of motion for a patient in shoulder rehabilitation is one of the crucial outcomes that can signify the progress of recovery. The activation of the shoulder muscles in combination with verified movement of the arm is necessary for a full understanding of the shoulder ability of a patient. In the past this process has been completed mechanically through protractor-like devices known as goniometers, but some experts suggest this process can give inconsistent results (Lee, 2015). Electronic devices have advanced rapidly in the ability to measure motion, and if implemented correctly, can be used to calculate the range of motion for a particular muscle group, and be combined with EMG data muscle analysis.

Many devices responsible for the detection of motion are classified as inertial measurement units (IMUs). IMU's are an electronic device that collects data on the motion and physical position of an object. These devices typically consist of a variety of sensors and components that combine together to collect data on motion given the appropriate application. IMU's can include gyroscopes, accelerometers, and magnetometers which can be used for applications of aircraft, motor vehicles, consumer electronics, and health monitoring devices.

Accelerometers measure linear acceleration. Using the baseline of the earth's gravitational pull, accelerometers detect the changes in force per unit mass. These devices typically measure the proper acceleration, which is the acceleration one can feel and measure. Accelerometers come in a variety of forms, including piezoelectric accelerometers, which use a piezoelectric crystal to generate a voltage when it is compressed or put under pressure. Capacitive accelerometers use fixed plates in combination with moveable plates which move relative to acceleration and alter the capacitance. MEMS accelerometers (micro-electro-mechanical systems) are miniaturized versions of a capacitive or piezoresistive accelerometer within a small integrated circuit that combines mechanical and electrical sensors. This form of device has quickly become the most common option for accelerometers because of the small package and low power consumption, which is especially important for wearable health monitors.

Gyroscopes are sensors that can measure the angular orientation of a device through the use of angular momentum. A mechanical gyroscope uses a spinning wheel or disk that resists

orientation changes. Through the resistance in force, the force required for a change in orientation can be used to determine the degree of motion. Most electronic devices, especially for medical applications, use a MEMS gyroscope, which uses the same principles of a mechanical device but integrates it in a package without any major moving parts. Through the use of semiconductors, these devices leverage the small movement of small structures to detect a rotational change.

Devices with gyroscopes are often integrated with medical devices for balance and movement detection. By analyzing the stability of a gyroscope device, the stability of a patient, or a particular segment of the body, can be understood. Included in this ability is the range of motion of the patient, particularly useful for rehabilitation therapies. The detection of rotation can determine the range of motion for any joint that bends at an angle, including the shoulder.

2.7.1 Goniometers

One of the most important tools used in the medical industry to measure the ROM of joints is a goniometer. The traditional usage of this device is a protractor-like measuring tool that uses arms connected to either side of a joint to measure the angle for the ROM. Usage of this tool on the shoulder joint would consist of two arms on either side of the joint, with the pivot placed at the center of rotation. While these devices are practical and reliable for clinical use, they are impossible for a patient to complete measurements accurately on their own, and it is difficult and time-consuming to record regular measurements throughout recovery in parallel with EMG measurements.

Today, electronic systems exist that are more versatile and some that are even designed for extended wear. By using basic techniques of potentiometers, a system can easily detect an increase in resistance after a bend of some kind of conductor stretching across two ends of the joint. Other techniques utilize flex sensors which will increase resistance when bent, but this can come at the cost of adding mechanical resistance across the shoulder.

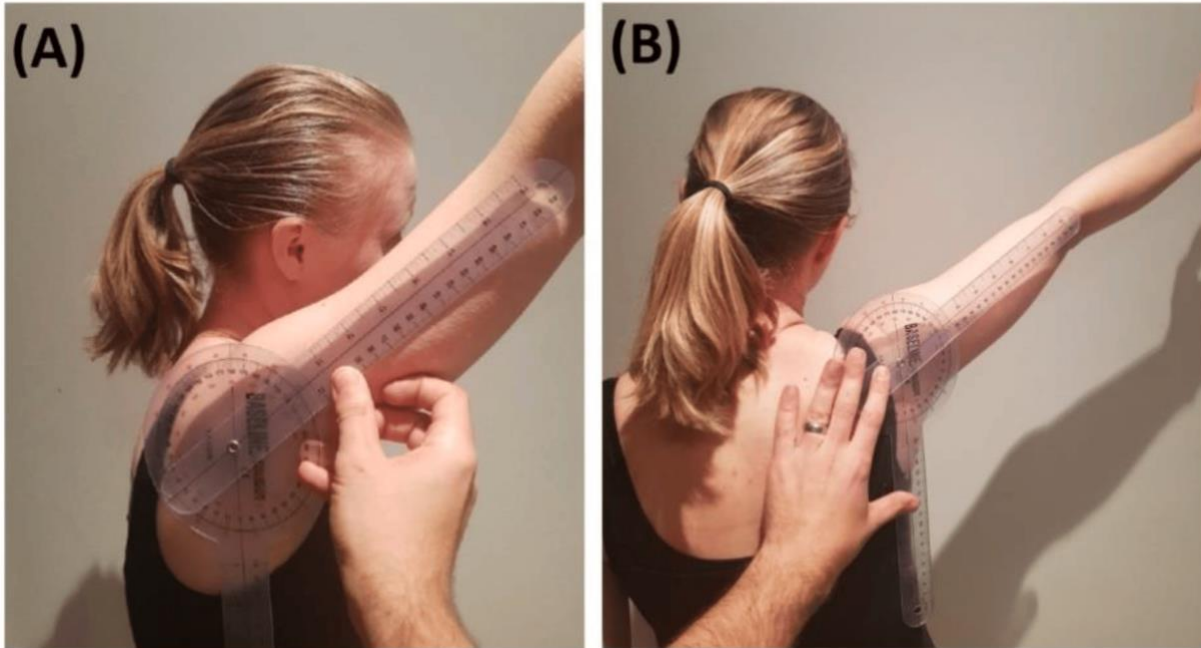


Figure 2-23: Traditional Goniometer use in clinical setting to measure shoulder ROM (Beshara, 2020).

2.8 Microcontroller Overview

A microcontroller is an embedded computer system on a single integrated circuit. This is to say that the microcontroller chip contains a CPU, memory (including program memory), as well as programmable inputs and outputs. Microcontrollers are distinct from a microprocessor, which only contains a CPU. Microcontrollers are used in a wide variety of contexts when computing elements are advantageous in conjunction with other electronic elements, such as a digital alarm clock.

A system on a chip (SoC) is a type of microcontroller with additional electronic components built-in, such as a Bluetooth module or secondary storage. SoCs are widely used in embedded system applications, and one will be used in our design as well; specifically, we are going to use the Adafruit Feather nRF52840 Express, which is profiled in more detail later in this section. The Feather integrates the Nordic nRF52840 SoC architecture, and in fact a program written for one can be easily ported to the other by swapping out a hardware configuration file.

Microcontrollers are broadly used to control the system it's embedded in, as a means of simplifying the hardware while also making it more reliable. In our case, while EMG data could be transmitted wireless through entirely analog means, the process is vastly simplified by passing the signal through an analog to digital converter (ADC) on the microcontroller, programmatically compressing those data points as necessary, and transmitting them over Bluetooth Low Energy (BLE). This is made possible by the nRF52840 having the necessary peripherals for this alongside the microcontroller proper, which in this case is replacing the otherwise costly step of negotiating between the device's inputs and outputs (Davies, 2008 pp. 1-16).

2.8.1 ADC Limitations

In order to be stored in the microcontroller's digital memory, the analog EMG signal needs to be processed by an ADC. This introduces two sources for error, as both the time and amplitude of the signal are continuous and need to be mapped onto some discrete set in this process. Where time is concerned, this takes the form of the ADC's sampling rate, which can be increased exponentially to decrease noise and increase the effective resolution, but which at a minimum should be twice the bandwidth of the EMG signal to avoid aliasing (Silicon Labs, 2020).

$$f_{os} = 4^{n_a}(2B) \quad (\text{Eq. 2-9})$$

Where f_{os} is the frequency to oversample at in Hz, n_a is the effective number of bits of resolution to be added, and B is the bandwidth of the input in Hz.

Where the measurement at a sample is concerned, there is similarly an inescapable rounding error due to there being a finite number of values for the voltage to round towards between the reference voltages as well as the potential for a value to be higher than the high reference voltage or lower than the low reference voltage. While the latter errors can only be mitigated by electrically ensuring that the input voltage is within a known range, the rounding errors can be affected by rounding to smaller increments. Since the data are represented digitally, the number of increments is increased by adding more bits to the output of the ADC, meaning the resolution grows finer exponentially to the number of bits (Davies, 2008 pp. 393-396).

$$R = \frac{V_{refH} - V_{refL}}{2^n} \quad (\text{Eq. 2-10})$$

Where R is the resolution in Volts/division, V_{refH} & V_{refL} are the high reference voltage and low reference voltage respectively in volts, and n is the number of bits of the ADC.

2.8.2 Nordic Microcontroller

The Nordic nRF52840 is a SoC with a variety of useful features balanced out by low power consumption, which is a necessity for a portable device such as this which requires a long battery life. On top of the necessary features for being a microcontroller, the nRF52840 has a successive-approximation ADC and a 2.4 GHz transceiver, both of which are necessary I/O interfaces for this project.

2.8.2.1 ADC Information

The nRF52840 has a 12-bit ADC, meaning each sample rounds to the nearest 2^{-12} or $1/4096$ of the range between the reference voltages. The maximum sampling rate is 200 kHz. The ADC has four channels if both reference voltages are set, but can be set to a single-ended mode (setting the low reference voltage to ground) to use eight channels. While a higher resolution ADC could benefit some contexts, the low resolution functions as a kind of compression which allows it to be transmitted efficiently over bluetooth. That being said, due to the low bandwidth of EMG signals the effective number of bits could be improved by oversampling using the microcontroller's built-in functionality to do so, although the necessary averaging process is done across all channels at once (Nordic Semiconductor, 2021).

2.8.2.2 BLE Information

The nRF52840 has a 2.4 GHz radio transceiver, compatible with BLE. BLE uses 40 RF channels at 2 MHz spacing in the band between 2402 MHz to 2480 MHz, the same frequencies as classic Bluetooth. The difference between BLE and classic Bluetooth is that BLE uses a less complex modulation scheme to lower power requirements, making it useful in this context to maintain a long battery life (Bluetooth Special Interest Group, 2023).

3. Design Options

This MQP aims to integrate multi-channel EMG acquisition with motion monitoring into a removable, wearable, and wireless shoulder device that can help with shoulder muscle analysis for surgical rehabilitation and other applications. Consistent EMG acquisition devices have been researched within the laboratory of our advisor (Professor Clancy), but none of these have integrated a wireless system together that is easily removable, integrates motion data, and is combined into one package designed for the shoulder. The goal for this project is to design all of those parts into one device that is wearable, and balances performance to meet all necessary device requirements.

3.1 System Requirements and Design Options

To create a wireless EMG device, a number of design decisions need to be carefully considered and weighed in order to balance performance while still meeting design requirements. A wireless shoulder device needs to be especially cautious of electrical consumption, physical size and weight, and the integrity of the signals. Too much emphasis on any one aspect of the design will likely cause another area to suffer. Components of the design can be broken up into the following major parts which need to be designed:

- EMG signal leads
- Motion sensing device
- Analog front-end processing
- Analog to digital conversion
- Microcontroller unit (MCU)
- Power supply
- Wearable component housing

With each of these components in an integrated system, the EMG shoulder device needs to meet the following requirements to meet the end goal successfully:

System Requirements	
Wear-time	≥ 4 Hours
Application to shoulder	Removable by the subject
Size of components	Small enough to fit on shoulder housing
Power supply	± 3.6 V
EMG Requirements	
Input signal amplitude	± 15 mV maximum
Gain	Discrete intervals between 1- 46,000
Frequency Range	15 - 800 Hz
Common Mode Rejection Ratio (CMRR)	≥ 80 dB at 60 Hz
Input referred voltage noise (EMG)	≤ 1 μ V between 20-800 Hz
Minimum Input Impedance	1 M Ω
DC Offset	300 mV maximum
MCU Requirements	
Connection to peripheral monitoring device	Wireless
Sampling rate per channel	2 kHz
ADC Channels	5 Channels

Table 3-1: EMG Shoulder Device Required Specifications

3.2 EMG Front End

After transduction of an EMG signal from the electrodes, some kind of differential amplifier must come directly after in order to measure the potential difference between the two electrodes. In order to minimize common mode noise, this process must happen as soon as possible to ensure noise is not further amplified, which could cause EMG saturation or useful data to be lost. Because skin has a very high impedance, it is ideal to pick an amplifier circuit that has a high input impedance, which an instrumentation amplifier offers.

A DC offset is also expected to be obtained from the signal, which is up to 300 mV, much larger than the raw EMG signal (Lee & Kruse, 2008). The stage after the instrumentation amplifier should be a high pass filter to remove this offset, as well as other low-frequency noise from motion artifacts. EMG data are prominent between 15-800 Hz, so a high pass filter of 15 Hz would remove most of this low-end noise while keeping the important EMG data.

This project is also designed to be used across multiple patients and be easily modifiable to be optimized for each case, so gain must be variable for different subjects in order for the ADC to have maximum resolution. The voltage supply of the ADC will be between 3.3 - 4 V depending on the supply chosen, and the maximum EMG signal will be between 0 - 10 mV. For sufficient resolution, the EMG signal needs to be amplified to 0 - the max ADC voltage (3.3 - 4 V). A gain stage must be added that can provide variable levels of amplification based on user input since the maximum EMG signal will change significantly between patients. Changing this gain can be done using dip switches adjusting the gain of a non-inverting amplifier, or it can be handled digitally through a programmable gain amplifier. For the selection of gain, dip switches will likely provide the best solution to customization while giving feedback to the user of the current selection and remaining low-cost and easy to use.

The final block should consist of a low pass filter, which has similar requirements to the high pass filter, in that it needs to have a small footprint and a low power draw for the wearable device. Based on prior research, it has been decided that the high-frequency cutoff should be around 800 Hz, which will keep a wide range of EMG data, without the need for too sharp of a filter roll-off.

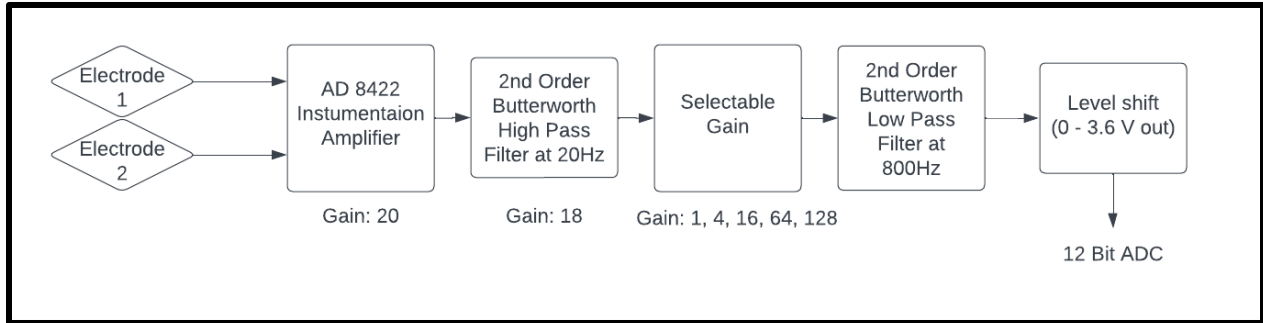


Figure 3-1: High-level block diagram of EMG acquisition front end.

The main design decision needed for this project is the method used to implement each of these analog blocks. Within this option is the consideration of resolution, which can be completed with either a 12-bit or 24-bit ADC. The third option is to implement a more integrated package, such as an ADS 1292, that could accomplish the majority of the analog front end in one package but comes at risk of some requirements due to noise and other factors.

3.2.1 EMG Analog Front End Design Option 1

Using an analog circuit for each block provides higher customization to tune to the project specifications and has prior data available from previous research. A 12-bit ADC would give 2^{12} or 4096 discrete levels. These levels would provide a smaller dynamic range than higher bit alternatives, which noise can limit further. On the other hand, if a Nordic nRF52840 microcontroller is used, the onboard ADC is 12 bits, so creating a higher-bit ADC would use more power, which must be considered carefully for the wearable application of this device. For either a 12-bit or 24-bit system, the same design considerations are given for the design of each analog stage prior to the ADC. This design will use an instrumentation amplifier and a low and high pass filter, all of which have their own design considerations that affect performance. In addition, both design options will need a method for adding user-selectable gain, but the method may vary depending on the option chosen.

3.2.1.1 Instrumentation Amplifier

The use of an instrumentation amplifier was chosen due to the high impedance that is required for impedance matching, which will ensure that there is not a high draw of current from the source. Many integrated instrumentation amplifiers are designed for medical applications like

this, and focus on having a low noise profile, which must be a major consideration for component selection. The AD8422 is based on an industry-standard instrumentation amplifier, the AD620, and offers low input voltage noise at 8 nV/sqrt (Hz) and rail-to-rail output. This can allow output values to swing close to the rail voltage, giving maximum ADC range while simplifying power supply design.

3.2.1.2 Filtering

The first consideration of choosing a filter is the filter order. The high pass filter mainly aims to remove the DC offset and low-frequency motion artifact, so a more shallow roll-off can be acceptable before analog to digital conversion, and further filtering can occur digitally after transmitting. A 2nd order filter would provide 20 dB/decade attenuation, which is acceptable, and would keep power draw and noise to a minimum. As for the low pass filter, the value that could be used for the stopband varies significantly between research. This project plans on a high-frequency cutoff at 800 Hz, which is at the high end of the EMG signal range. Since many EMG signals filter closer to 500 Hz, having a wider roll-off at 800 Hz will be acceptable, as the most important frequencies around 20-200 Hz will be relatively unaltered.

When considering the type of filter to use, the main concern is reducing signal noise, and ideally providing gain to continue to amplify the signal across stages. An active filter would be preferred to address these requirements, and options include Butterworth, Chebyshev, and Elliptic filters. Chebyshev and Elliptic can give steep roll-offs but have ripples in the passband, which can alter the EMG signal to be analyzed. A Butterworth filter has a more shallow roll-off but the passband is relatively flat and the design is relatively simple. If a 2nd order Butterworth filter is used, the roll-off would be 20 dB/decade, and the op amps used in the design can be configured to add gain while filtering.

3.2.1.3 Gain

The overall gain of the EMG signal from the electrodes to the ADC must experience a minimum gain throughout each block before reaching the ADC in order to maximize the resolution available. It is expected that the ADC range will be 3.6 V, meaning an EMG analog input signal should range from 0-3.6 V. It can be assumed that the maximum EMG signal

obtained will be $\pm 5 \text{ mV}$. This gives a 10 mV range, which for 3.6V ADC, would mean a minimum gain of $A = 360$ is needed. Because it is ideal for the user to understand what gain level is selected on the input device, dip switches will likely provide the best solution to a variable gain. If we set the baseline selectable gain multiplier to 1, then the filters and instrumentation amplifiers need to provide a gain of 360 distributed between them.

If the system needs to be able to read a signal as low as 0.1 mV with full resolution, then a total gain can be computed as,

$$3.6 \text{ V} / 1 \text{ mV} = 3,600 = A$$

which is 10x that of the minimum gain. With this expectation, it can be assumed that selectable gains of $A = 1, 2, 4, 8, 16$, will suffice to give a full range of the ADC for almost all uses of the shoulder EMG.

3.2.2 EMG Front End Design Options 2

The consideration of a 24-bit system includes most of the same specific blocks for each analog stage, but exact value requirements are altered due to the higher resolution and the effects of doing so. The higher resolution of a 24-bit ADC would give 2^{24} , or over 16 million discrete levels, as compared to 64 thousand for a 16-bit system. Those added bits give more space for other analog peripherals, including digital selectable gain, which can remove analog switches.

The biggest drawback for a 24-bit system is the power and data requirements. In order for the higher bit resolution to even be useful, the noise level must be kept low enough to even take advantage of the additional least significant bits. Making the device 24 bit would require oversampling, or an external ADC, both of which can up to double the power draw of the microcontroller using a 12-bit ADC. While adding more bits can allow for a smaller analog package and allow for higher resolution, the tradeoff of power consumption and other unknowns may not be worth it for a project that is not focusing on optimization as much as system integration and functionality.

3.2.3 EMG Front End Design Option 3

3.2.3.1 ADS1292ECG-FE Integrated Circuit Description and Application

The ADS1292ECG-FE has two input channels each equipped with two low noise programmable gain amplifiers (PGA) and two high-resolution ADCs which are the ADS1292 and ADS1292R. The ADS1292 is a 24-bit multichannel delta-sigma analog-to-digital converter. The ADC can handle simultaneous sampling and contains an oscillator and internal reference (Texas Instruments, 2020). The ADC has a flexible input multiplexer, one per channel, that independently connects to the internally generated signals for temperature, test, and lead off detection. Although the right leg drive amplifier will not be used in our application, the ADC allows any configuration of input channels to be selected for derivation of the right leg drive output signal (Texas Instruments, 2020). The right leg drive is something that can be added to signal amplifiers to reduce common mode interference which improves the common mode rejection ratio. The ADS1292ECG-FE contains thirty-two pins with either QFP or QFN packaging. A functional block diagram of the ADS1292ECG-FE can be seen in Figure 3-2.

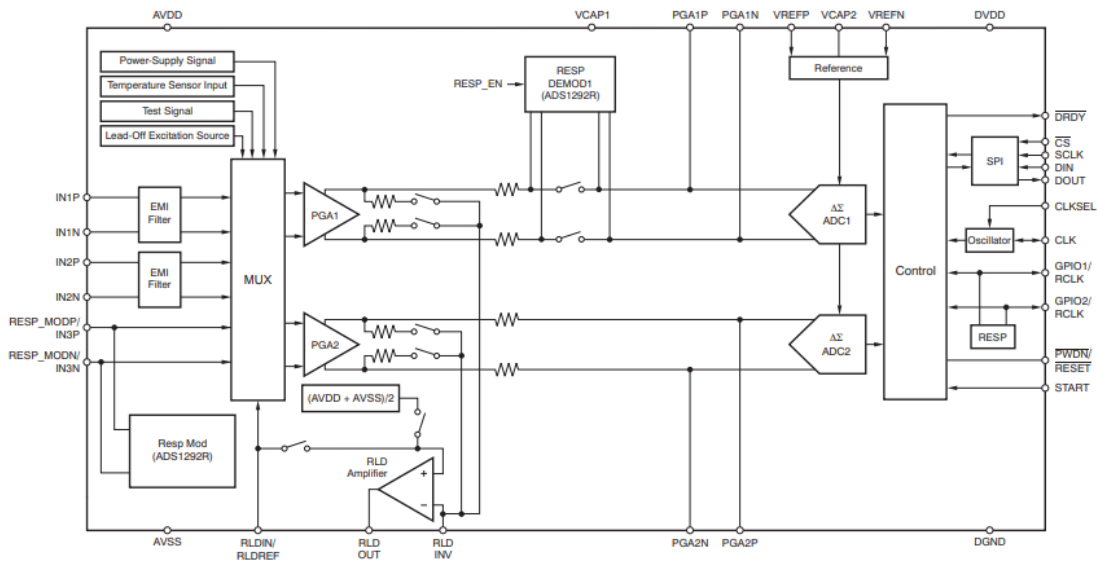


Figure 3-2: Functional Block Diagram of the ADS1292ECG-FE (Texas Instruments, 2020)

The application of the ADS1292ECG-FE is towards health monitoring, whether it be patient monitoring or just personal care and fitness monitoring. The device can be used to record stress and vital signs like ECG, and be used to measure heart rate and respiration. Other

applications of the ADS 1292 include any high precision multichannel data acquisition (Texas Instruments, 2020).

3.2.3.2 Specifications

Some of the specifications of the ADS 1292 are listed in Table 3-2 below.

Operating Temperature	-40°C to 85°C
Low Power	335 μ W/channel
Input Referred Voltage Noise	8 μ V _{PP}
Input Bias Current	200 pA
Data Rate Per Channel	125 SPS to 8 kSPS
Programmable Gain	1, 2, 3, 4, 6, 8, or 12
Supplies both Unipolar or Bipolar Power	Analog: 2.7V to 5.25V Digital: 1.7V to 3.7V
Common Mode Rejection Ratio	120 dB at 50 and 60 Hz

Table 3-2: ADS1292ECG-FE Specifications

3.2.3.3 Noise Comparison

In Table 1 it was determined that the noise requirement be less than or equal to 1 μ V RMS. The input referred noise of the ADS1292 can be seen in Figure 3-3 vs time and occurrence, at 150 Hz bandwidth and a gain of 6, so that we can compare the noise to our requirement.

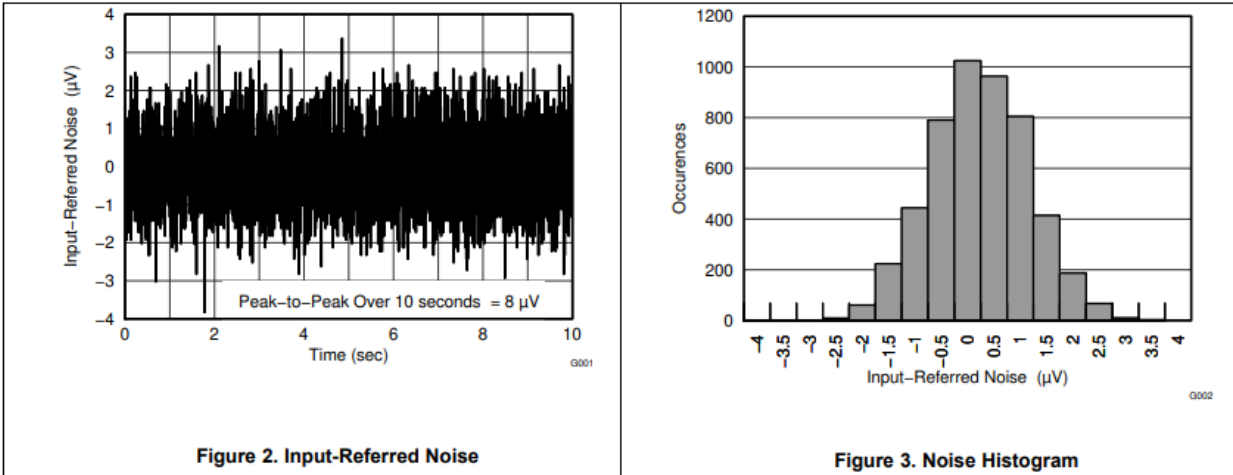


Figure 3-3: Input-Referred Noise vs Time and Occurrence Tested at 150 Hz Bandwidth (Texas Instrument, 2020)

As can be seen above and in Table 2 the input referred noise is 8 μV P-P, however to compare to the 1 μV RMS we need to convert to μV RMS. The standard deviation of the noise histogram is equal to the noise in RMS. First, we used a digital ruler to calculate the occurrence values of each bin. Then we calculated variance using multiple methods. The first was using equation 3-1. N-1 is being used instead of N since we are using the sample mean instead of the population mean. This gives a more accurate calculation of variance.

$$Variance = \frac{\sum_{i=1}^n f_i(x_i - \bar{x})^2}{N-1}, \quad (\text{Eq. 3-1})$$

where n is the number of bins, f_i is the occurrence value, x_i is the input referred noise in μV, N is the sum of all the occurrence values, and $\bar{x} = \frac{\sum_{i=1}^n x_i * f_i}{N}$ which is the mean value. We got a variance of 0.908722 which is a standard deviation of $\sqrt{0.908722} = 0.953 \mu\text{V}$.

The second way we calculated variance was using equation 3-2.

$$Variance = \overline{x^2} - \bar{x}^2, \quad (\text{Eq. 3-2})$$

where $\overline{x^2}$ is just $\bar{x^2}$ with squared values of x_i and \bar{x}^2 is just \bar{x} squared. We got a variance of 0.908541 which is a standard deviation of $\sqrt{0.908541} = 0.953 \mu\text{V}$. Using both equations, we got the same standard deviation so the noise of the ADS1292ECG-FE is 0.953 μV RMS, which meets our requirement. However, for reasons mentioned in the next chapter we have decided to

not focus on this design option but instead research it in parallel with hopes that someone in the future can take this and go further.

3.3 IMU Measurements

3.3.1 Flex Sensor

A flex sensor is an analog sensor that measures the amount of contraction or bending by increasing resistance as it is bent. A flex sensor is a good selection for our application since it can be used to measure the angle of an arm, is easy to use, and is small so it can fit into whatever wearable shoulder sleeve we decide on. The manufacturer Spectra Symbol has a couple options, including the FS-L-055-253-ST flex sensor, and they are readily available. Spectra Symbol has shorter flex sensors available with a length of 2.9 inches and a longer flex sensor with a length of 4.4 inches. Both flex sensors have a long life cycle of over one million uses and a good temperature range from -35°C to 80°C (Spectra Symbol). Some of the specifications on the FS-L-055-253-ST flex sensor are a flat resistance of 25 kilo-ohms, resistance tolerance of plus/minus 30%, a bend resistance ranges from 45K to 125K ohms over 0° bend to 90° bend, and a power rating of 0.5 W continuous and 1 W peak (Spectra Symbol). The dimensions of the sensor are 0.250 inches thick and 2.9 inches long but only 2.18 inches of it actually does the bending.

3.3.2 Accelerometer

An accelerometer measures acceleration, typically by measuring the displacement of some known mass similar to how a scale measures weight. Three perpendicular two-axis accelerometers with known displacement from one another can be arranged in a manner to precisely measure displacement and orientation in space. However, such precision cannot be relied on in our case, and would make our measurements significantly inaccurate due to the algorithm used to calculate those measurements from the accelerometer data. The position and orientation data are calculated from acceleration measurements by presuming an inertial reference frame and integrating over the acceleration data with respect to time. This means that any inaccuracy in the initial conditions will cause the IMU to drift over time, which would

complicate the data and require more complexity in the design (such as some form of calibration) to account for. The path to get there is more complex, and outside the scope of this project (Ang et al., 2003).

3.4 Microcontroller

For the selection of a system on a chip, several necessary features were taken into account, such as a Bluetooth antenna, and an ADC with enough channels for our needs as well as support for oversampling if necessary. While a number of boards other than the Adafruit nRF52840 Feather Express provide this functionality—such as the Texas Instruments CC26X51—our lab has the most experience with the Feather board. Additionally, a significant amount of code from this earlier work with the board can be reused to expedite development. Since the Feather is essentially sufficient for our needs as-is, any similar hardware would need to provide some equivalent advantage in ease of development to make switching to it worthwhile.

Nordic also offers nRF52840 development kit boards which can be used to more easily reprogram boards such as the Feather boards and gather debugging information from them. These development kit boards are being used in our prototype as the central node from which data are transmitted over UART to a PC. For the purpose of programming, the development kit boards are extremely similar to the Feather boards on account of them both using the nRF52840; in fact, the Zephyr kernel we are using for development even allows us to run the exact same code across both boards with merely a change of configuration files.

That being said, the Nordic nRF52840 does have its limitations. For example, its ADC only has a 12-bit resolution—which leads to some wasted data when being stored due to not being a multiple of 8. Another would be the connection interval of at least 7.5 milliseconds used due to its use of the BLE standard, although this can potentially be overcome by sending multiple packets within one connection interval. However, ultimately these limitations are largely insignificant in the context of our project.

3.4.1 Sampling rate

The optimal sampling rate for the ADC is restricted by a number of factors, including but not necessarily limited to input bandwidth, necessary effective resolution, and BLE packet size. The minimum sampling rate is given by the Nyquist frequency of the input, i.e. twice its bandwidth. Should the 12-bit resolution of the ADC prove insufficient, the signal can be oversampled by taking samples exponentially more frequently and averaging the results. However, the Nordic nRF52840 performs this averaging over all channels simultaneously when sampling in “scan” mode, so the built-in support for this can only be taken advantage of if only a single channel is being used and/or all channels are sampled at the same frequency. However, our software is a “burst” mode implementation which takes all samples in rapid succession, meaning oversampling can be implemented in C without using Zephyr functionality as a means of circumventing this limitation.

A BLE packet will be sent every 10 milliseconds (slightly longer than the minimum connection interval), and one packet contains a maximum of 258 bytes of data. Of those bytes, 30 will contain a header, and the nRF52840’s 12-bit ADC means that one sample will take up two bytes (with four unused bits). Accordingly, the maximum average sampling rate that can be used across the 5 channels of the ADC being used is given by:

$$f_s = 100 \frac{(258-30)}{2(5)} = 2280 \text{ Hz} \quad (\text{Eq. 3-3})$$

For the 258 bytes of data per packet minus the 30 bytes of a header, divided by the 2 bytes for a data point across each of the 5 channels every .01 seconds.

While the limitations imposed by the packet size could potentially be overcome with compression or other approaches to transmission, this could complicate the process of data collection and should be avoided if possible.

3.5 Power Supply

Battery power is important to consider when it comes to how long the end product will be able to function. Based on the datasheet, the nRF52840 is able to operate using a single-sided

voltage supply with voltage anywhere between +1.7 V and +5.5 V (Nordic Semiconductor, 2021). It is ideal to give the ADC a higher consistent voltage of 3.6 V or above.

The main consideration for a battery-operated system is whether to use a bi-polar or unipolar system. A standard design for use of operational amplifiers requires a bi-polar power supply in order to reach positive and negative levels of the output. To work around this, level shifting and modifications to the op-amp circuit could allow the device to run off a unipolar supply. This option, while more complicated, does reduce the footprint and complexity of the system by only requiring one battery. A unipolar supply could also work by using a charge pump, which would take the positive supply and act as an inverter to create an additional negative supply rail. While an option, there are many unknowns for this project on how a charge pump would work in practice, including power draw and voltage stability.

Previous research in our lab has used a bipolar power supply, and then used a voltage regulator along with an adder circuit, to offset the output signal to the ADC range of 0 - 3.6 V. While voltage regulators are not particularly power efficient, their use has been proven in battery operated devices, and provides the easiest path for implementation.

For battery options, the LIR2450 watch battery is rechargeable and is rated to provide 3.7 V with a typical capacity of 120 mA hours of power available and weight of about 5.5 grams (Power Stream, 2023). These batteries are about five dollars when purchased individually. Another option is a 9 V battery. In that case, there are both rechargeable and non-rechargeable batteries. For the purposes of our end-goal product, a rechargeable 9 V battery, even though more expensive than non-rechargeable, is more cost-effective and can be used more than once before needing replacement. For example, a rechargeable 9 V battery such as the Energizer NH22-175 (HR22) is rated to provide a nominal 8.4 V with a typical capacity of 175 mA hours of power and weighs about 42 grams (Energizer, n.d). This particular battery costs upwards of \$11.99 when sold individually. However, a 9 V battery would be very large and heavy compared to our other battery options.

Based on the calculations below, either of these batteries is sufficient for powering our device. The power draw of an AD8422 instrumentation amplifier is about 338 μ A. If design option 1 is used, the other power draw from the analog front end will be from two op-amps used

for filtering and another used for selectable gain. An op-amp (LMC6484) that would be used for this project would draw about $210\ \mu\text{A}$ per op-amp, so $210\ \mu\text{A} \times 4 = 840\ \mu\text{A}$. That would give the total power consumption for the analog front end as roughly $1178\ \mu\text{A}$, or about $1\ \text{mA}$. The Nordic microcontroller that will be used for this project draws about $2.4\text{-}3\ \text{mA}$ for the ADC and BLE transmission (Rajotte, 2023). This additional current draw brings the total current draw estimation to $4\ \text{mA}$. With a $175\ \text{mA hour}$ battery, it is expected to get at least $175\ \text{mA}/4\ \text{mA} = 43.75$ hours of operation off of one LIR2450. The $9\ \text{V}$ battery does provide more mA hours of capacity, which gives about 137 hours of operation, assuming a given $9\ \text{V}$ battery has $550\ \text{mA hours}$ of capacity. Therefore, in addition to weighing and costing much less which is better for our application, the LIR2450 is also the better option for battery power.

3.6 Shoulder Sleeve/Strap

As previously discussed in section 2, surface electrodes are most commonly sticky pads that adhere directly to the skin. However, they are generally one-time use and would not be the best solution for at home use. In addition, one of the most common ways to secure surface electrodes in place outside of a doctor's office, such as in at-home products, is the use of a tight-fitting long sleeve shirt as depicted in Figure 2-10. The exact placement of the electrodes in that case would not be uniform in terms of location in the shirt for all patients. The location of the electrodes on each shirt would be in line with the chosen muscles, but those muscles are in slightly different locations and at different distances from one another depending on the size of the patient.

One potential solution to optimizing the placement of the electrodes on a compression shirt would be to make the position adjustable. Such adjustable placement would allow any patient to use the product. Adjustable placement could use strips of Velcro inside the shirt, but before any at home use the placement of the electrodes would need to be set by a doctor or other medical professional. While the Velcro would be used in strips along the arm and shoulder, parts of the Velcro would touch the skin even when the electrode is in place. In order to best take care of potential skin irritation, the softer side of the Velcro would be on the shirt facing the skin while the other side would be on the backside of the electrode itself. However, for initial testing purposes, the electrodes were held in place using an ACE bandage. Such a bandage was

sufficient for short tests but would not be sufficient for long-term testing or final at home use as it would be much easier to undo or skew electrode positions making the measurements less useful.

4. Design Selection

After considering the three main design options for the EMG acquisition, the final design choice is option 1, to use an instrumentation amplifier with 12-bit ADC. This design will use an instrumentation amplifier, the AD 8422, connected directly to the leads, 2nd order high and low pass Butterworth filters with gain, and an additional adjustable gain. This design selection was chosen for a couple of reasons: ease of implementation and electrical consumption.

Design option 2 was ruled out because of the added complexity for a 24-bit system to be implemented, including additional power draw, and other unknowns. Current data of typical operation for sampling at 2 kHz with a 12-bit ADC and transmitting over BLE will consume about 2.4-3 mA (Rajotte, 2023). A 24-bit system would require additional ADC hardware or oversampling, which could almost double the power consumption. A 12-bit ADC would mean the effect of gain could not be replicated by masking out irrelevant bits since not enough bits of captured data would be available, but this is acceptable because the analog gain stage would only add one additional op amp, or an estimated 210 μA of current draw, which is significantly less than the extra power needed for a 24-bit ADC.

Design option 3, which was using the ADS1292ECG-FE as the front end, was not chosen because of two main reasons. Those reasons are the complexity of programming, and lack of experience working with the ADS1292ECG-FE. Programming the ADS1292ECG-FE is complex since the software is outdated and it is hard to write new scripts for the device and upload to it. The last reason is that the team does not have any experience working with a device like the ADS1292ECG-FE, so there are many unknown variables that could disrupt the design goal to have a complete and integrated system by the end date. Instead, for this design option, we assessed its function as a side project to determine if this option is worth these tradeoffs for future research.

The existing framework for the chosen design allowed for more time to be allocated to the integration of the wireless system and optimization for performance on the shoulder. The main goal for this project was to get a running system that meets all the requirements, and extra time can be spent afterward to optimize for the best noise and signal integrity performance. A 2nd order Butterworth filter will suffice for this project because minimizing added power

consumption and noise is more of a priority than sharpening the filtered window. This option also allows for gain to be added, which can help simplify the design for a customizable gain stage. Gain will be selected using dip switches and performed through a non-inverting op-amp configuration. The total gain for the system will range from 360-46,000, which will provide flexibility for EMG signals to be displayed will full resolution of the ADC from $10 \mu\text{ V}$ to 10 mV.

As for the microcontroller, the Nordic nRF52840 is suitable for all of our hardware needs and provides the aforementioned 12-bit ADC. Its technical performance meets our needs and the experience we can draw on and ease of development for it makes it possible to rapidly prototype software and test a wide range of designs and implementations. The Adafruit Feather nRF52840 board was used as a peripheral node to receive data directly from the sensors and transmit it to the central node due to their small size and low power consumption. The Nordic nRF52840-DK board was used as the central node to receive that data over Bluetooth and send it over UART to be collected on a PC due to its easily accessible debugging tools. However, the use of the Zephyr kernel in development makes it so that the code used for one SoC can also be used on the other.

5. EMG Front End

5.1 Methods

The EMG analog front end of this project incorporates each of the blocks in the selected design, design option 1, and implements them on a solder board that is relatively compact and wearable. This design is powered by a bi-polar power supply consisting of two-coin cell batteries in series with a center tap which serves as the reference potential. Both of the power rails are rated to stay equal to or above ± 3.6 V while in operation.

After completing circuit simulation through Multisim for each of the stages of the front-end design, the team prototyped the circuit of the selected design by assembling it on a protoboard one EMG channel at a time. Data were then collected about the response of each stage given various input sine waves. This prototype channel was then used to collect an EMG signal through sticky electrodes and viewed on an oscilloscope prior to integrating with the microcontroller. The full prototype can be seen in Figure 5-1. After the completion of the full protoboard prototype, the final circuit was soldered onto two solder boards and used to create four EMG channels total. One of these solder boards can be seen in Figure 5-2.

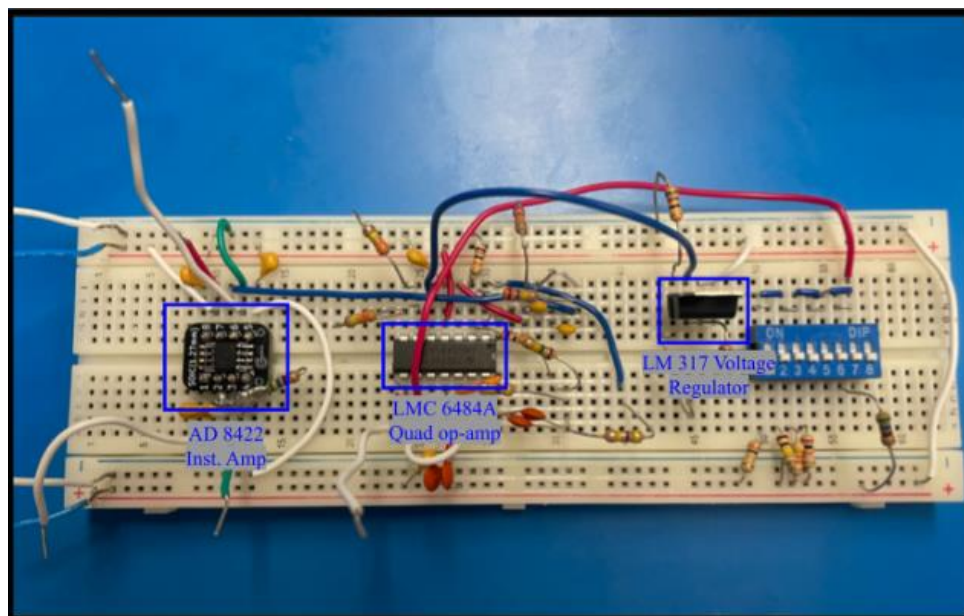


Figure 5-1: EMG front-end prototype.

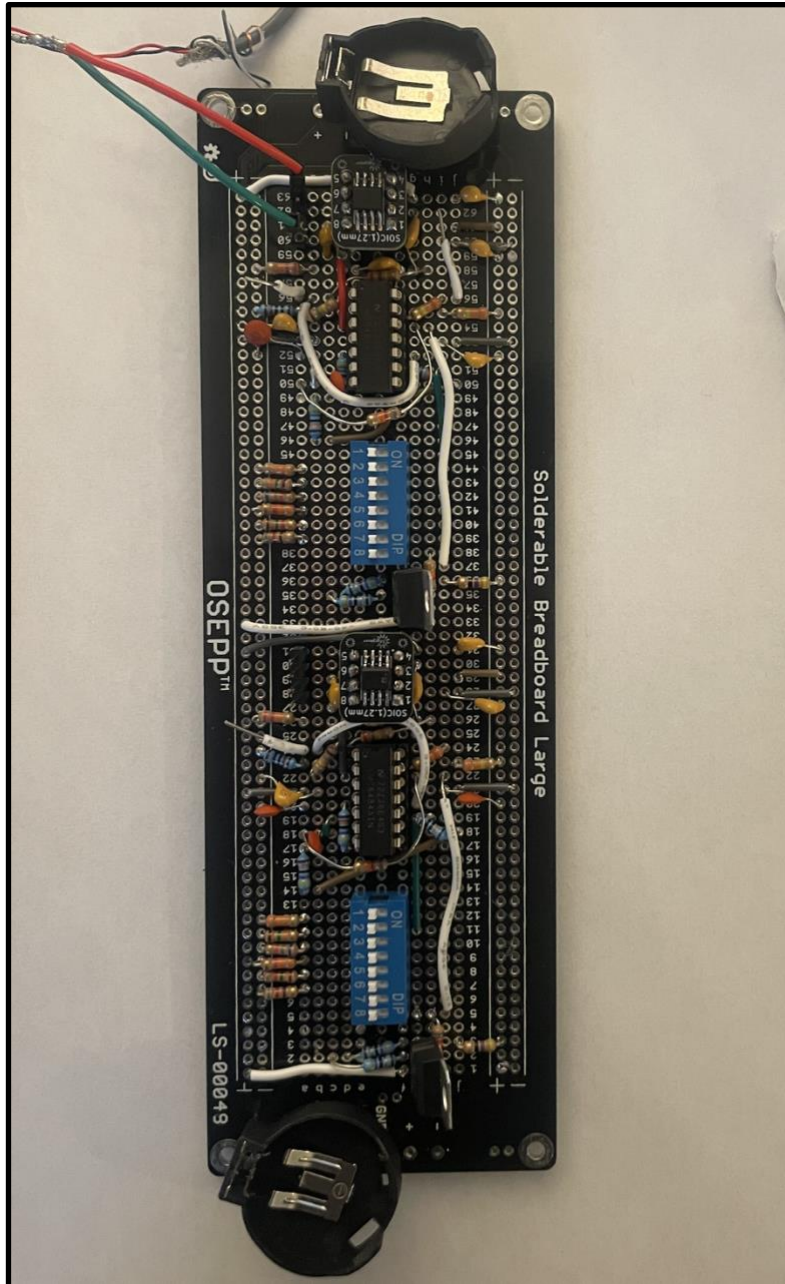


Figure 5-2: Solder boarded prototype of two EMG front end channels.

5.2 Instrumentation Amplifier Circuit

The instrumentation amplifier used was the AD 8422. This device is an upgraded version of the previous industry standard for low-noise instrumentation amplifiers, the AD 620. The AD 8422 has the following pin-out diagram using a SOIC_N package type.

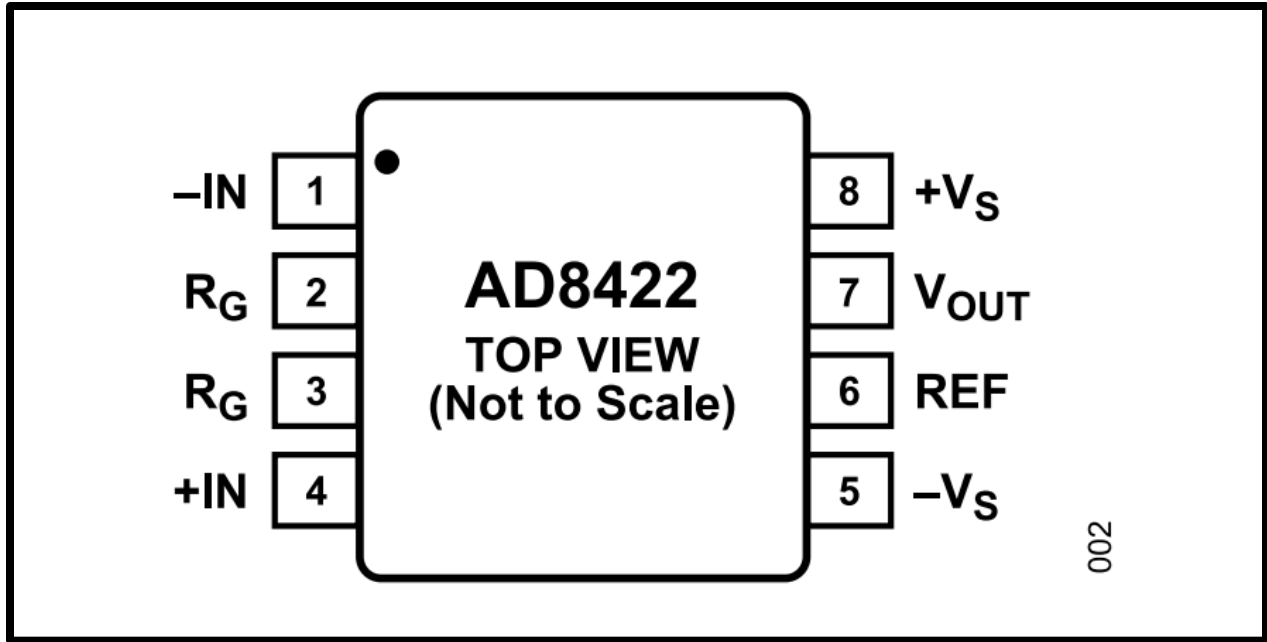


Figure 5-3: AD8422 pinout diagram

The input pins are connected to each of the two electrodes for a single EMG channel, and the two R_G pins accept an input impedance that determines the gain of the amplifier. While designed to use a standard resistor input, by using a capacitor in series with R_G , the instrumentation amplifier can act like a high pass filter. The resistor value was determined using Eq. 5-1 as $1\text{ k}\Omega$ by solving for a gain of $G = 20$ (Analog Devices, 2022).

$$R_G = \frac{19.8k}{G - 1} \quad (\text{Eq. 5-1}).$$

Because the complex impedance of a capacitor is equal to $\frac{1}{j\omega C}$, a transfer function for the system with a capacitor in series with R_G can be derived to be,

$$H = \frac{19.8k}{1k + \frac{1}{j\omega C_G}} \quad (\text{Eq. 5-2}).$$

Using equation 5-2, a value for C can be determined depending on the desired gain at any given frequency. Using a modified version of a MATLAB script created by previous research groups, `iamp_stage_v01`, the frequency response of the created filter can be visualized for any input capacitance. The full MATLAB script can be seen in Appendix B. Using this visualization,

a capacitor value of $4.7\mu F$ was chosen to create a steep enough roll-off to attenuate signals below 20 Hz by at least -3 dB. Figure 5-4 shows this response.

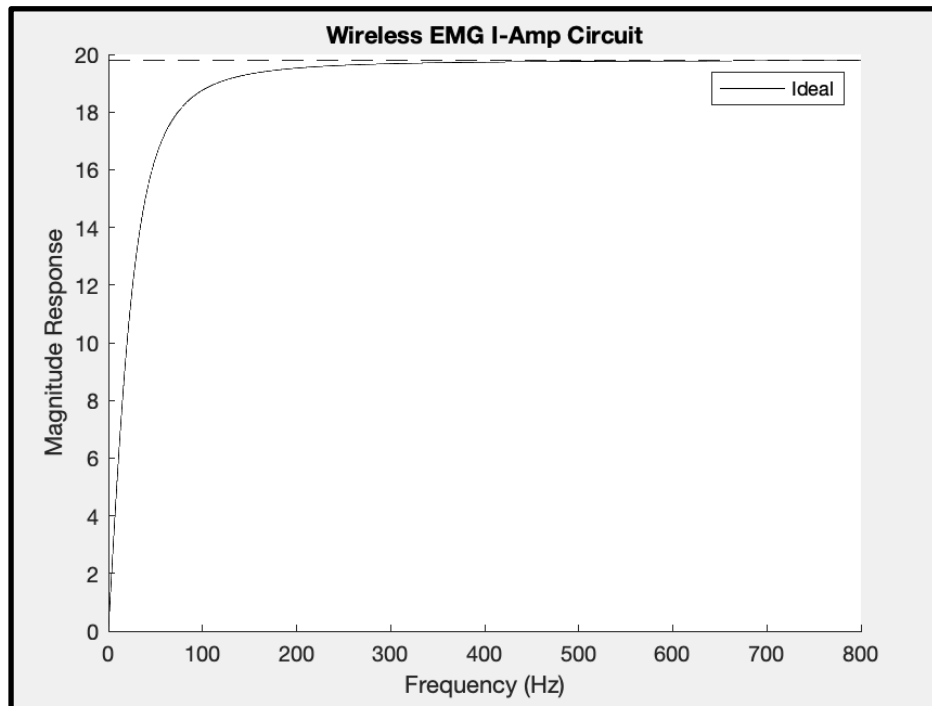


Figure 5-4: Transfer function of instruction amplifier filter response

A circuit schematic was then created using Multisim, as seen in Figure 5-5. Decoupling capacitors were added to both power rails on the prototype, as close to the input as possible, and were chosen as $1\mu F$ based on datasheet specifications for the AD 8422.

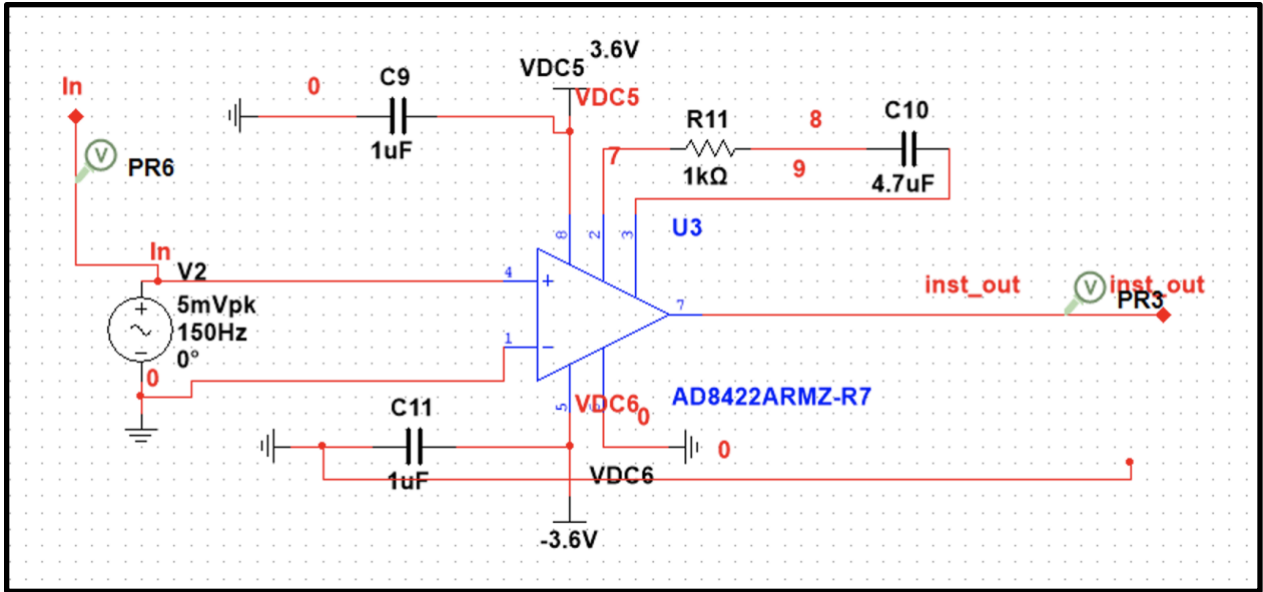


Figure 5-5: Instrumentation amplifier circuit schematic.

Once prototyped on a protoboard, the instrumentation amplifier was tested using an input sine wave of magnitude 10 mV pk-pk at various frequencies to get a complete frequency response. Figure 5-6 shows this response in red with a magnitude of 26.3 dB at 150 Hz.

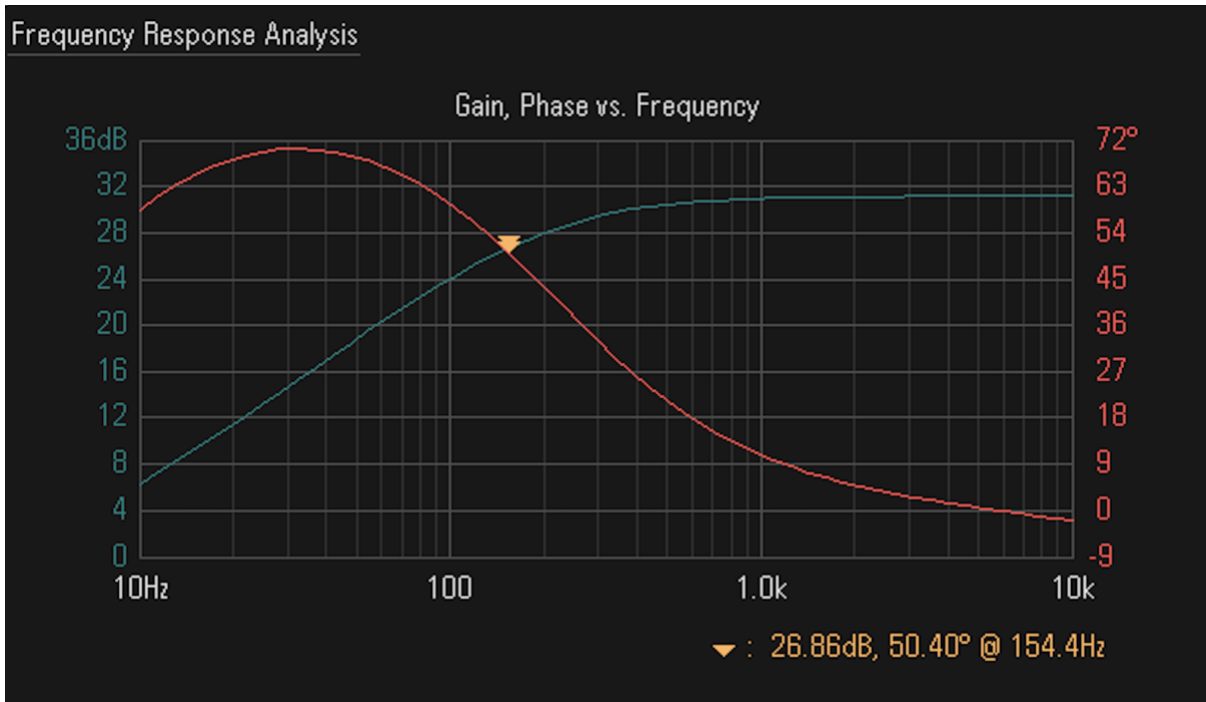


Figure 5-6: Protoboard frequency response of instrumentation amplifier circuit.

The equation for converting dB to linear scale,

$$y = 10^{\frac{y_{dB}}{20}} \quad (\text{Eq. 5-3})$$

Using equation 5-3, 26.3 dB equates to a gain of 20.65, which is almost exactly equivalent to the theoretical value of 20. Because the impedance values were calculated based on a desired gain of 20 just at 150 Hz, frequencies higher than 150 Hz get amplified a bit more, but this is acceptable given that 360 is the absolute minimum gain for the most prominent frequencies between 15-150 Hz. Frequencies higher than that will typically be smaller in magnitude anyway and will need more gain to begin with.

5.2.1 Common Mode Rejection Ratio (CMRR)

To further verify the effectiveness of the AD 8422 instrumentation amplifier, a test was conducted to calculate the common mode rejection ratio (CMRR). To do so, an 180 mV sine wave at a 150 Hz testing frequency was connected to only the positive input terminal (with the negative input terminal connected to 0 V), and then compared to when the same sine wave was connected to both the positive and negative terminals. Table 5-1 shows these results.

Measurement	Pk-Pk Voltage
Differential output voltage	3.58 V
Common Mode Output Voltage	320 μ V

Table 5-1: Differential vs common mode input comparison

Using the data of Table 5-1, the CMRR in dB was calculated through equation 5-4 to get 80.9 dB, where A_D is the differential amplitude and A_{CM} is the common mode amplitude. This equation obtains the ratio of the two measurements and converts to dB.

$$CMRR = 20 \log_{10} \left(\frac{A_d}{A_{cm}} \right) dB \quad (\text{Eq. 5-4})$$

5.2.2 Noise

In addition to verifying a sufficient common mode rejection ratio, the noise of the instrumentation amplifier was also tested by shorting both inputs of the AD 8422 to reference. A sampled table of data points was gathered and the mean of all data points was subtracted from each value in order to center the data. The root mean square (RMS) of the data set is then taken and divided by the gain of 360 across the frequency band between 20 - 800 Hz. After completing these steps, the noise sampled was approximately 2.58 μV RTI (referred to input).

This can be compared to the theoretical noise based on the data sheet given by,

$$\text{Total Noise} = \text{Noise Density} * \sqrt{\text{Bandwidth}} \quad (\text{Eq. 5-5})$$

The noise density of the AD 8422 given in the data sheet is 8nV. For the EMG front channel, the passband is between 20 - 800 Hz, giving a bandwidth of 780 Hz. Using Eq. 5-5, the theoretical total noise is 2.23 μV , very close to the measured 2.58 μV RTI.

5.3 High and Low Pass Filters

The high pass filter was created using a LMC6484 quad amplifier IC. Using the components selected in the design selection section, the Butterworth 2nd order filter was created and tested on a protoboard. Component values for the Butterworth filter were chosen and analyzed using a MATLAB script used in Clancy's lab, `butter_hi_design.m`, found in appendix D. This function takes in resistor, capacitor, desired gain values, and a cutoff frequency to output the remaining component values. The theoretical frequency response of the designed high pass filter was plotted with MATLAB and shown in Figure 5-7. A schematic was then created in Multisim (Figure 5-8) and tested for theory of operation. Decouple capacitors were added to the quad op-amp's power rails based off data sheet specifications of 1 nF.

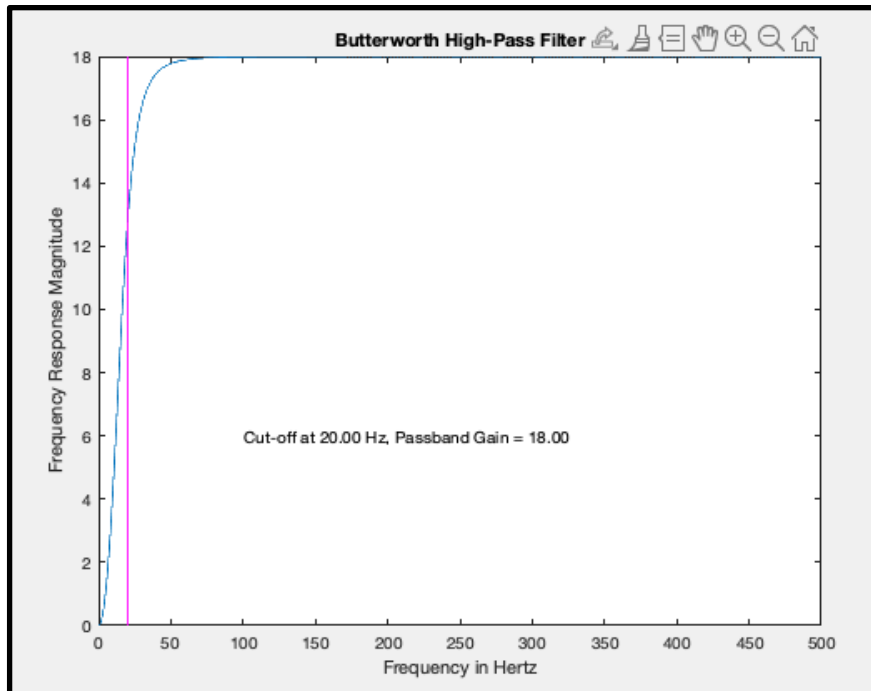


Figure 5-7: Theoretical high pass filter response with gain of 18.

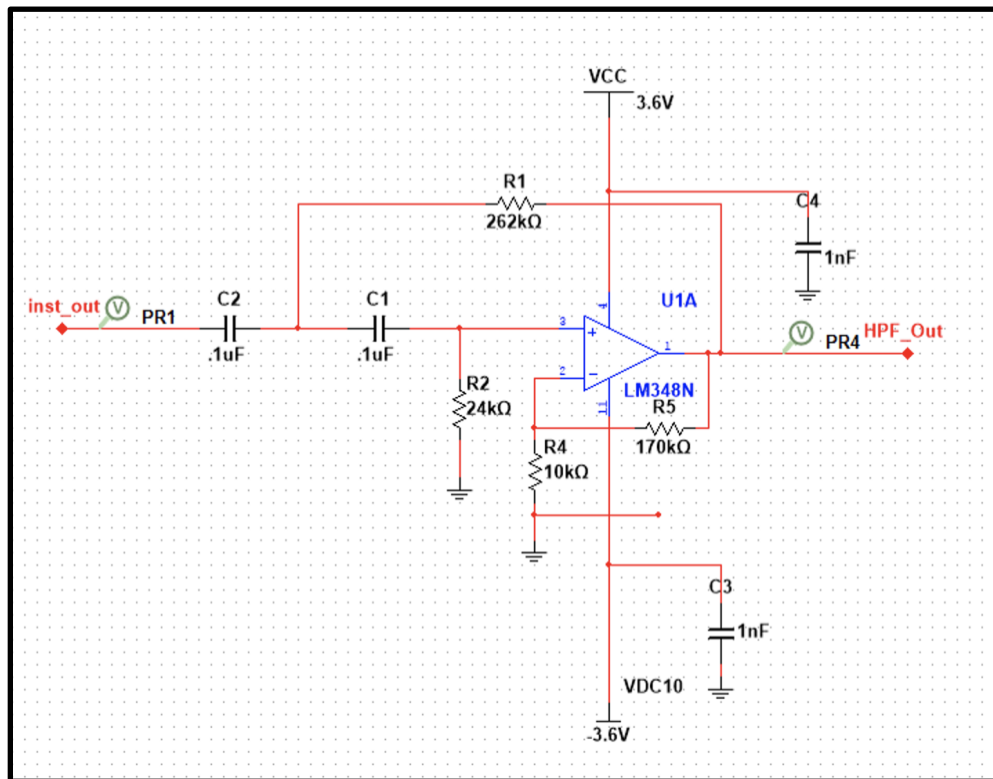


Figure 5-8: High pass filter schematic.

The high pass filter was added to the protoboard following the instrumentation amplifier stage and the frequency response of the combined instrumentation amplifier circuit and high pass filter was measured using 100 data points and collected through a Keysight oscilloscope, shown in Figure 5-9. This response shows a gain of 51 dB, which using eq. 5-3 gives a gain of 354. As expected, the roll-off with the high pass filter is a bit narrower, as it acts as an additional order to the instrumentation amplifier high pass filter.

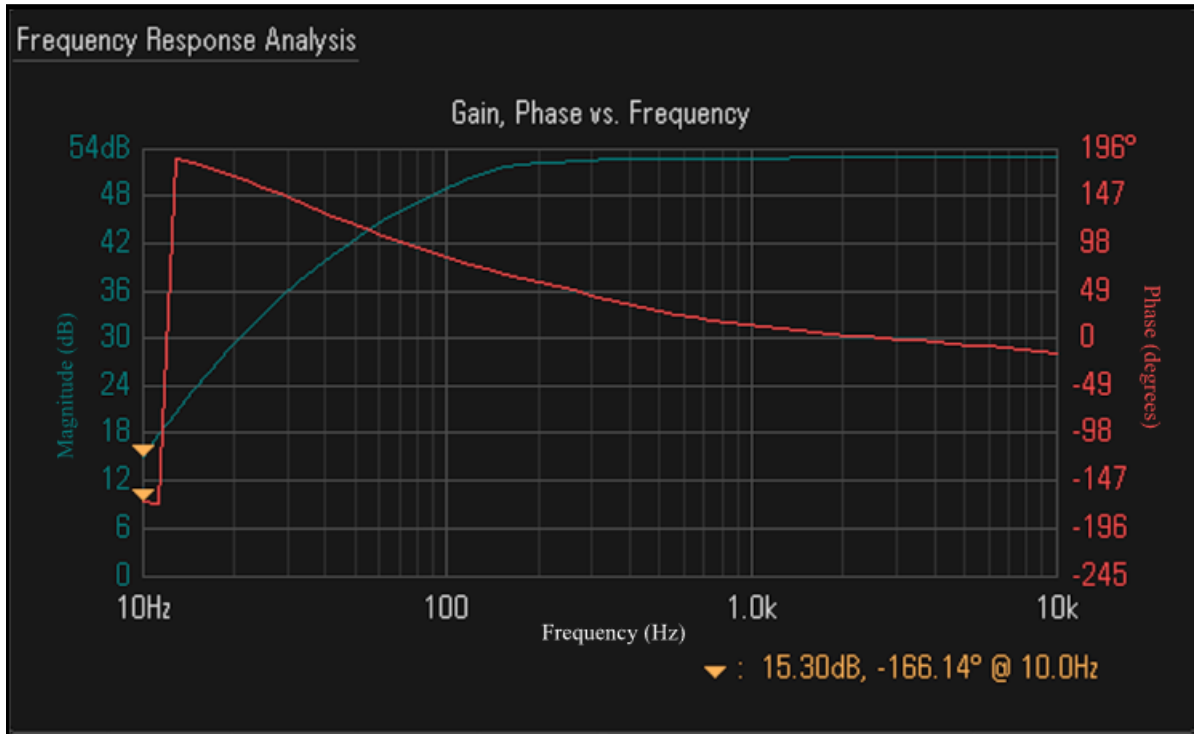


Figure 5-9: Frequency response of instrumentation amplifier followed by high pass filter

The low pass filter was constructed using a Sallen-Key Butterworth filter, similar to the high pass filter, but excluded the additional resistance and reference node included with the negative feedback in order to eliminate any gain. Like the high pass filter, a MATLAB script, Butter_lo_design.m, was used to determine the resistor and capacitor values for the desired gain of 1 and cutoff frequency of 800 Hz. Figure 5-10 shows the circuit schematic for the low pass filter with the chosen component values.

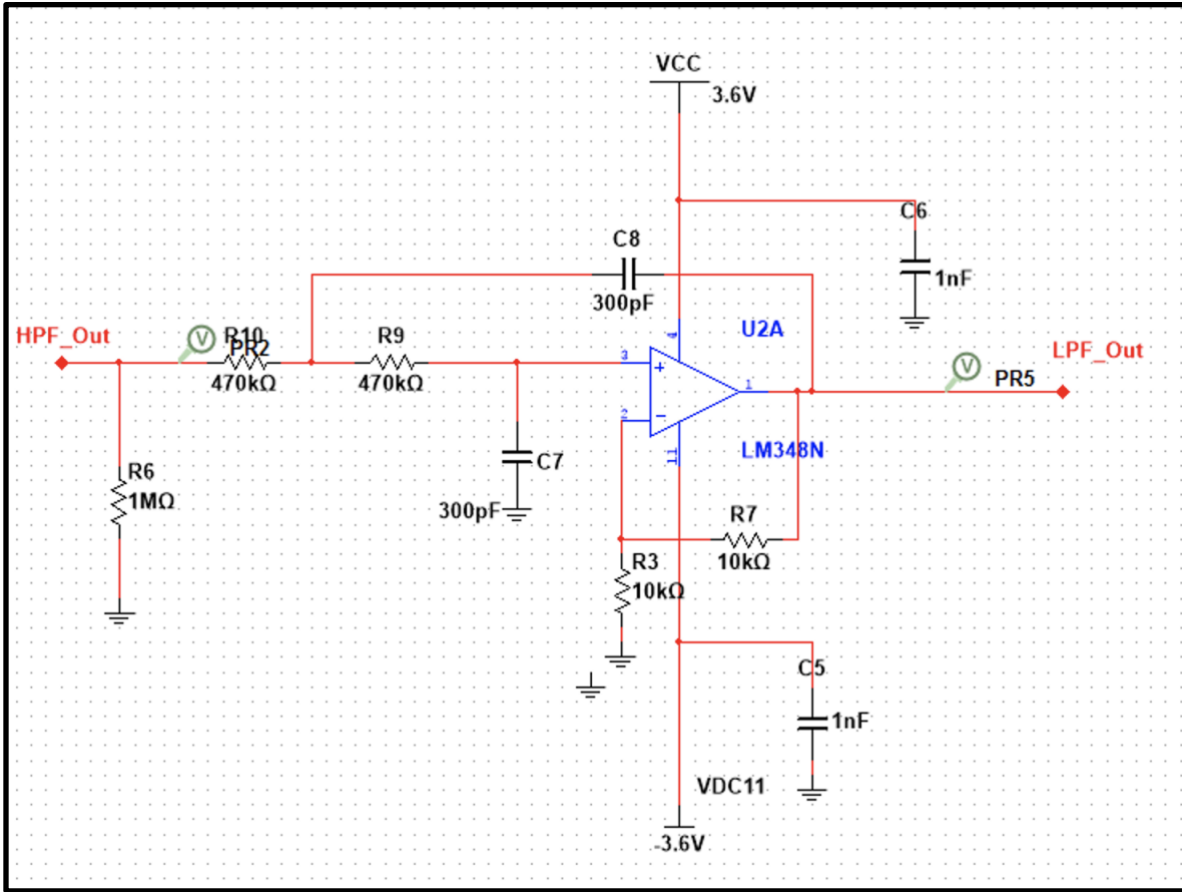


Figure 5-10: Low pass filter circuit schematic

Once prototyped on the protoboard, the low pass filter stage was connected to the high pass filter and instrumentation amplifiers to verify effective implementation. With all three stages connected together, the frequency response should match the final theoretical response for the minimum gain. Figure 5-11 shows this response which clearly shows a window that includes the required passband between 20 and 800 Hz. The roll-off for the high-frequency cutoff is wide, but it significantly reduces any signals beyond 1 kHz. From Figure 5-11, the magnitude at the tested frequency of 150 Hz is 51 dB or 354, just under the designed base gain of 360.

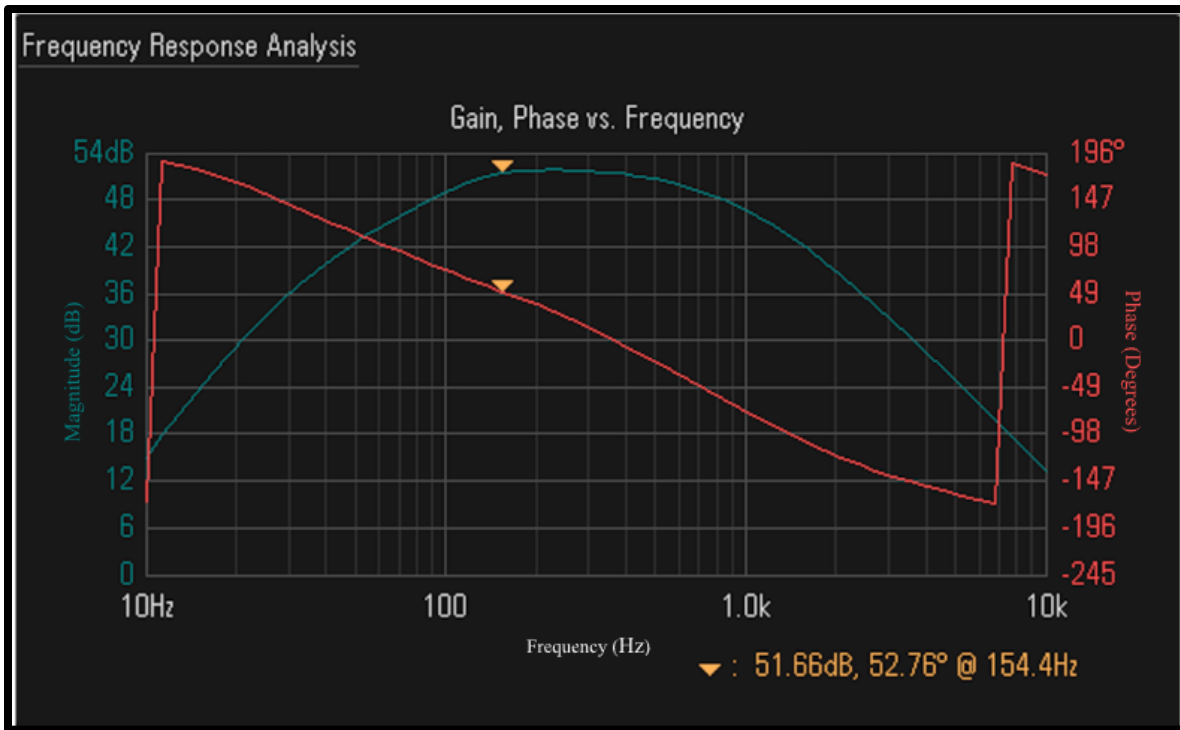


Figure 5-11: Instrumentation amplifier and bandpass filter circuit frequency response.

5.4 Selectable Gain

The selectable gain stage was created through a standard non-inverting amplifier with dip switches to allow various resistor values for R2. Eq. 5-1 shows the resistor values needed to obtain gains of two, four, eight, sixteen, thirty-two, sixty-four and one hundred twenty-eight while R2 is a 100 k Ω resistor. Figure 5-12 shows the schematic for this gain stage, where R2 is varied using dip switches to select between the resistor values in Table 5-2.

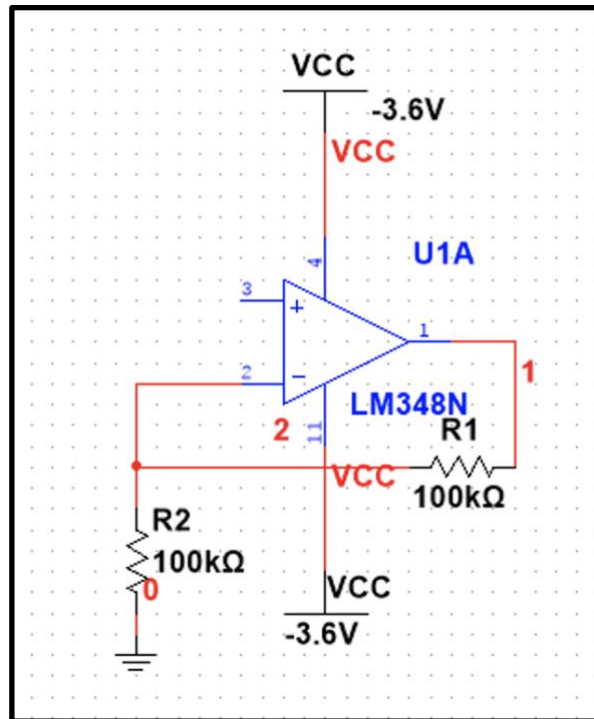


Figure 5-12: Non-inverting amplifier circuit.

Additional Selectable Gain Multiplier	Resistor Value	Theoretical Gain	Measured Gain
2	100 kΩ	2	1.99
4	33 kΩ	4	3.8
8	15 kΩ	7.98	7.97
16	6.8 kΩ	16	16.05
32	3.3 kΩ	32.25	31.19
64	1.5 kΩ	64.8	62.5
128	820 kΩ	131	125

Table 5-2: Selectable Gain Resistor Values

The selectable gain is controlled by supplying a current path to each one of these resistors individually. Switch one activates resistor 1, switch 2 resistor 2, etc. Thus, only one switch at a time should be in the conducting state. If further customization is desired, multiple of these switches can be turned on to activate resistors in parallel. Each of these selections was tested and the output was amplified by the expected value successfully.

5.5 Level shifter

The inclusion of a level shifter through a voltage regulator alongside an adder circuit effectively offset the output by +1.8 V. This adjustment ensures that the entire EMG signal range is optimally positioned for the unipolar ADC. Figure 5-13 shows the circuit schematic for the level shifter. The voltage regulator is an LM317, which is configured to output 1.8 V. This DC output is inputted into the fourth op-amp of the quad IC used.

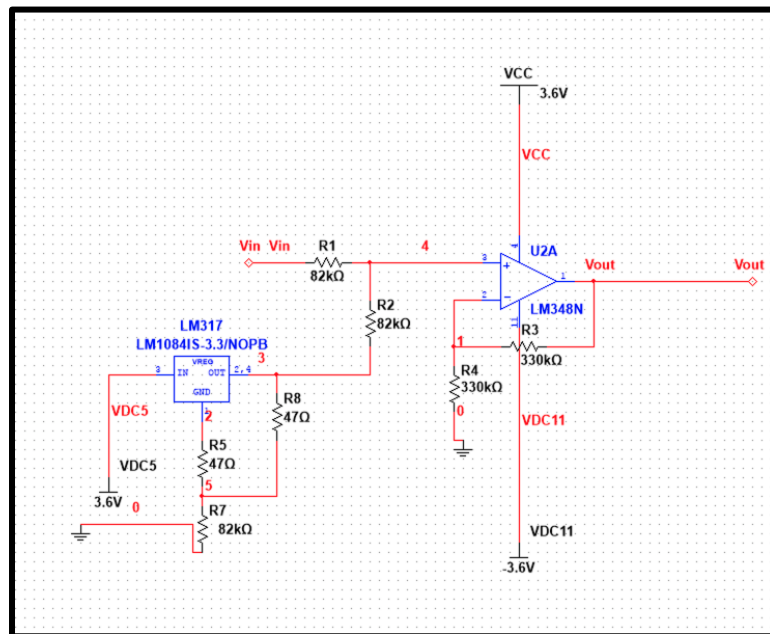


Figure 5-13: Level shifter schematic.

Figure 5-14 shows this offset for a 10 mV sine wave input (yellow) overlaid with the output (green) that stretches 3.63 V pk-pk and is offset 1.8 V by the level shifter. Note that the input wave has a smaller scale of 20 mV/division for easier viewing.

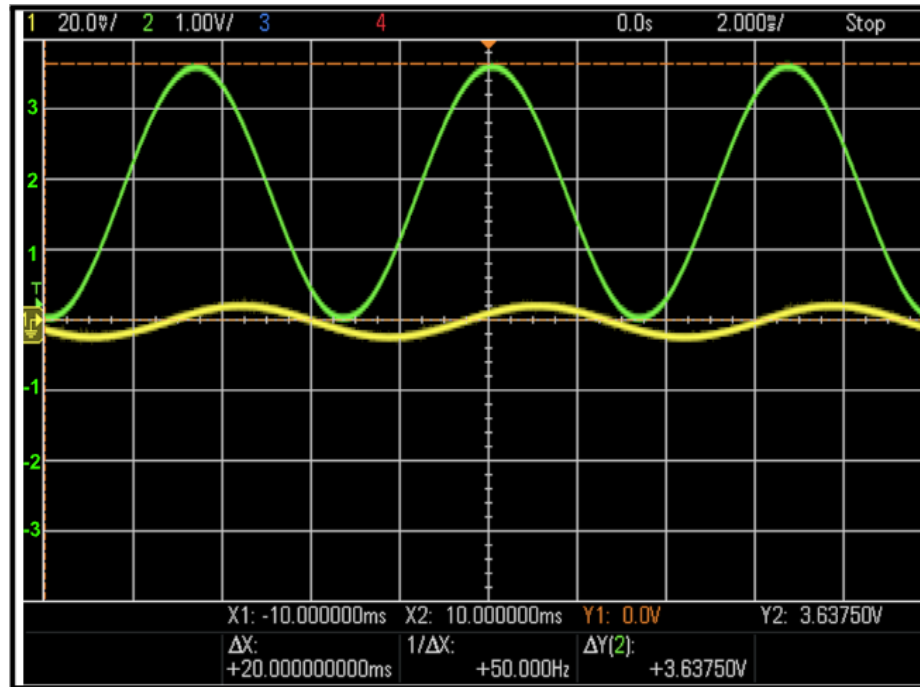


Figure 5-14: EMG front-end output with 1.8 V level shift vs time (2ms/div)

5.5.1 Future Improvements

For the purposes of piecing together our project, the use of a voltage regulator and adder circuit was used to achieve the level shift required to ensure that our acquired EMG signal is within a range that is usable by our ADC. However, this method may use a lot more power than it needs to. One alternative, if given a constant power source, would be using a voltage divider. While this voltage divider could be made of only resistors, a better option is one made of a resistor and a diode as in Figure 5-15. A level shifting circuit which includes a diode rather than a basic voltage divider is the better option because the output of a regular voltage divider is dependent on the supply voltage. However, the output of a level shifter using a diode is not supply dependent because while the diode is on there will always be a constant voltage drop over that diode and therefore the circuit always has a constant output voltage.

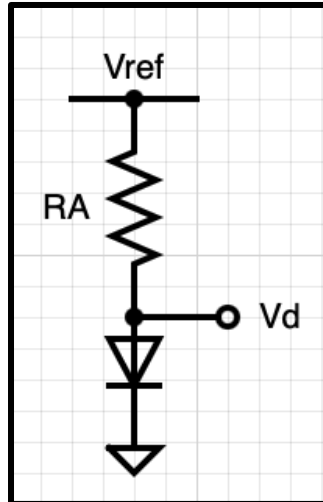


Figure 5-15: Voltage Divider using a Diode.

In order to use this method, the new circuit must be evaluated to ensure that it will work properly when implemented in the place of the voltage regulator and adder that is currently in use. The new circuit is shown in Figure 5-16.

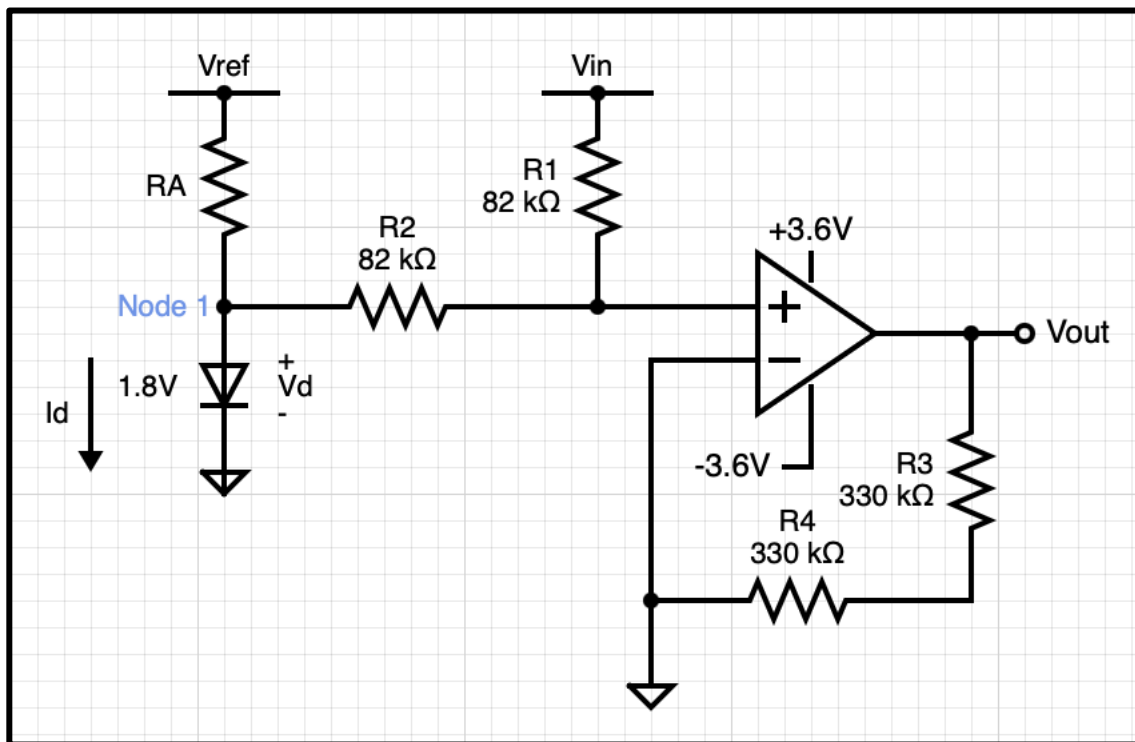


Figure 5-16: Level Shifter Using a Resistor and a Diode

The output of this circuit is the level shifted EMG signal which will go to the microcontroller. In this case, V_{REF} is the positive battery voltage which has a value between 3.6 V and 4 V as the battery used to power the whole system loses its charge over time. V_{in} on the other hand, is the EMG signal arising from the instrumentation amplifier as well as the filters. I_D is the current flowing down through the diode and R_A is the resistor we are trying to find which allows I_D to flow in the correct direction. In addition, R_1 and R_2 form the voltage divider that the adder portion of the circuit uses to evaluate the EMG signal before it moves on to the next stage of the circuitry.

The diode used must be a 1.8 V diode to ensure proper level shifting. This new circuit is evaluated using Kirchhoff's current law (KCL) to ensure that the diode is on (forward biased) rather than off (reverse biased). This evaluation about Node 1 is used to make sure that current never attempts to flow back up through the diode but rather always flows down through the diode to ground. The same evaluation also allows us to find the edge cases for which the circuit will work as desired so that appropriate circuit components can be chosen. These calculations are as follows:

Writing KCL at Node 1:

$$I_D = \frac{V_{REF} - V_D}{R_A} + \frac{V_{IN} - V_D}{R_1 + R_2} \quad (\text{Eq. 5-6})$$

In order for the circuit to function as needed, I_D must be greater than zero. In addition, V_{IN} can range from $-V_{REF}$ to $+V_{REF}$ since it is the output of all the previous stages of the circuit, but also can not exceed the range of our bipolar power supply. V_D must also be a positive value for I_D to be positive.

Node 2:

Consider three cases for the equation I_D . The first is where $V_{IN} = -V_{REF}$. If that is the case, the second half of the equation for I_D is a large negative number. The second case is where $V_{IN} = 0$ V. If $V_{IN} = 0$ V, the second half of the equation is still equal to a negative number, but it is much closer to zero than in the previous case. The final case is where $V_{IN} = V_{REF}$ which results in the whole equation for I_D being positive. Therefore, the worst case (lowest value of I_D)

occurs when $V_{IN} = -V_{REF}$. From now on, we consider this the worst case and these are the conditions used to find an appropriate value of R_A .

Therefore, KCL at Node 1 becomes:

$$I_D = \frac{V_{REF} - V_D}{R_A} + \frac{-V_{REF} - V_D}{R_1 + R_2} > 0$$

It is important to note that both R_1 and R_2 have the same value so that there is no scaling of the inputs when the adder is used, which will make $R_1 + R_2 = 2R$.

$$\frac{V_{REF} - V_D}{R_A} + \frac{-V_{REF} - V_D}{2R} > 0$$

$$-\frac{-V_{REF} - V_D}{2R} < \frac{V_{REF} - V_D}{R_A}$$

$$-\frac{-1(V_{REF} + V_D)}{2R} < \frac{V_{REF} - V_D}{R_A}$$

$$\frac{V_{REF} + V_D}{2R} < \frac{V_{REF} - V_D}{R_A}$$

$$2R \cdot V_{REF} - 2R \cdot V_D > R_A \cdot V_{REF} + R_A \cdot V_D$$

$$2R(V_{REF} - V_D) > R_A(V_{REF} + V_D)$$

$$R_A(V_{REF} + V_D) < 2R(V_{REF} - V_D)$$

$$R_A < \frac{2R(V_{REF} - V_D)}{V_{REF} + V_D} \quad (\text{Eq. 5-7})$$

The existing level shifter and adder circuit uses $R_1 = R_2 = 330 \text{ k}\Omega$ and V_D will always be 1.8 V as long as the diode is on. Between the two coin cell batteries being used as our power supply, V_{REF} can be anywhere between +3.6 V and +4 V and the circuit will still function as intended. A value of $V_{REF} = 3.6 \text{ V}$ is the worst case because it is the smallest value of the existing battery our team is using for which our system remains fully functional and is also the condition for which the smallest positive value of I_D occurs. If V_{REF} is 3.6 V R_A can be calculated as follows:

$$R_A < 2(330,000)\left(\frac{3.6 - 1.8}{3.6 + 1.8}\right)$$

$$R_A < 219999.9998\Omega \approx 220\text{ k}\Omega$$

In order to ensure that the value of R_A leaves a little bit of room for component tolerances and exact power supply value so that I_D is never zero or negative, the value of R_A used will be 200k Ω . Using these calculations, resistor values that would be used to satisfy our use of the Circuit in Figure 5-11 are in Table 5-3.

Resistor	Value
R_A	200 k Ω
R_1	330 k Ω
R_2	330 k Ω

Table 5-3: Resistor Values for the Level Shifter Circuit of Figure 5-11

While $R_A = 200\text{ k}\Omega$ satisfies the calculations, Multisim was used to double check the current I_D given various values of R_A for each case of V_{IN} previously discussed when V_{REF} is between 3.6 V and 5 V. These values are located in Table 5-4 where the smallest positive value of I_D is in green and all negative values of I_D are in red.

R_A	V_{REF} and V_{IN}	I_D
200k Ω	$V_{REF} = V_{IN} = +3.6\text{ V}$	11.7 μA
200k Ω	$V_{REF} = V_{IN} = +3.6\text{ V}$	16.3 μA
200k Ω	$V_{REF} = V_{IN} = +3.6\text{ V}$	20.8 μA
220k Ω	$V_{REF} = V_{IN} = +4.3\text{ V}$	10.9 μA
220k Ω	$V_{REF} = V_{IN} = +4.3\text{ V}$	15.2 μA
220k Ω	$V_{REF} = V_{IN} = +4.3\text{ V}$	19.4 μA
240k Ω	$V_{REF} = V_{IN} = +5\text{ V}$	18.2 μA
240k Ω	$V_{REF} = V_{IN} = +5\text{ V}$	15.3 μA
240k Ω	$V_{REF} = V_{IN} = +5\text{ V}$	10.2 μA

200k Ω	$V_{REF} = +3.6 \text{ V}, V_{IN} = -3.6 \text{ V}$	818nA
200k Ω	$V_{REF} = +4.3 \text{ V}, V_{IN} = -4.3 \text{ V}$	3.26 μA
200k Ω	$V_{REF} = +5 \text{ V}, V_{IN} = -5 \text{ V}$	5.70 μA
220k Ω	$V_{REF} = +3.6 \text{ V}, V_{IN} = -3.6 \text{ V}$	-1.35pA
220k Ω	$V_{REF} = +4.3 \text{ V}, V_{IN} = -4.3 \text{ V}$	2.12 μA
220k Ω	$V_{REF} = +5 \text{ V}, V_{IN} = -5 \text{ V}$	4.24 μA
240k Ω	$V_{REF} = +3.6 \text{ V}, V_{IN} = -3.6 \text{ V}$	-682nA
240k Ω	$V_{REF} = +4.3 \text{ V}, V_{IN} = -4.3 \text{ V}$	1.17 μA
240k Ω	$V_{REF} = +5 \text{ V}, V_{IN} = -5 \text{ V}$	3.03 μA
200k Ω	$V_{REF} = +3.6 \text{ V}, V_{IN} = 0 \text{ V}$	6.27 μA
200k Ω	$V_{REF} = +4.3 \text{ V}, V_{IN} = 0 \text{ V}$	9.77 μA
200k Ω	$V_{REF} = +5 \text{ V}, V_{IN} = 0 \text{ V}$	13.3 μA
220k Ω	$V_{REF} = +3.6 \text{ V}, V_{IN} = 0 \text{ V}$	5.45 μA
220k Ω	$V_{REF} = +4.3 \text{ V}, V_{IN} = 0 \text{ V}$	8.64 μA
220k Ω	$V_{REF} = +5 \text{ V}, V_{IN} = 0 \text{ V}$	11.8 μA
240k Ω	$V_{REF} = +3.6 \text{ V}, V_{IN} = 0 \text{ V}$	4.77 μA
240k Ω	$V_{REF} = +4.3 \text{ V}, V_{IN} = 0 \text{ V}$	7.69 μA
240k Ω	$V_{REF} = +5 \text{ V}, V_{IN} = 0 \text{ V}$	10.6 μA

Table 5-4: I_D for Each Case of V_{REF} and V_{IN} for Various R_A

After investigating the relationship between the value of R_A given various conditions of V_{REF} and V_{IN} . It was found that for a given value of R_A that was greater than or equal to Eq. 5-7, it is possible to get a negative value of I_D . Since the initial values of R_A used to find the values of I_D are relatively far apart, they are not sufficient enough to find exactly where the value of I_D becomes negative. The values in the tables found in Appendix A were obtained through Multisim and used to create Figures 5-17 and 5-18 below.

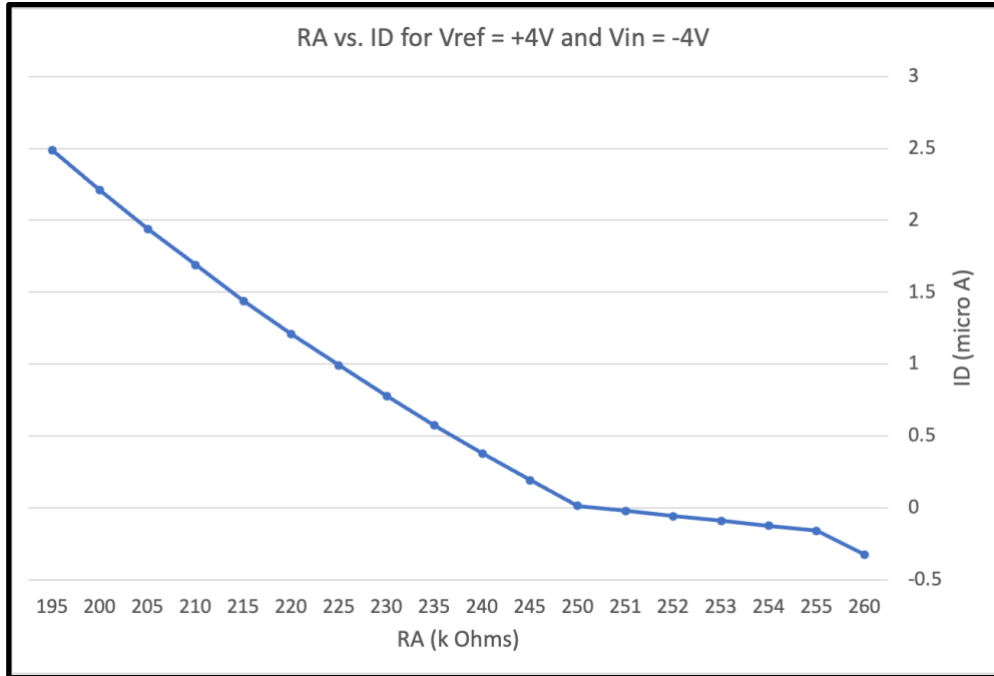


Figure 5-17: R_A VS. I_D for $V_{REF} = +4V$ and $V_{IN} = -4V$

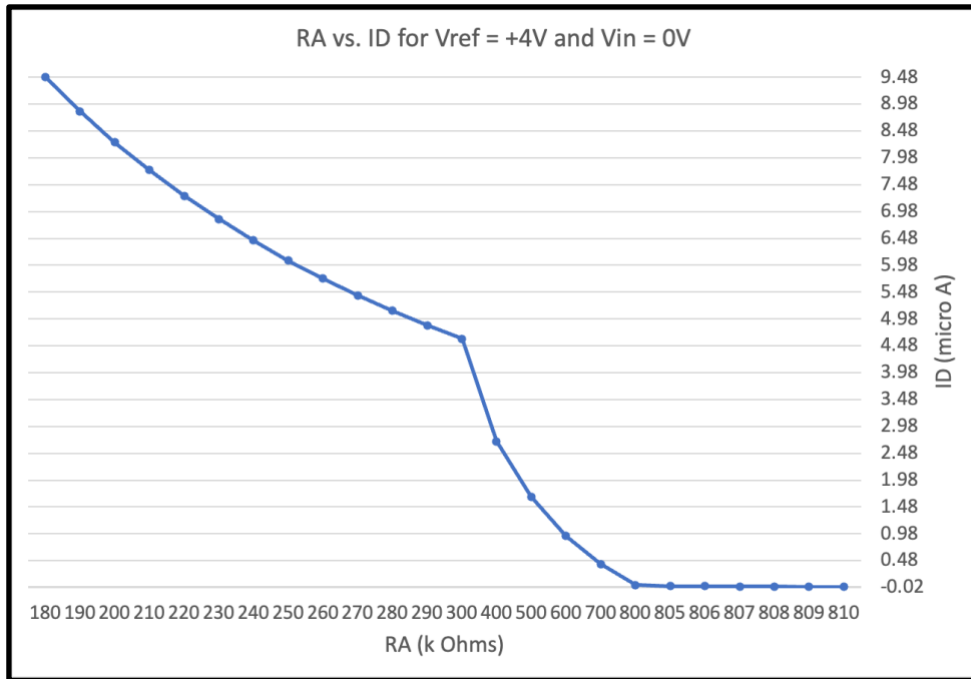


Figure 5-18: R_A VS. I_D for $V_{REF} = +4V$ and $V_{IN} = 0V$

The data collected for $V_{REF} = V_{IN} = +4V$ was not turned into a graph because, for all values of R_A between $120\text{ k}\Omega$ and $2\text{ M}\Omega$ the value of I_D was positive and was nowhere close to

becoming negative under the conditions given until R_A becomes very large. Since R_A would need to be so large, that value is not the edge case needed to ensure proper function of the circuit and was therefore not transferred into a plot.

The data for the other two major conditions of V_{REF} and V_{IN} on the other hand are plotted in Figures 5-17 and 5-18. These plots are important to demonstrating the limitations on the value of R_A that can be used in our circuit. For the condition where $V_{REF} = +4 V$ and $V_{IN} = -4 V$ (Figure 5-17), the current I_D becomes zero somewhere between values of R_A equal to 250 k Ω and 251 k Ω . The same testing was done for $V_{REF} = +4 V$ and $V_{IN} = 0 V$ (Figure 5-18), in that case more current flowed through R_A resulting in I_D passing through zero at a much higher value (R_A between 806 k Ω and 807 k Ω). When equation 5-7 is evaluated using the conditions discussed above, the calculated values are consistent with those that were obtained through simulation. However, it is important to use the value of R_A for which the current never reaches zero or becomes negative making the smaller values of R_A more desirable for our application.

Based on the data collected, the condition for $V_{REF} = +4 V$ and $V_{IN} = -4 V$ does in fact result in the worst case scenario (smallest value of I_D). This scenario reinforces the reasoning behind the initial calculations of R_A as well as the discussion of Table 5-4. In each of the three cases, current (I_D) decreases with increasing values of R_A as expected. Therefore, using an R_A value which is less than that of the calculated value when Eq. 5-7 is used for a given value of V_{REF} , between 3.6 V and 5 V, leaves room for component tolerances.

Overall, at a nominal voltage of $V_{REF} = +4 V$ and $V_{IN} = -4 V$, R_A needs to be a few kilo ohms less than 250 k Ω for proper circuit operation. Based on these calculations, the maximum value of R_A increases with increasing V_{REF} . Due to this relationship between R_A and V_{REF} along with the existing set-up of our circuit, an R_A less than or equal to 200 k Ω keeps the circuit in proper working order. In addition, the power consumption of the level shifter is equal to the value of R_A multiplied by the current through R_A squared. Therefore, the power consumption is 86.528 μ W. Each of the four voltage regulators in our existing circuit, as discussed earlier in Section 5.5 draws about 13 mA of current at a nominal 3.6 V. In which case, the total power consumption of one voltage regulator is 46.8 mW and that of all the voltage regulators is 187.2 mW. Based on each of these two values of power consumption, the diode level shifter is about

541 times more power efficient than the use of one voltage regulator and about 2164 times more power efficient than the existing level shifter using four voltage regulators. Therefore, the diode level shifter as discussed above is a viable option for future improvements to our prototype by improving the battery life of our prototype.

5.6 Front-End EMG Acquisition

The final data collected for the entire analog front end when isolated from the rest of the system was a basic EMG signal test. For a simplified test, we placed three electrodes on the forearm using sticky electrodes. Two served as positive and negative terminals for an EMG measurement of muscles in the forearm, and one on the wrist as a body reference. Figure 5-19 shows this setup.



Figure 5-19: EMG electrodes connected to the forearm.

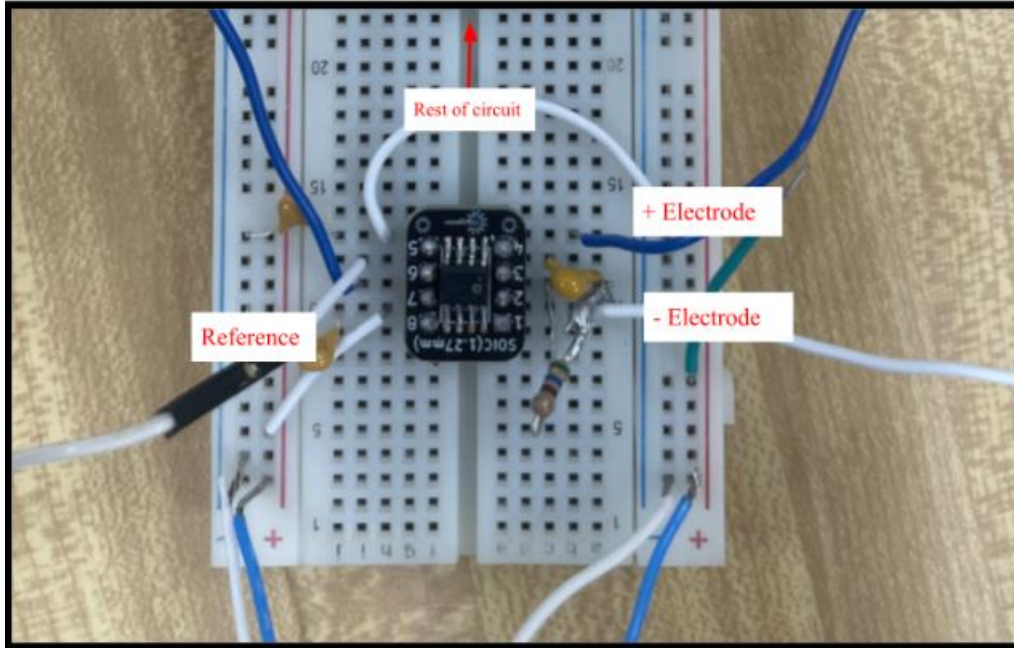


Figure 5-20: EMG electrodes input to the instrumentation amplifier

Using a selected gain of 1,140, the output of the front end for a *rested* forearm can be seen in Figure 5-21. The pk-pk output voltage has a voltage span of approximately 150 mV, which divided by gain of 1,140 is 132 μV . The noise shown is significantly attenuated, with the most noticeable variations in the 60 Hz range, as a result of power line interference.

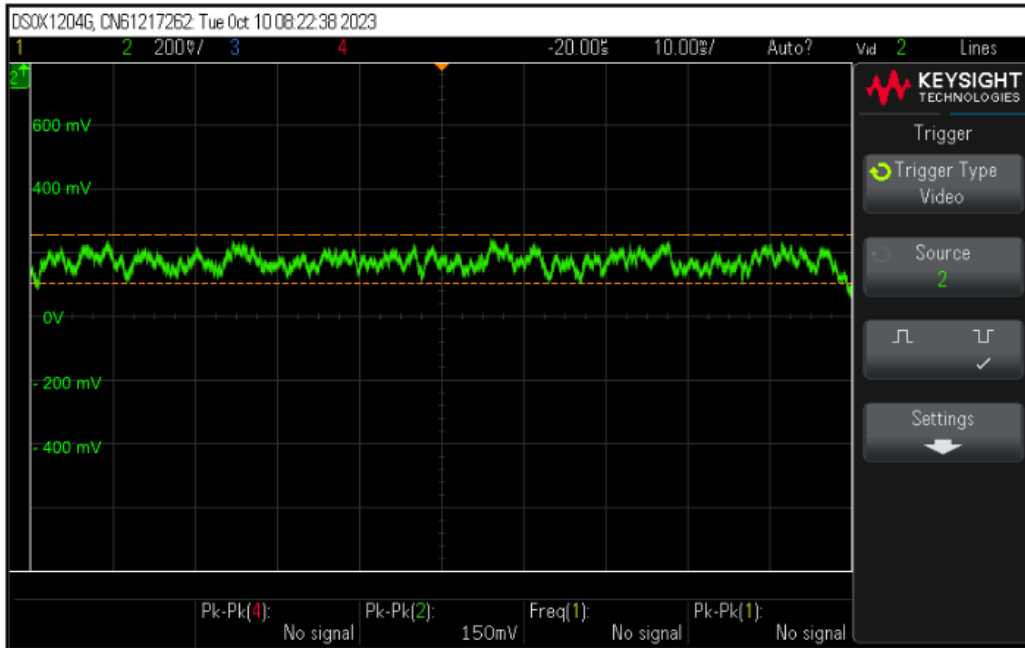


Figure 5-21: Rested forearm EMG output vs time (200mV/div) on oscilloscope

The subject then performed a few muscle contractions. The output for a high-effort contraction is shown in Figure 5-22 below, which uses the same y-axis scale as Figure 5-20.



Figure 5-22: Forearm contraction front-end output viewed through an oscilloscope using the same y-axis scale as Figure 5-21.

The signal in Figure 5-22 depicts a successful EMG acquisition. The resting input in Figure 5-21 has a pk-pk value of 150 mV (as seen on the bottom row of the scope). In the contracted muscles Figure (5-22), the pk-pk voltage is >1.3 V. While this is not taking advantage of the full range of the ADC, 0-3.6 V, the signal could be further amplified using the selectable gain to do so. The shape of the signal shows the summed motor unit action potentials (i.e., the interference pattern) of the muscle. The firing of groups of muscle fires varies in length depending on the muscle and the peaks fire at spontaneous times in the data and sometimes build off each other.

Figure 5-22 shows little noise being amplified since both 5-21 and 5-22 are using the same y-axis scales. This suggests successful acquisition of EMG signals and providing gain to the correct range of frequencies (20 Hz - 800 Hz). The subject in this data was moving as their muscle contracted, so motion artifact and altering DC offset would have been prominent if not for properly functioning filters.

5.7 Power Performance

LIR2450 batteries were used for this project and are rated at 3.6 V with a capacity of 120 mAh. The setup used for the analog front end consists of two of these cells in series to form bipolar power rails, with the midpoint taken as the 0V reference potential. In addition to the front end, the positive supply rail is also used to power the MCU. Because these batteries are compact and limited in capacity, the voltage output needs to be verified that it will remain at 3.6 V or above for the length of intended use. To ensure this, a battery test (using one battery) was performed with a 51 Ω load, which produced a current of 70 mA. With a capacity of 120 mAh, the battery is expected to last 1 hour and 42 minutes. Table 5-5 shows the battery voltage as a function of time collected from this test. Figure 5-23 shows the capacity vs. voltage plot, and Figure 5-24 shows the capacity vs. time plot for this stress test. It should be noted that the current draw in this test is much higher than the typical operation and was strictly used for stress testing. Even so, the battery still remained above 3.6 V for 75 minutes.

Time (minutes)	Voltage (V)	% of Full Capacity
0	4.3	100%
9	4.1	91%
14	4	86.30%
25	3.9	75%
47	3.7	54%
55	3.6	45%
67	3.6	34%
75	3.6	26%
77	3.5	25%

Table 5-5: Battery drain test data.

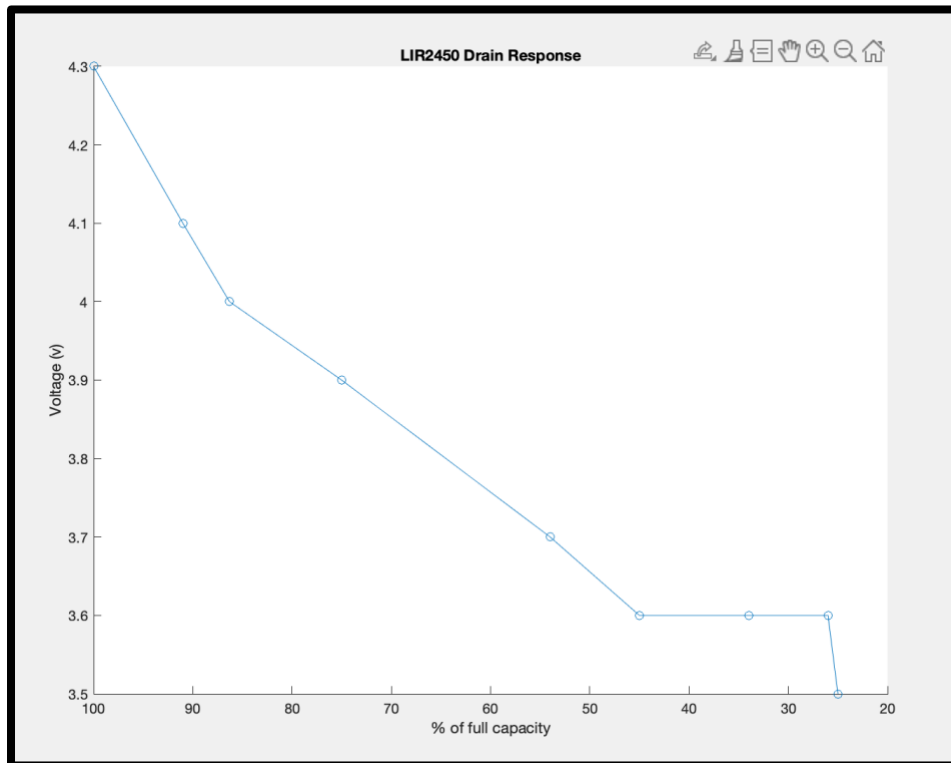


Figure 5-23: Battery drain voltage vs. percent capacity.

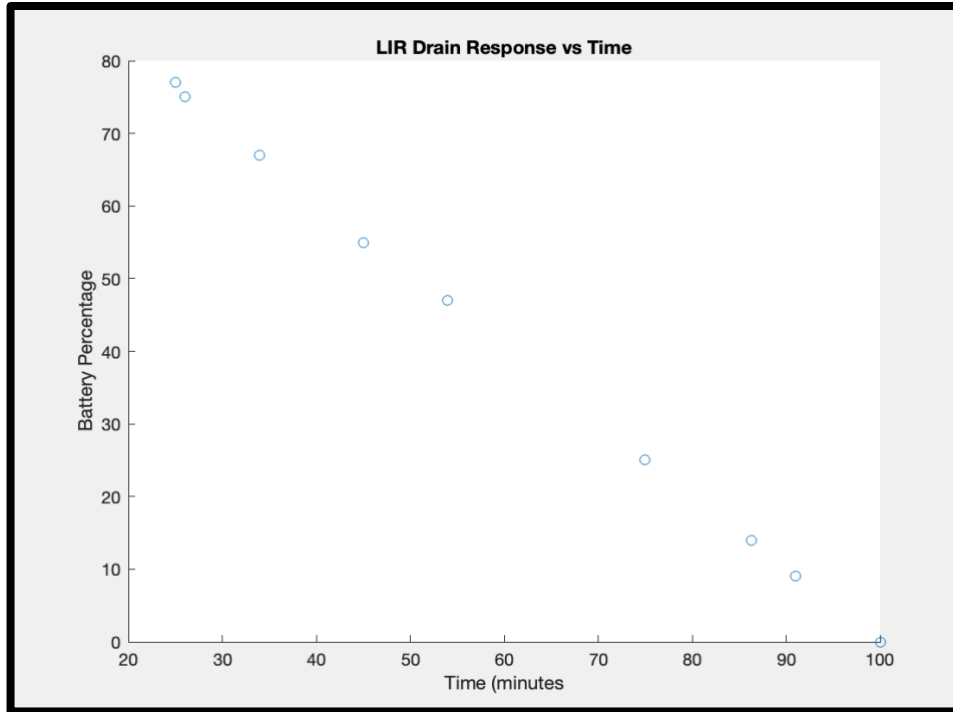


Figure 5-24: Battery drain vs Time (minutes)

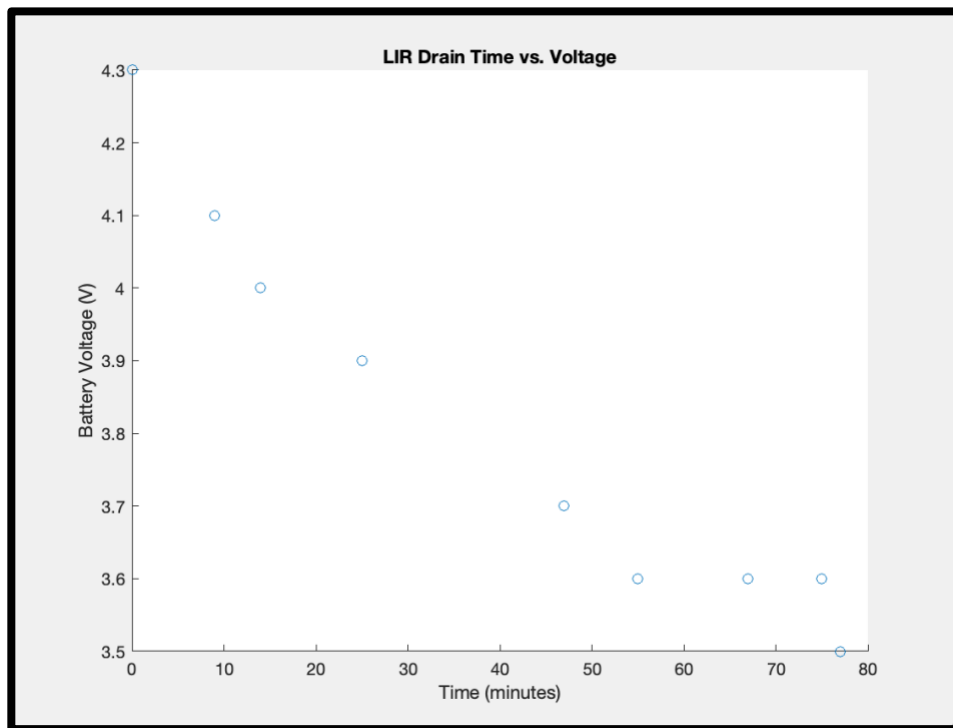


Figure 5-25: Battery voltage vs. drain time

5.8 Front End Discussion

Using the information gathered in our testing, the analog front end functions as needed for our purposes and satisfies our requirements as laid out by Table 3-1. Given our setup, there is a minimum of 3.6 V provided by our power supply for a sufficient wear time of four hours in a lab setting. In addition, since each of the stages has either the expected gain or is very close to the expected gain, in addition to the selectable gain stage, it is easy to satisfy the requirement for a minimum gain of 360; and gain is able to go up to 46,000. Each stage of the front end functioned as expected as well. The instrumentation amplifier acts as a high pass filter with a gain of about 20 as seen in Figure 5-4. The high pass filter successfully adds a gain of 18 to the output of the instrumentation amplifier and attenuates frequencies below 20 Hz. The low pass filter attenuates signals past 800 Hz, which when combined with the previous two stages creates a bandpass filter with a passband of 20 - 800 Hz with a gain of 360. The selectable gain stage can then multiply this gain further, successfully ranging from 360 to 46,000. The output signal is then level shifted by 1.8 V which ensures that the entire signal can be read by an ADC ranging from 0 - 3.6 V.

The front-end design can later be improved upon by optimizing the power supply system as well as by improving compactness and noise reduction. Our design uses a bi-polar power supply using two rechargeable cell batteries in series. Because the positive supply is powering the front end and the microcontroller, and the negative supply is only powering the front end, the use of two cells does not increase wear time by a factor of two. This setup was implemented only for the purpose of simplifying the bi-polar power requirements of the analog components. In the future, a charge pump can easily be added between a power supply consisting of a single battery and the instrumentation amplifier in order to create a bipolar supply using a single battery rather than the two batteries being used for our tests. In addition to simplicity, this would decrease the footprint of the overall package.

Increasing the CMRR and reducing the noise produced by amplifiers any further would likely be challenging, as the AD 8422 amplifier appears to be relatively standard in EMG applications. The components used, however, do take up a significant amount of space and are not easily customizable. In order to adjust the pass band of the filters, the filter order, and even

fine-tuning the gain, removing, adding and or modifying components is required. Using a higher bit ADC would allow for more customization, as digital inputs could be used for gain, filtering, or user modes, which would in turn reduce the physical footprint of circuitry and increase the digital modifications. In the future, the use of a higher-bit ADC should be taken into consideration, along with the drawbacks of additional power consumption and the need for additional hardware. A device such as the ADS 1292 could also be a consideration and logistics of the feasibility of this is discussed further in Section 6.

Using the information gathered from the output of the EMG signal and the frequency response, the filters used could also be sharpened by using filters with orders higher than a second. While this would use more power draw and increase the physical footprint of the circuit, the high-frequency noise that is partially visible has the potential to be reduced further. This would help to produce a clearer signal, although the 2nd-order Butterworth design currently provides sufficient results for the purposes of our research.

5.8.1 Alternative Power Supply System

As previously mentioned in Section 5.8, two coin cell batteries were used to create a bipolar power supply. However, this method did not double the wear time of our product, but rather provided a bipolar supply. Overall, one battery in the place of two would be an improvement to our design. However, one battery on its own takes away the existing bipolar power supply needed to power the remainder of our circuit. A charge pump is one solution to this issue.

A charge pump uses various components that can be switched between in order to store as well as transfer energy which will result in a different constant voltage source (Hardwarebee, 2022). Such components are usually capacitors, which are individually charged and then put in series. Since each capacitor is charged individually and then placed in series, this is where the switching function of the pump comes into play. In order to achieve higher output voltages, more stages of charged capacitors are connected together (Hardwarebee, 2022).

While the general function of a charge pump has been discussed, our application needs both a constant positive and constant negative output supply. Each of these outputs have slightly different topologies which will be discussed later in this section, but each has the same basic

mode of operation. In the case of the constant negative supply that a charge pump can provide, this is achieved by switching the locations of the components used which will change the output to a negative voltage. A very basic example of a positive charge pump is located in Figure 5-26 and a negative charge pump in Figure 5-27. These diagrams are the simplest representations of charge pumps there are. In each case, the diodes are used to aid in keeping the capacitor charged as it discharges to provide the charge pump output (Hardwarebee, 2022).

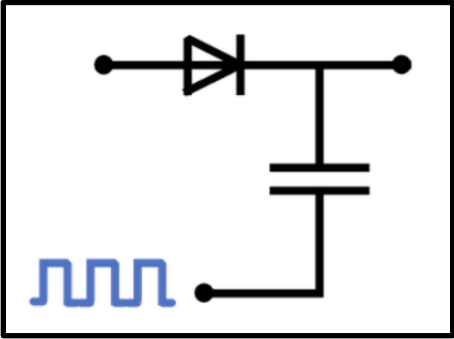


Figure 5-26: Positive Charge Pump (Hardwarebee, 2022)

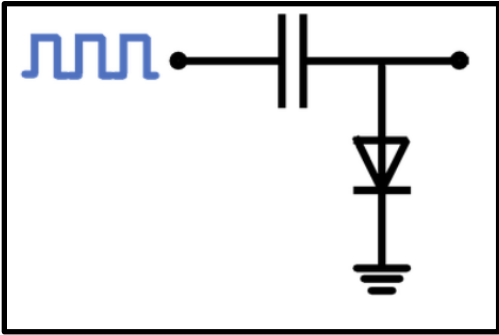


Figure 5-27: Negative Charge Pump (Hardwarebee, 2022)

The input to a charge pump in our application would be a DC voltage coming from a battery. That input is not the one being looked at in Figures 5-26 and 5-27. The square wave input seen in the figures is used to explain how the charge pump works. This input is a square wave from 0 V to V_{DC} in Figure 5-26 and between 0 V and $-V_{DC}$ in Figure 5-27. In each case, when the input is at 0 V, the diode(s) will be on and the capacitor will be charging to the $\pm V_{DC}$ value and the output of the circuit will be either $\pm V_{DC}$. In a similar fashion, when the input square wave is the given $\pm V_{DC}$ the capacitor has already been charged, the diode off and the output of $\pm 2 V_{DC}$ (Hardwarebee, 2022).

In addition, as previously mentioned in this section, these two basic circuits can have additional stages to aid in doubling or even tripling the input voltage given. An example of a charge pump that would take in the value provided by our battery and output a constant ± 5 V power supply is part number LM27762 from Texas Instruments and can be seen in Figure 5-28 below (Texas Instruments, LM27762).

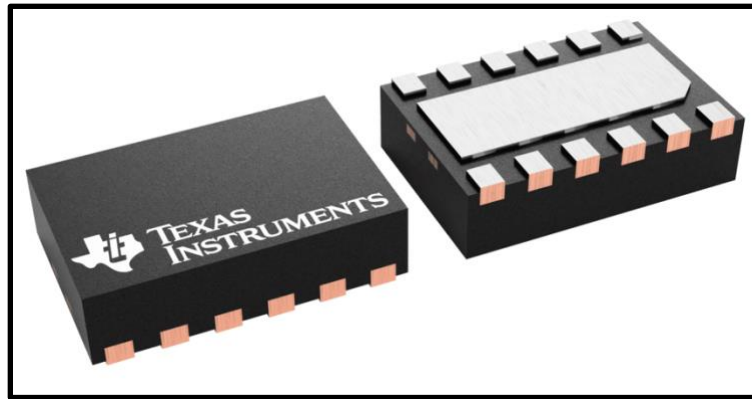


Figure 5-28: Texas Instruments Charge Pump (LM27762) (Texas Instruments, LM27762)

While there are many charge pumps available for purchase, many of them output much less than or much more than ± 5 V. Due to this voltage difference from what is needed as well as reasonable for our application, the Texas Instruments charge pump discussed above is one of the best options for our application. Through the use of a charge pump such as this, the power supply is now a constant ± 5 V rather than the ± 3.6 V to ± 4 V provided by our existing two-battery supply. With a constant ± 5 V supply, the voltage regulators that are in the existing circuit will not be needed and only one of our two cell batteries will be needed. In order to integrate a charge pump into the existing circuit design, one of our two coin cell batteries would be the input to the charge pump itself and the outputs of the charge pump would be the new bipolar power rails that will be used by the rest of the circuit. The new setup can be seen in Figure 5-29 below.

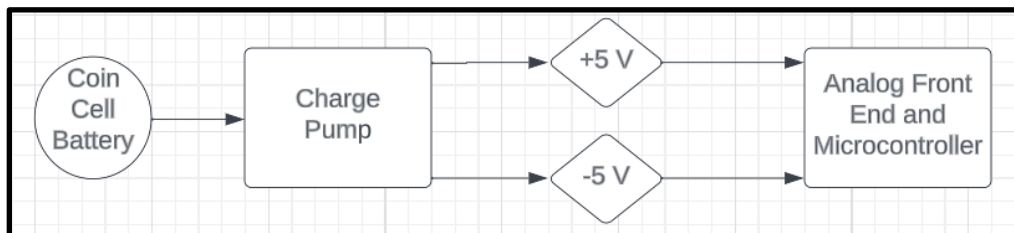


Figure 5-29: Analog Front End Using a Charge Pump.

Using the new topology in Figure 5-29, the remainder of the circuit will remain unchanged. The level shifter will still be needed to offset the EMG signal to a range that is readable by our ADC. However, the Nordic device can operate off +5 V while the op-amps operate off ± 5 V and the components used to obtain the gain of each stage of our analog front end are not dependent on supply voltages. Therefore, there would simply be one extra stage of the circuit located after the battery and before the analog front end to integrate a charge pump into our circuit design.

Each charge pump will be slightly different and the datasheet for the chosen charge pump needs to be reviewed and understood before it can be integrated into our circuit. In terms of the Texas Instruments LM27762 charge pump, some additional circuit components are needed to ensure the charge pump is working in order to provide the desired output. This setup is located in Figure 12 of the Texas Instruments data sheet for this particular charge pump and can also be found in Figure 5-30 below (Texas Instruments, LM27762).

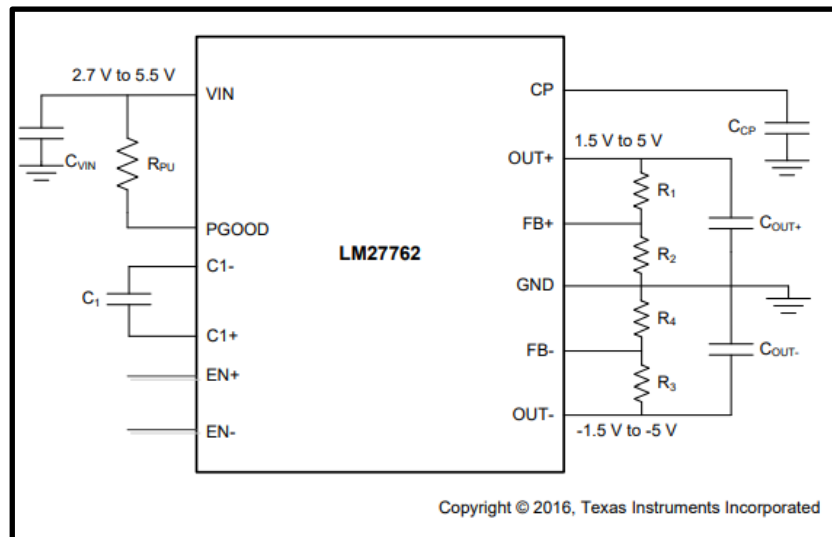


Figure 5-30: Texas Instruments LM27762 Charge Pump Typical Application Setup (Texas Instruments, LM27762)

This particular charge pump can output between ± 1.5 V to ± 5 V. For our application an output of ± 5 V is desired and the values of C_{VIN} , R_{PU} , C_1 , C_{CP} , C_{OUT+} , C_{OUT-} , R_1 , R_2 , R_3 and R_4 must be chosen. The datasheet explains that the values of $C_{VIN} = C_{OUT+} = C_{OUT-} = 2.2 \mu F$, $C_1 = 1 \mu F$ and $C_P = 4.7 \mu F$ unless specified otherwise for a particular functionality (Texas Instruments,

LM27762). Based on the datasheet and the purposes of our application these values are sufficient. The value of resistor R_{PU} is only specified when the functionality of PGOOD is desired otherwise this pin will be grounded. PGOOD is an output flag which indicates whether or not the power flowing in the circuit is sufficient. In addition, the remaining resistor values (R_1, R_2, R_3 and R_4) are chosen based on the output voltages desired.

6. ADS 1292 Study Results

6.1 Ordering and Software Installation

6.1.1 Creating a Texas Instruments Account

We initially ordered the ADS1292ECG-FE integrated circuit from Texas Instruments (TI) and got the software working correctly. The board was ordered through the Electrical and Computer Engineering (ECE) Shop at Worcester Polytechnic Institute. For ordering the board, and downloading the corresponding software, a TI account was needed. However, we were not permitted to directly do so over TI's web portal.

This problem was solved by going to the account “log in” page and clicking the “Need help logging in?” button in the bottom left. Clicking the button sends the user to a form asking for your name, email, etc.; and most importantly, a section describing the issue at hand. After describing the problems with account access, a reply email stated that TI could create an account manually. All that was needed was information including name, email, zip code, university name, role (“student”), application (“medical”), and phone number. After that, a TI account was created and the ADS1292ECG-FE integrated circuit software was downloaded.

6.1.2 Downloading Software

The software for the ADS1292ECG-FE integrated circuit is the ADS1x92xEVM-SW and the installer can be directly downloaded from the TI website under the “Order & Start Development” section on the ADS1292ECG-FE page. Once the installer file was downloaded, it was run to complete the installation of the ADS1x9xEVM-SW. Instructions for proper installation were found in the user guide for the ADS1292ECG-FE under the “Technical Documentation” section. Section 3.2 in the user guide describes to the reader the different options needed to be selected to successfully install the software, with pictures of the popups to make it easier to follow along. The user guide also contains a list of required setups needed for the software, including a Microsoft Windows XP SP2 or Windows 7 operating system and a USB to mini-USB connector to connect the board to the computer.

After the software is finished installing, the USB drivers need to be installed. In section 3.3 of the user guide, it walks through the process of installing the USB drivers similar to that of the software. For versions of Windows more recent than Windows 7, some problems may occur with the installation of the USB drivers, as discussed in the next section.

6.2 Problems with Installation

6.2.1 USB Driver Not Properly Installed

For versions of Windows more recent than Windows 7, a popup may not open asking for the installation of the USB driver when connecting the board to the computer. In our case Windows 11 was being used and this problem did occur. USB drivers are supposed to be automatically installed for updated versions of Windows which is why the popup does not show up. But since the software and USB drivers are very outdated, it did not correctly install on its own.

When running the software, a message at the top of the graphical user interface (GUI) may state “Trying to establish connection with ECG Recorder” and after a few seconds a popup will read “ECG Recorder not detected”. If so, the software is not detecting the board. If the board is connected, then the problem is with the USB drivers. Another way to verify that it is indeed the USB drivers that are causing the problem is to go to the device manager on the computer being used and check under the “ports” section. If the name of the USB driver is listed as something similar to “USB Serial Device (COM3)” and not “ADS1x9x - ECG Recorder (COM3)”, then there was a problem with the installation of the USB drivers.

6.2.2 How USB Driver Problems Were Fixed

The following steps were done to solve the USB Driver installation problems:

1. Disable the Unified Extensible Firmware Interface (UEFI) Secure Boot
2. Disable Digital Signature Checking
3. Update the USB Driver

Before beginning with step one to disable the UEFI Secure Boot, find the bitlocker recovery key, which may be needed when attempting to disable the secure boot. Unless the key is already known, it can be found on the Microsoft account website.

The secure boot setting can be found in the BIOS settings, which is opened by holding the “shift key” and clicking “restart” on the computer. Once the computer restarts, instead of displaying the usual home screen, it will display the BIOS settings. On the BIOS settings display “troubleshoot” was selected, then “advanced options”, and finally the secure boot setting was found in the BIOS menu. It is usually in the security, boot, or authentication tab. The secure boot was disabled, and the changes were saved, which reboots the computer.

Step two involves disabling digital signature checking, which can be done in the command prompt. The command prompt needs to be opened as an administrator, which is done by right clicking the command prompt setting and selecting “run as administrator”. If the computer asks, allow changes to be made on the computer. In the command prompt type in “bcdedit /set loadoptions DISABLE_INTEGRITY_CHECKS” and press enter. Next, type in “bcdedit /set testsigning on” and press enter. This disables digital signature checking.

The third step involves updating the USB driver in the device manager. Open the device manager, go to the ports section, and find the corresponding USB driver in this section. In our case it was called “USB Serial Device (COM3)”. Click the driver and select the driver tab, then click “update driver”. After that a popup will open and the following options were selected in this order:

1. “Browse my computer for drivers”
2. “Let me pick from a list of available drivers on my computer”
3. Select the USB serial device.

If the update is successful, check to see if the name of the USB driver is now “ADS1x9x - ECG Recorder (COM3)”. If so, then execute the software, make sure the board is connected, and check to see if the resulting GUI that appeared is detecting the board. The GUI will read “ready” at the top if it detects the board.

6.3 Functioning Software and Early Testing

6.3.1 GUI of ADS1x9xEVM Software

Once the software detects the board, then the software interface should be fully functional. The GUI that appears when executing the software has five main tabs labeled: about, ADC register, analysis, save, and live ECG/RESP display. The about tab just explains what the software and board does and displays its version.

The ADC register tab is where the main control of the board happens (for our purposes). There are five separate tabs within the ADC register tab labeled channel registers, LOFF and RLD, GPIO registers, respiration registers, and register map. The channel registers tab contains the ability to change the settings for the separate channels. Some of the settings that can be controlled here are the channel oversampling ratio (which controls the sampling rate), reference voltage, test signal amplitude, test signal frequency, lead-off comparator threshold/current magnitude/frequency, PGA gain, and most importantly channel input.

The LOFF and RLD tab contains the ability to control settings to enable lead-off detection and for which channels, and deriving the right leg drive signal. One of the settings that can be controlled here is the chop frequency which, when enabled, removes any internal offset voltage. The GPIO registers tab contains the ability to control the settings for general purpose inputs and outputs. The respiration registers tab contains the settings needed for respiration and the RLD reference signals can be changed here. Some of the settings that can be modified here are modulation, respiration phase/control, calibration signal, respiration control frequency, and RLD REF signal source. Finally, the register map tab is just a table that reads back the register bit values from the ADS1292ECG-FE integrated circuit.

The analysis tab is where all the data collected on the board can be seen and manipulated. There are four separate tabs within the analysis tab: scope, histogram, FFT, and ECG/RESP display tabs. The scope tab displays the data in the time-domain, plotted as either input-referred or non-input-referred voltage. For input referred, the output voltage is divided by the PGA gain setting. There is an option for scope analysis which gives the mean voltage, root mean square voltage, and peak to peak voltage. At the top of the screen there is also an option to set the

samples per channel, and a button to acquire data from the board. The data can also be plotted continuously.

The histogram tab displays the data in a histogram format. Some of the settings that can be changed on this tab are the total number of bins and various displays such as nyquist, nichols, s plane, and z plane. The FFT tab displays the data in the frequency domain by performing a fast Fourier transform (FFT) on the two channels. There is an option for FFT analysis which displays a comprehensive list of information including the signal to noise ratio. Some of the settings that can be changed on this tab are the bins, input amplitude, low and high frequency, and the desired or ideal frequency. Finally, the ECG/RESP display tab displays the ECG data for all the leads. Here is where a high pass, low pass, or notch filter can be applied. The filter order and cutoff frequency can also be modified here.

The save tab is self-explanatory, since it allows the user to save any data collected on the board. Finally, the live ECG/RESP display tab displays live ECG and respiration data for all leads. Here the signal bandwidth and notch filter can be changed, and the heart and data rate can be seen. In our case, the data will be EMG data but all the different functions that are in the ADS1292 GUI should work the same.

6.3.2 Connecting to Function Generator and Results

The function generator was connected to pins one and two of the DB9 ECG connector on the ADS1292ECG-FE board. These pins are labeled ELA and ERA for the left arm and right arm respectively. The sine wave signal was received and displayed on the GUI in the scope analysis tab. Figure 6-1 shows an example sine wave signal (100 mV_{p-p}, 150 Hz). Analysis data magnitude is not input referred and there were 1000 samples per channel. The resulting signal, using the scope analysis function, is 110 mV_{p-p}, and the sampling frequency is 2000 samples per second.

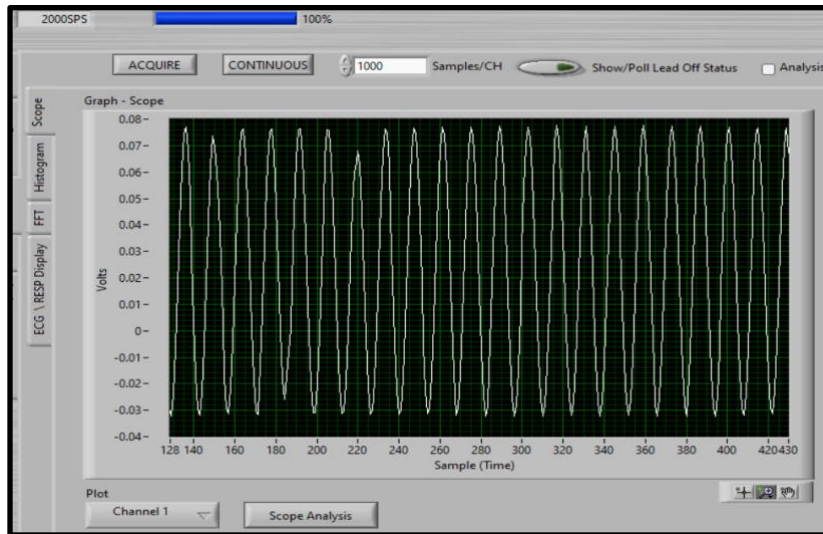


Figure 6-1: Example Sine Wave Signal from Function Generator passing through the ADS1292ECG-FE and Displayed on the software GUI

Initially, different signals were tested, such as square and triangle waves, and both were correctly displayed. The next step was to test the different settings to see how they affected the data. The amplitude, gain, and frequency were changed and all changes showed up on the display. Figure 6-2 shows the same sine wave being input to the ADS1292ECG-FE with the PGA now set to 12. Both the sampling frequency and the frequency of the input sine wave were kept the same, so 2000 samples per second and 150 Hz respectively. The expected peak-to-peak voltage should be around 1.2 V and using the scope analysis function the peak-to-peak voltage was found to be 1.41 V pk-pk.

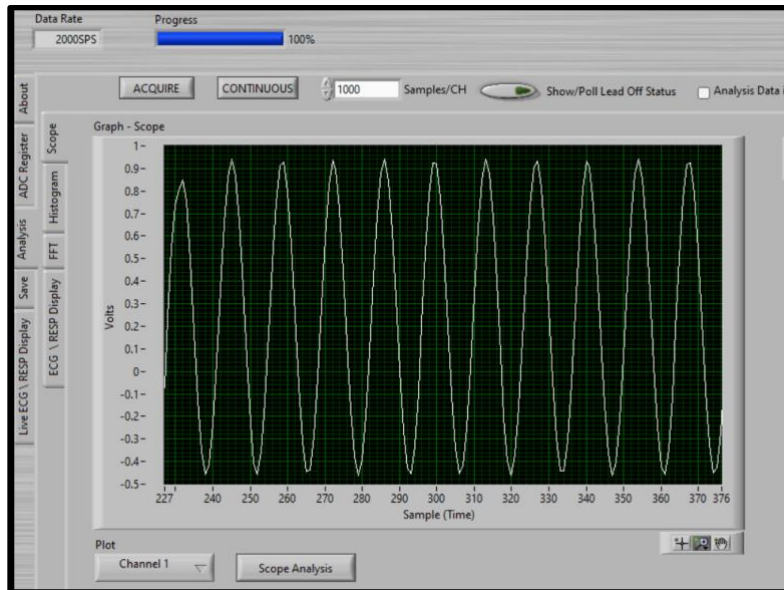


Figure 6-2: Example Sine Wave Signal from Function Generator passing through the ADS1292ECG-FE and Displayed on the software GUI with a Gain of 12

6.4 EMG Application

6.4.1 Instrumentation Amplifier

6.4.1.1 Overview

The programmable gain amplifier on the ADS1292ECG-FE has a maximum gain of 12. To meet our minimum gain requirement of 360, which amplifies an average 10 mVp-p signal to 3.6 Vp-p, an additional gain stage must be added to the front end of the board. The AD8422 was used to keep design option 3 as similar as possible to design option 1 so that a fair comparison of using the ADS1292ECG-FE versus not using it could be made. The same batteries used to power the front end design option 1 were also used in design option 3 for the same reason. The schematics that used the AD8422, how it was designed on a breadboard, and testing can be seen in Chapter 5.

For use with the ADS1292ECG-FE, the gain needed to be 30 so that combined with a gain of 12 from the PGA on the ADS1292ECG-FE, the total gain would meet our requirement of 360. Using equation 5-1 from Chapter 5, the resistance across pins 2 and 3 of the AD8422 needed to be about 682 Ω to give a gain of 30. So a resistance of 680 Ω was used.

Connecting the AD8422 to the ADS1292ECG-FE was simple. The output on the amplifier, pin 7, was connected to pin 1 of the DB9 ECG connector on the ADS1292ECG-FE. The negative rail from the breadboard was connected to pin 2 of the DB9 ECG connector.

6.4.1.2 Advantages and Disadvantages of Increasing Gain

The advantage of increasing gain is that as the gain on the amplifier increases, the lower the generated noise level. Lower noise makes analyzing the signal easier and any calculations more accurate.

The disadvantage of increasing gain on the instrumentation amplifier includes the possibility of distortion of the signal. If the gain is increased too high, it could cause clipping, which is a form of distortion that makes analyzing signals harder. An additional problem with increasing gain is it can lead to creating heat on the electronics if the power of the signal is too high. Although this is likely not an issue for the signals involved in our EMG application being that they have a small peak-to-peak voltage.

6.4.1.3 Voltage Noise Testing

One of the main tests that can be done to compare design option 3 to design option 1 is a voltage noise analysis. Two different tests were done, one without the instrumentation amplifier, and one with the instrumentation amplifier attached to the ADS1292ECG-FE.

For test number one, two wires were connected to pins 1 and 2 of the DB9 connector, which are the inputs to the ADS1292, and shorted together. These pins are labeled ELA and ERA for the left arm and right arm respectively. The data were then acquired, with a sampling rate of 2000 samples per second, a duration of half of a second, and a gain of 12, through the ADS1292 software and the scope analysis function was used to find the RMS voltage. The RMS voltage of the data after subtracting out the mean was 53 μV which then divided by 12 gives the input-referred noise of 4.4167 μV . In Figure 6-3, the output of the noise test can be seen.

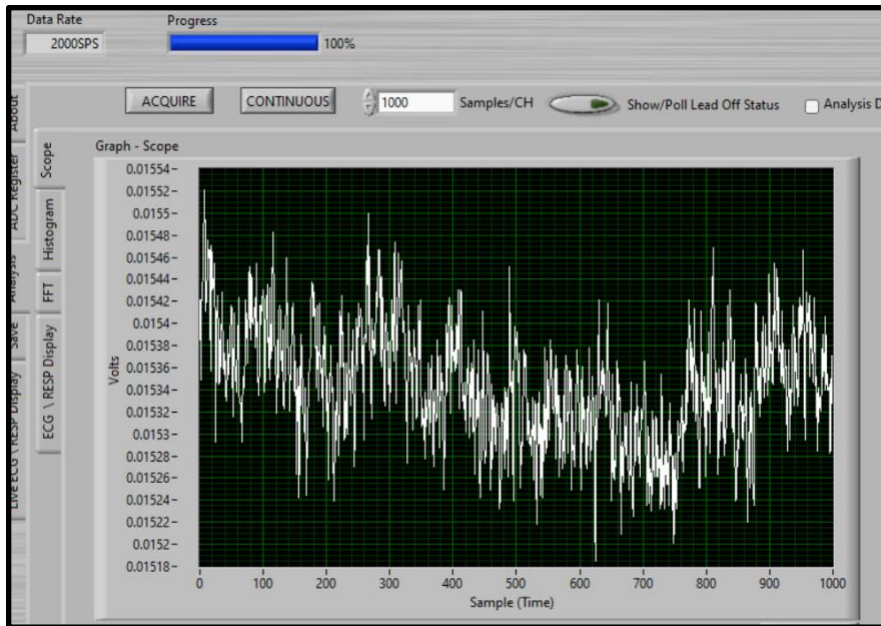


Figure 6-3: Output after Inputs were Shorted Together on ADS1292ECG-FE with a Sampling Rate of 2000 Samples per Second

For test number two, the instrumentation amplifier, with a gain of 30, was connected prior to the ADS1292ECG-FE. The two inputs of the amplifier were shorted together and the resulting data were then acquired, with an additional gain of 12, through the ADS1292 software. The scope analysis function was used to find the RMS voltage which was then divided by the total gain of 360. The RMS voltage of the data after subtracting out the mean was found to be $640 \mu\text{V}$ which then divided by 360 gives $1.7778 \mu\text{V}$ of noise. Figure 6-4 shows the output of the second noise test.

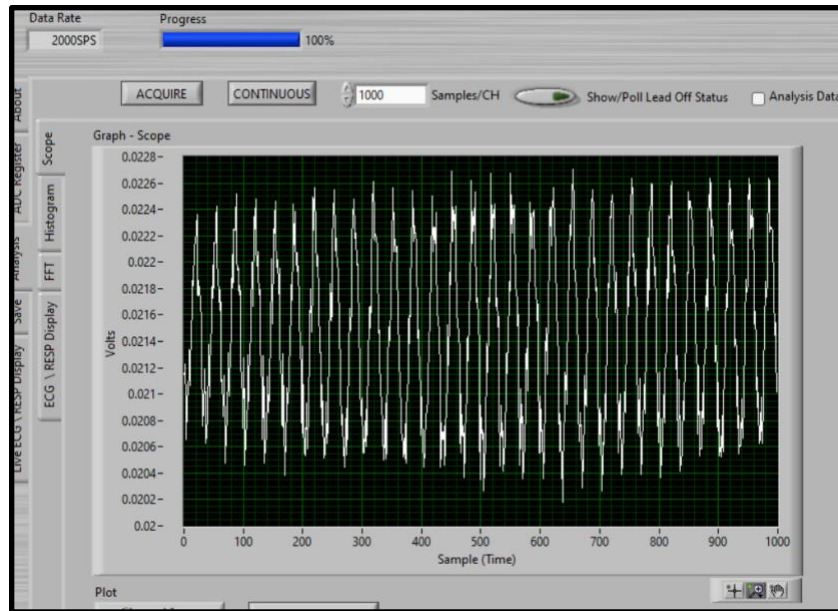


Figure 6-4: Output after Inputs were Shorted Together on Instrumentation Amplifier connected to the ADS1292ECG-FE with a Sampling Rate of 2000 Samples per Second

6.4.2 Voltage Divider

Using the function generator (Tektronix CFG253) and oscilloscope (Tektronix TDS 210) available to us, it was hard to test signals at voltages that would be seen through an EMG. That voltage is at its maximum around 10 mVp-p. The testing done in the design option 1 was done with 50 mVp-p and a frequency of 150 Hz using the function generator. For design option 3, a voltage divider was added to the front of the instrumentation amplifier to get a signal of 10 mVp-p. The circuit of a basic voltage divider can be seen in Figure 6-5.

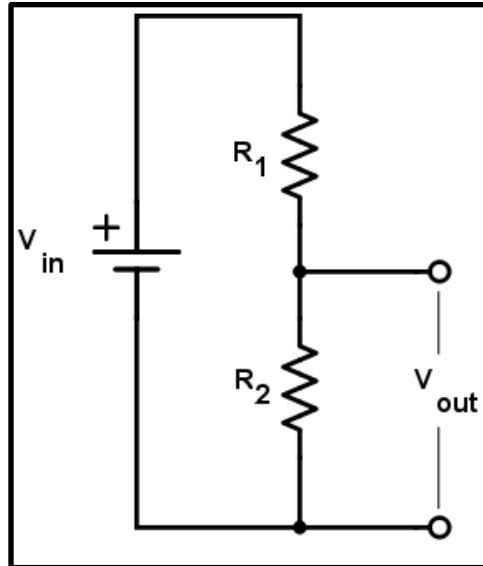


Figure 6-5: Schematic of a Voltage Divider

Image link: <https://www.allaboutcircuits.com/uploads/thumbnails/voltage-divider-main-circuit.png>

For the EMG application, V_{out} needs to be a 10 mVp-p sine wave and using a 50 mVp-p sine wave as V_{in} means that values for R_1 and R_2 need to be selected to fit these requirements. The equation for the voltage divider can be seen in equation 6-1.

$$V_{out} = V_{in} * \frac{R_2}{R_2 + R_1} \quad (\text{Eq. 6-1})$$

R_2 was selected as a 56 Ω resistor and R_1 was selected as a 220 Ω resistor to achieve the correct V_{out} value. Although the resistance values are small which will lead to larger currents, for design option 3 we are working with a signal generator which is connected to the wall electrical outlet. The output voltage is then connected to pins 2 and 3 of the instrumentation amplifier. A picture of the voltage divider, instrumentation amplifier, and the ADS1292ECG-FE all connected together on a breadboard can be seen in Figure 6-6.

R_2 was selected as a 56 Ω resistor and R_1 was selected as a 220 Ω resistor to achieve the correct V_{out} value. Although the resistance values are small which will lead to larger currents, for design option 3 we are working with a signal generator which is connected to the wall electrical outlet. The output voltage is then connected to pins 2 and 3 of the instrumentation amplifier. A

picture of the voltage divider, instrumentation amplifier, and the ADS1292ECG-FE all connected together on a breadboard can be seen in Figure 6-6.

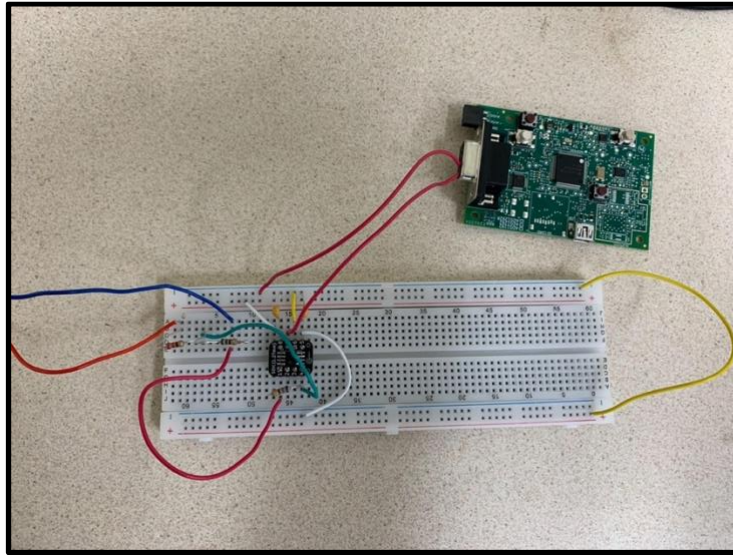


Figure 6-6: Circuit with Voltage Divider, Instrumentation Amplifier, and ADS1292ECG-FE

R_2 was selected as a 56Ω resistor and R_1 was selected as a 220Ω resistor to achieve the correct V_{out} value. Although the resistance values are small which will lead to larger currents, for design option 3 we are working with a signal generator which is connected to the wall electrical outlet. The output voltage is then connected to pins 2 and 3 of the instrumentation amplifier. A picture of the voltage divider, instrumentation amplifier, and the ADS1292ECG-FE all connected together on a breadboard can be seen in Figure 6-6.

Using a function generator and dual power supply, a 150 Hz sine wave with 50 mV_{p-p} was passed into the circuit and then acquired with a sampling rate of 2000 samples per second. The voltage divider brings the peak-to-peak voltage down to 10 mV and then the amplifier with a gain of 30 brings it up to 300 mV_{p-p} . A gain of 12 was selected on the ADS1292ECG-FE, so after the signal passed from the amplifier the peak-to-peak voltage was brought up to about 3.6 V. An image of the resulting sine wave on the ADS1292ECG-FE software can be seen in Figure 6-7 where the peak-to-peak voltage was measured to be 3.72 V.

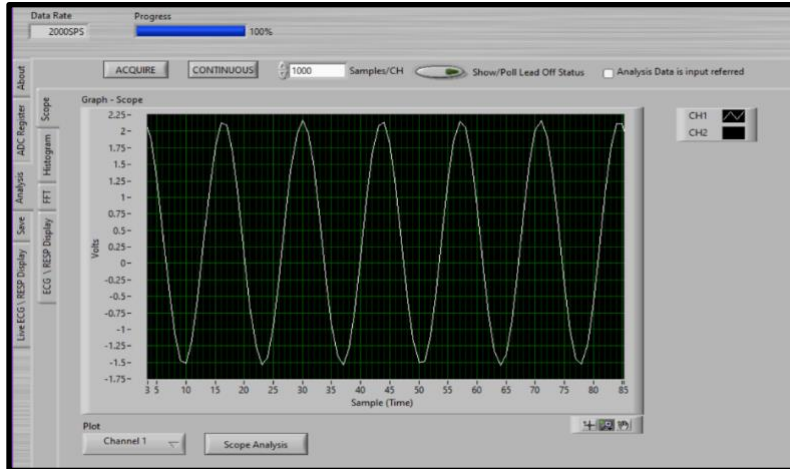


Figure 6-7: Sine wave at 150 Hz and 3.72 V_{p-p} Result on ADS1292ECG-FE Software After Passing Through the Circuit with a Sampling Rate of 2000 Samples per Second

6.4.3 Effective Number of Bits (ENOB)

6.4.3.1 Definition

The effective number of bits of an ADC is the resolution in the number of bits of that ADC when introducing noise and distortion into the system. ENOB is quantifying how many bits are effective so in other words how accurate the ADC is at converting between analog and digital information. Noise and distortion can come from anything such as quantization noise, or noise from the input signal (Girard, 1995). The measurement called signal to noise and distortion ratio (SINAD) is used to calculate the noise and distortion needed to figure out ENOB. SINAD is the ratio of the “fundamental frequency signal power level to the noise plus distortion power level” (Maxim Integrated, 2019). In section 6.4.3.2 below, the calculations for the above measurements are listed.

6.4.3.2 Calculations

The equation for solving for ENOB can be seen in equation 6-2 where SINAD is given in dB (Girard, 1995). In equation 6-2, everything to the right of the plus symbol on the numerator is not needed if the collected sine wave fills the voltage range. If not, this extra term is needed.

$$ENOB = \frac{SINAD - 1.76 + (20 \cdot \log_{10}(\frac{\text{Full Scale Voltage of ADC}}{\text{Peak to Peak Voltage of Collected Sine Wave}}))}{6.02} \quad (\text{Eq. 6-2})$$

SINAD is more complicated to solve for so there are two different data analysis methods used, one being a time domain data analysis, and the other being a frequency domain data analysis (Girard, 1995). The time domain data analysis method that initially, removes the mean value from the data. Then, an algorithm matches a perfect sine wave to the received data. The sine wave is subtracted from the data and what remains is used to calculate SINAD (Girard, 1995). The equation can be seen in equation 6-3 where A_{rms} is the best fit sine wave amplitude in RMS voltage, and NAD is RMS noise and distortion after subtracting the sine wave first (IEEE, 2011).

$$SINAD = \frac{A_{rms}}{NAD} \quad (\text{Eq. 6-3})$$

A_{rms} is calculated using the sine wave peak amplitude, and NAD is calculated using the number of points in the data, the collected sine wave, and the fitted sine wave. The equations for A_{rms} and NAD can be seen in equations 6-4 and 6-5 respectively (IEEE, 2011).

$$A_{rms} = \frac{\text{Collected Sine Wave Peak Amplitude}}{\sqrt{2}} \quad (\text{Eq. 6-4})$$

$$NAD = \sqrt{\frac{1}{M} * \sum_{n=1}^M (x[n] - x^{\sim}[n])^2}, \quad (\text{Eq. 6-5})$$

where M is the number of points in the collected sine wave, $x[n]$ is the data from the collected sine wave after subtracting the mean value, and $x^{\sim}[n]$ is the data from the fitted sine wave.

The frequency domain data analysis method uses the Discrete Fourier Transform (DFT) to convert the time domain data to frequency domain data (Girard, 1995). An analysis done on the resulting DFT results in SINAD and the equation can be seen in equation 6-6 (Maxim Integrated, 2019). The magnitude squared of the DFT should be taken before doing the calculation in equations 6-6.

$$SINAD = 10 \log\left(\frac{P_S}{P_{N+D}}\right), \quad (\text{Eq. 6-6})$$

where P_S is the fundamental frequency signal power and P_{N+D} is the noise plus distortion power level (Maxim Integrated, 2019). P_S can be found by looking at the power of the fundamental frequency which is the large spike centered around the frequency of the collected sine wave on the DFT plot. P_{N+D} is the average power of the noise floor which is what is left in the DFT plot

when you ignore the fundamental frequency and all other harmonics plus the power of the remaining harmonics.

6.4.3.3 Results

For our application we tried calculating ENOB using both the time domain and frequency domain analysis methods. For both applications we collected the largest possible sine wave without clipping at 150 Hz. The sampling frequency was set to 2000 samples per second, the reference voltage was at 4 V, the gain was set to 1, and the channel input for channel 2 was set to zero to ignore any noise that may come from the second channel. Also, there were 1000 samples per channel and the analysis data were not input referred. The scope analysis, FFT analysis, and data were saved from channel one from the ADS1292ECG-FE software so that we could do further analysis in MATLAB.

There was one problem, when saving the data from the software, with the Microsoft excel spreadsheets being corrupted. The data were copied over to a new Microsoft excel spreadsheet that was not corrupted. The data were imported into MATLAB using the import data function.

The largest possible sine wave without clipping used for both methods was a sine wave at 150 Hz frequency and a peak-to-peak voltage of about 6 V. In this case the peak-to-peak voltage of the sine wave was 6.036 V. The signal can be seen in Figure 6-8 where it was plotted in MATLAB.

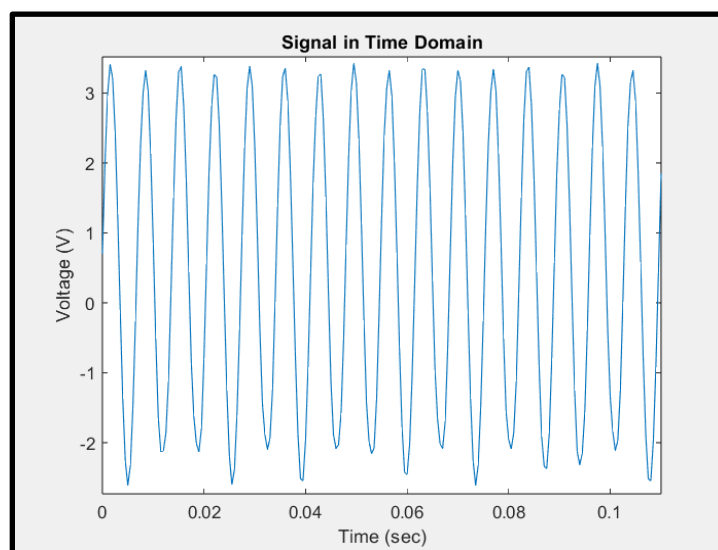


Figure 6-8: Largest Possible Sine Wave Collected without Clipping (150 Hz, 6.036 V_{p-p})

First, we tried the frequency domain method with the largest possible signal without clipping but without much success. We took the DFT of the signal subtracted by its mean to remove the DC term (0 Hz term). We then took the absolute value of only the first half of the DFT. In Figure 6-9 the DFT of the signal plotted in MATLAB can be seen. The problem we ran into can easily be viewed in the DFT plot. The fundamental frequency was not a single peak, it slowly ramped up and down so it had a width to it. When trying to calculate the power of the fundamental frequency and of the noise floor, only the maximum value of the peak was counted as the power of the fundamental frequency and the rest of the peak was counted as noise even though it should not.

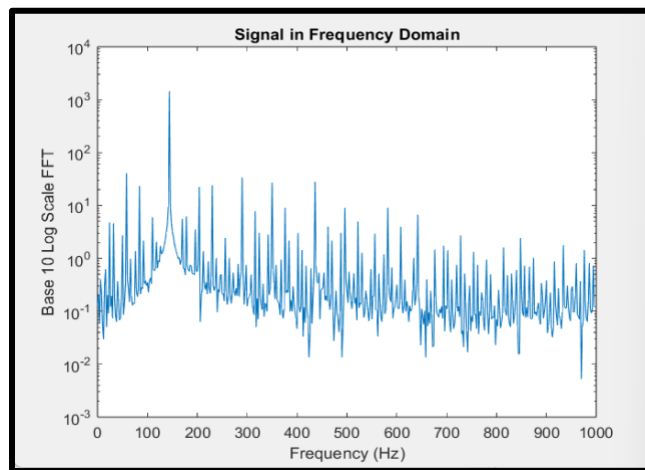


Figure 6-9: Largest Possible Sine Wave Collected without Clipping in Frequency Domain

Since we ran into problems using the frequency domain analysis, we reverted to the time domain analysis. Overall, we had to predict the fitted sine wave parameters, fit a new sine wave to the collected sine wave (first the largest possible sine wave without clipping), find SINAD, and then finally find ENOB. First, we estimated the amplitude of the fitted sine wave by taking the rms value of the signal minus its mean and then multiplying it by the square root of two. We estimated the frequency of the fitted sine wave by using the mode value in the DFT. We did this by finding the index value of the fundamental frequency in MATLAB (from its DFT magnitude), subtracting it by one (to adjust for MATLAB indexing), multiplying it by the sampling rate, and then dividing it by the total number of points in the data. We trimmed the data set to achieve an initial phase of zero degrees as a guess for the phase. We then estimated the best fit amplitude, frequency, and phase of the sine wave by using the “lsqnonlin” function in MATLAB which is a

nonlinear least square data fitting function. The fitted sine wave on top of the collected sine wave can be seen plotted in MATLAB in Figure 6-10. The fitted sine wave is almost completely covering the collected sine wave and the error which is not much can be seen in Figure 6-11.

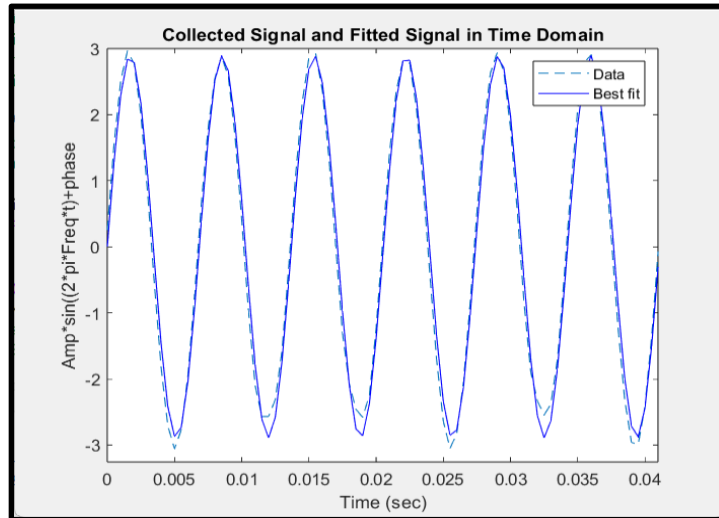


Figure 6-10: Largest Signal without Clipping and Fitted Signal in the Time Domain

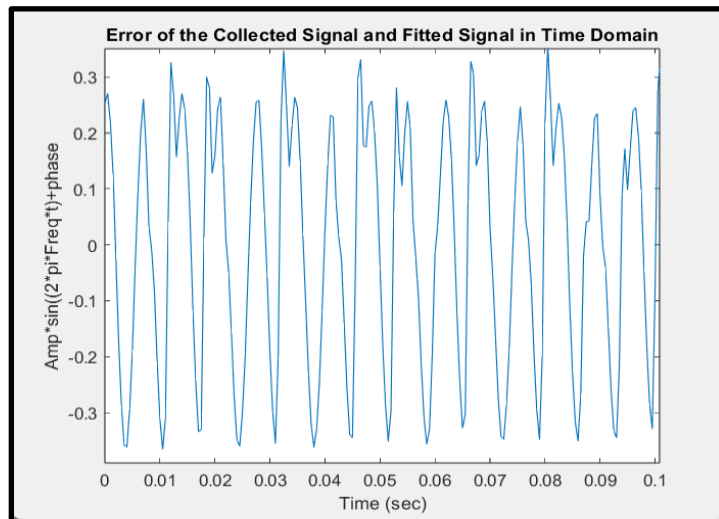


Figure 6-11: Error of the Fitted Signal in the Time Domain

Next, equations 6-2, 6-3, 6-4, and 6-5 were used to calculate ENOB which was found to be 17.9668 bits. The MATLAB code used to do all of the calculations above can be seen in Appendix C.

6.4.4 Power Spectral Density (PSD)

6.4.4.1 Definition and Calculation

Power spectral density (PSD) is the variations in power versus frequency of a given signal. PSD displays at which frequencies the signal is strong and at which the signal is weak by showing how much power is composed in the frequency band of a signal. PSD is not only useful for analyzing a signal at different frequencies, but it also is used to calculate total power of a signal and can be used to check if the inputted signal is too large and clipping which for our ENOB calculation is very useful. The total power is found from the PSD by taking the integral over the entire frequency band of the signal. PSD overall is useful in understanding the characteristics of a signal to better analyze it.

For calculating PSD the “pwelch” function in MATLAB is a great tool to do so. It creates an array that shows the variations in power versus frequency. This array can then be graphed to view the PSD. In our case the signal data can be saved from the ADS1292ECG-FE software directly as a Microsoft Excel spreadsheet and then imported into MATLAB. After that, the “pwelch” function is used to calculate the PSD and is then plotted so it can be viewed. The total power of the signal can be computed by using the “dspdata.psd” and “avgpower” functions which take the integral of the PSD and calculate the total power.

6.4.4.2 Results

We found the PSD and total power of the collected sine wave used in section 6.4.3, using the largest sine wave possible without clipping at 150 Hz and 6.036 V_{p-p}. All the calculations were done in MATLAB and the code can be seen in Figure 6-12.

```
50 PSD = pwelch(a); %Finding the PSD
51 figure(5)
52 pwelch(a) %Graphing the PSD
53 Hs = dspdata.psd(PSD); %Taking data from PSD
54 Power = avgpower(Hs); %Finding Total Power
```

Figure 6-12: MATLAB Code Used to Find PSD and Total Power

The PSD of the largest sine wave possible without clipping can be seen in Figure 6-13. We can check to see if the PSD is being calculated correctly by checking the normalized frequency of the largest peak. If we take this value and insert it into equation 6-9 we should get back the frequency of the collected sine wave. In our case the normalized frequency was 0.148438 and we get back a frequency of about 148 Hz (0.148438×1000) which is about the frequency of the collected signal at 150 Hz. In Figure 6-13, there are no significant harmonics other than the fundamental, which tells us that the input signal was not too large and clipping. Therefore the inputted signal is at the full range of the ADS1292ECG-FE and our ENOB calculation is more accurate.

$$\text{Frequency} = \text{Normalized Frequency} * \frac{\text{Sampling Rate}}{2} \quad (\text{Eq. 6-9})$$

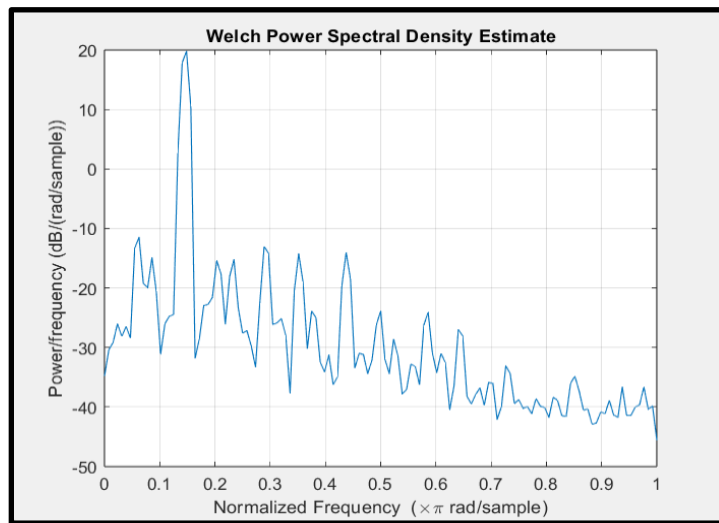


Figure 6-13: PSD of Largest Possible Sine Wave without Clipping

The total power was calculated using the “dspdata.psd” and “avgpower” MATLAB functions and was found to be 4.1848 dB.

6.5 ADS1292 Discussion

6.5.1 Limitations

The limitations of this design option all revolve around the ADS1292ECG-FE. The three main limitations are involved with the software, gain control, and number of channels. The

limitation of the software is that it is very outdated which creates problems when installing and when running. The problems with installation have been described in section 6.2 and the problems with running the software involve it crashing from time to time and failure to download non-corrupt Microsoft Excel files. All of these problems add time to getting the software downloaded, working, and data saved for further analysis. With the software being old, there also is not a clear explanation of how the analysis is done for some of the specifications, for example ENOB and SINAD, so it is hard to independently verify the results. This created problems with trying to calculate ENOB in particular since we had to learn how to calculate it from scratch. Some of the specifications are not clearly defined; for example, the scope analysis function lists the RMS voltage of the imputed signal, but it does not display that it is the RMS value of the data minus its mean. This can create problems with analyzing data directly off of what the software displays. Again, all of these problems add time to the whole process which may not be worth it for some applications.

The limitations with gain control and number of channels is more connected to our EMG application. The minimum gain needed to be 360 for our application, so an additional gain stage was added prior to the ADS1292ECG-FE since the selectable gain only goes up to 12. That is just the minimum gain so to reach our whole spectrum of gain selection, we would have needed more gain stages. The other limitation of the ADS1292ECG-FE for our application is that there are only two input channels. In our main design option there are 5 channels, so this would not work for the ADS1292ECG-FE.

6.5.2 What Could Have Been Done Better

The main area of improvement if we had more time, is in the effective number of bits calculation. As discussed in Chapter 6.4.3 we had problems with one of the two methods of calculating ENOB, that being the frequency domain analysis method. We had trouble determining detailed methods because of the equipment used. That is why there is not a single peak but more of a ramp up and down in Figure 6-9. If we had more time, we would have studied more about the frequency domain analysis method to hopefully recreate these tests for the ADS1292ECG-FE. We would have also found better oscilloscopes and function generators than the ones used in the lab that created less noise, to make our calculations, not just ENOB, more accurate.

The other area of improvement is in the MATLAB script used to calculate ENOB with the time domain analysis method. As we have it, we are manually coercing an initial sine wave phase to approximately 0° . We would like to automate calculation of the phase using correlation but we ran out of time.

6.5.3 Comparison to 24-bit ADC

For deciding whether a 24-bit ADC would be better over the ADS1292ECG-FE integrated circuit we need to weigh the advantages and disadvantages of both. The advantages of the ADS1292ECG-FE are that it is an all built into one microcontroller, not expensive, does its own analysis, works for the range of voltages in our application, and is somewhat low noise. The ADS1292ECG-FE has two programmable gain amplifiers, two ADCs, internal reference, and an oscillator. The software that goes along with the board lets the user pick reference voltage, sampling frequency, and has its own oscilloscope to view the input signal. There is no need for much to be added on to the ADS1292ECG-FE while for just the regular 24-bit ADC there would need to be multiple stages added on to it like in the first design option. Having fewer stages makes the ADS1292ECG-FE a smaller option than the 24-bit ADC and its multiple stages added on.

The price of a 24-bit ADC like the ADS1292 is significantly cheaper at a price of 6 USD than the ADS1292ECG-FE at 99 USD which is not expensive and an advantage. However, an option is to not even use the development kit so this cost would not come into play. The software for the ADS1292ECG-FE has functions that perform different types of analysis like finding the ENOB, RMS voltage, taking the FFT, etc. None of this would be available if just using the 24-bit ADC and even if the user wants to do all of the analysis themselves, it is a good way to check if it is right. The built in oscilloscope is also a huge advantage because you do not need to find a lab that has one or write a program that displays the signals. For our EMG application we will typically see signals with $3.6 V_{p-p}$ which fits in the range of voltages without clipping on the ADS1292ECG-FE software. The last advantage is that when adding the instrumentation amplifier to the ADS1292ECG-FE for our application, the noise level is lower than the noise measured in design option 1.

The disadvantages of the ADS1292ECG-FE are that the software is outdated, there are limitations in number of channels and gain, and it is not wireless. As discussed in previous

sections, the software for the ADS1292ECG-FE is old which creates problems when installing and while running. If we were to use a 24-bit ADC we would not run into these problems. These issues are fixable but can take time and the software crashing every once in a while, can create even more problems with data collection. The cost of using the ADS1292ECG-FE over the 24-bit ADC in this case is time and possible loss of data. The other problem with the software being outdated, is that it does not explain how it calculates some of the data analysis, which can make it hard to replicate. Although if we were to use a 24-bit ADC we would have to replicate the analysis ourselves regardless.

The ADS1292ECG-FE only has two channels which for our application is a disadvantage since we require 5 channels. We would need three ADS1292ECG-FE integrated circuits for enough channels which takes up a lot of space and starts to get expensive. If we used just the 24-bit ADC this problem would not exist. The ADS1292ECG-FE only has selectable gain up to 12, but according to our ENOB calculation the effective number of bits is 18 bits. We only used 16 bits when compared to our design option one, so the last two bits can be used to get an additional gain stage of 4 (2^2) which makes the overall gain of the board 48 ($12*4$). This gain still does not meet our minimum gain of 360 so we would still need an additional gain stage with the board. The last disadvantage is that the ADS1292ECG-FE is not wireless so although it may take up less space than in design option one, the wire space needed will require more space.

6.5.4 Additional Noise Testing

The area where the effective number of bits calculation could be improved is the function generator used to simulate the signals. The function generator used was suspected to create enough noise to throw off the effective number of bits. The increase in noise increases the noise floor which in turn lowers the effective number of bits. The next step is to therefore try and find the true noise floor of the system. The ADC inputs were grounded and the resulting data were imported into MATLAB to do some additional noise calculation. A sampling rate of 2000 samples per second was used for each case and the duration was half of a second. The mean of the data was subtracted out and the FFT was plotted to find the true noise floor. The RMS voltage was also found to make sure the gain selection was working correctly. The test was done

three times with a gain of 1, 6, and 12 to see how greatly the noise floor changes with gain. The RMS voltage with a gain of 1 was found to be $3 \cdot 10^{-4}$ V, with a gain of 6 to be $18 \cdot 10^{-4}$ V = $3 \cdot 10^{-4} \cdot 6$, and with a gain of 12 to be $37 \cdot 10^{-4}$ V which is about $3 \cdot 10^{-4} \cdot 12$. All three selectable gain values were working correctly for this noise test. The FFT plot for each test respectively can be seen in Figures 6-14, 6-15, and 6-16.

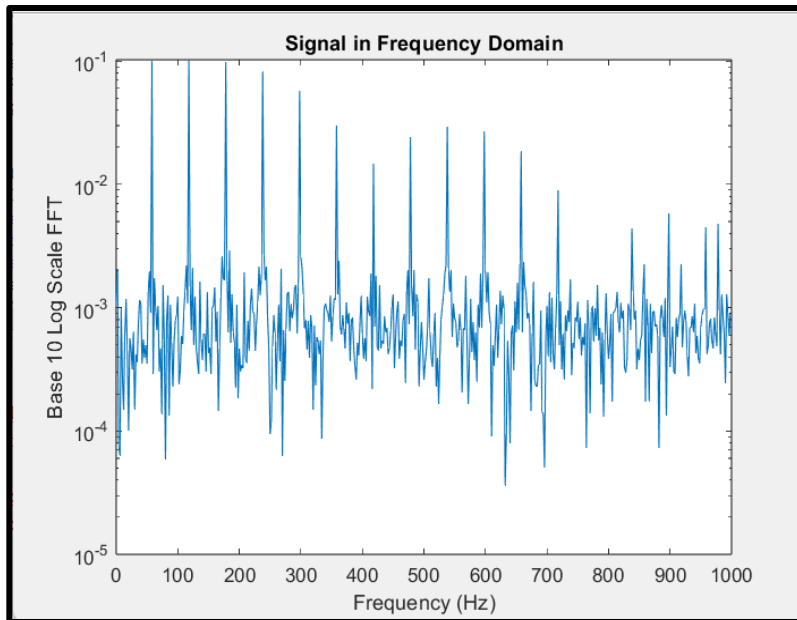


Figure 6-14: FFT Plot for Grounded Inputs of System with Gain of 1

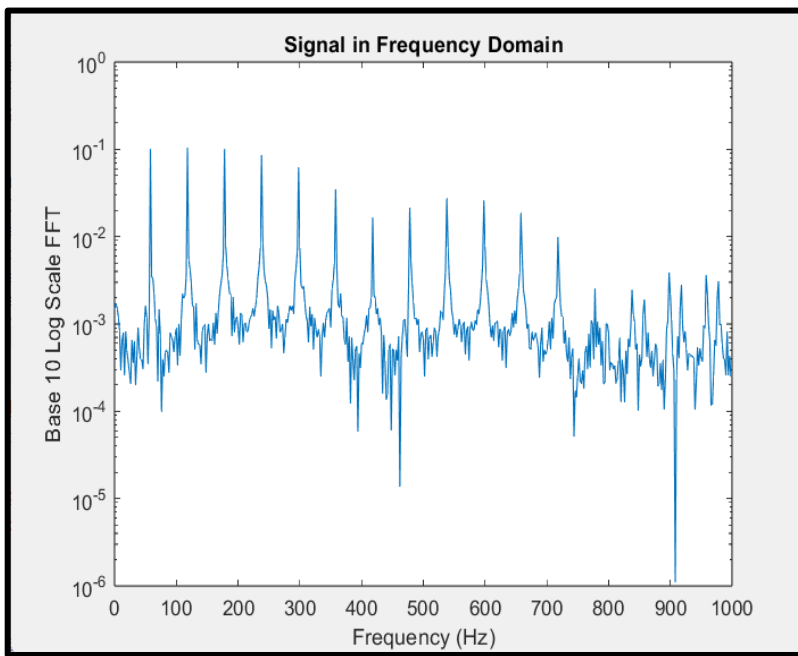


Figure 6-15: FFT Plot for Grounded Inputs of System with Gain of 6.

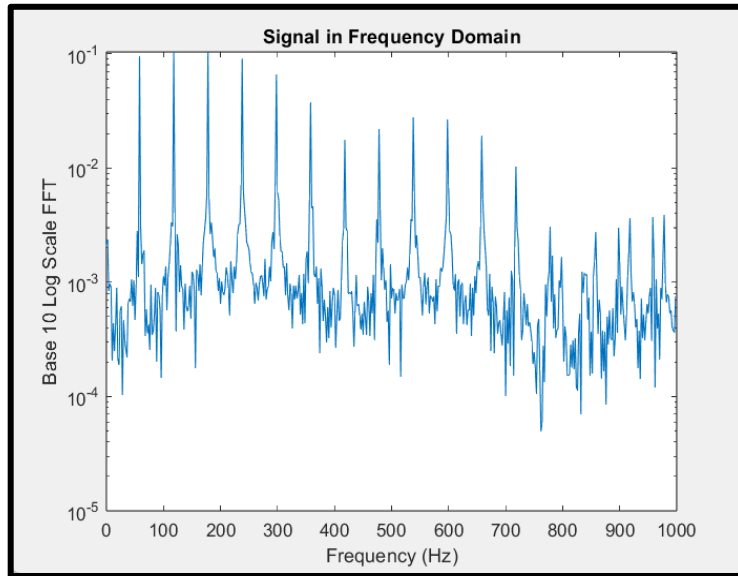


Figure 6-16: FFT Plot for Grounded Inputs of System with Gain of 12

In all three cases the noise floor is about the same which shows that no matter what gain is chosen on the programmable gain selection the noise does not change. The non-change in noise is great for our application because we are utilizing multiple gain selections. However, the noise floor found in all three cases above is significantly lower, about 100 times less, than in Figure 6-9 where the FFT is plotted using a function generator. If a function generator that produced less noise was used the real noise floor would be close to the value found in the above three examples. That means the effective number of bits calculation was not entirely accurate. The real noise floor is much lower, so the real effective number of bits is higher. If the true effective number of bits is closer to 20 bits and assuming the effective number of bits for the 16-bit ADC used in design option 1 is about 15 bits, that gives 5 extra bits that can be used for gain control. The 5 extra bits produces an additional gain stage of $2^5 = 32$ and when multiplied by the maximum gain selection of the ADS1292ECG-FE of 12 the total gain is 384. The new total gain of 384 meets our minimum gain requirement which means that no additional gain stage would be required assuming that our assumptions are accurate. This would make the ADS1292ECG-FE a very viable option since all of the additional analog components used in design option 1 are not needed making the product much smaller. However, these new calculations are based on some assumptions so more accurate equipment is required to confirm.

7. Microcontroller Results

7.1 Software overview

7.1.1 Microcontroller applications

The microcontroller code is relatively straightforward; the peripheral application runs an infinite loop which is interrupted for each ADC sample and every bluetooth packet received. In the former case, the data is copied into a buffer to be transmitted over bluetooth later. In the latter case, the first-in 40 bytes of the data buffer are sent over bluetooth to the central microcontroller.

Specifically, every time the ADC timer event is raised, a function is called to take the samples. This function enters a loop through each enabled ADC channel as specified in an array in the Zephyr overlay file. Each channel is initialized and read from, and the data are written into a static buffer. Once this buffer is 40 bytes long, it is copied to the FIFO buffer which the bluetooth transmission reads from.

The central microcontroller searches for and connects to the peripheral microcontroller over bluetooth, and then waits indefinitely for a packet to be sent over. Once the data are received by the central microcontroller, the data are formatted into a 54-byte packet, with a 12 byte header (consisting of 4 sync bytes, 4 bytes for the packet length, and 4 bytes for the channel ID) and 2 bytes of a checksum at the end. It outputs this packet over UART using the nRF52840-dk's micro-USB port, where a cable connecting it to a computer can be used to process the data.

Each of these processes interfacing with the hardware are implemented using Zephyr, a kernel maintained and documented by Nordic for the purpose of MCU development. Zephyr is designed to support numerous microcontrollers; the same C code can run on multiple different boards by changing out a device configuration file (provided both boards have the necessary hardware) and Zephyr handles the low-level implementation. The boards were programmed using nRF Connect v4.2.0, building the code with CMake v3.27.5 and flashing the boards using West v1.1.0.

Much of the C code inherited by the group remained unchanged throughout the project. Primarily, edits made to these programs concerned configuring the ADC to meet our

specifications and formatting the data for off-line processing. Due to the bulk of the code being unchanged, the following sections will largely only detail the altered sections of the programs.

7.1.2 Data processing script

The data collection script on the acquisition PC uses MATLAB's serialport interface to collect the data from the computer's USB port. It reads some arbitrary number of UART packets and copies them in their entirety to an array, and their lengths (in bytes) into a separate array. Each of these arrays are then written to a CSV file for off-line analysis.

A separate MATLAB script is used to process the data and extract the ADC outputs, which iterates across each packet (separating them in the data using the packet lengths) and copies the raw data into an array while skipping over any header data. After a second pass is made to ensure no header data has been copied in, the data—which have up until now been read as unsigned 8-bit integers due to the header information—is then cast to signed 16-bit integers, saved as a CSV, and plotted using MATLAB's built-in graphing functions. Any unit conversion is also done at this step, with the ADC values scaled to the range of 0 to 3.6 V and the time between two samples fixed at the inverse of the sampling rate, which is assumed to be constant.

7.2 Initial testing

7.2.1 DC voltage input

To ensure basic functionality, the 3.3V out pin on the peripheral (Feather) board was connected to a single ADC input, and with all of the hardware running the data were collected using the aforementioned scripts. For reading 50 UART packets, 600 ADC samples taken at 2 kHz were received and graphed in Figure 7-1. This should show a roughly flat line at 3.3 V, and this result is confirmed by the output.

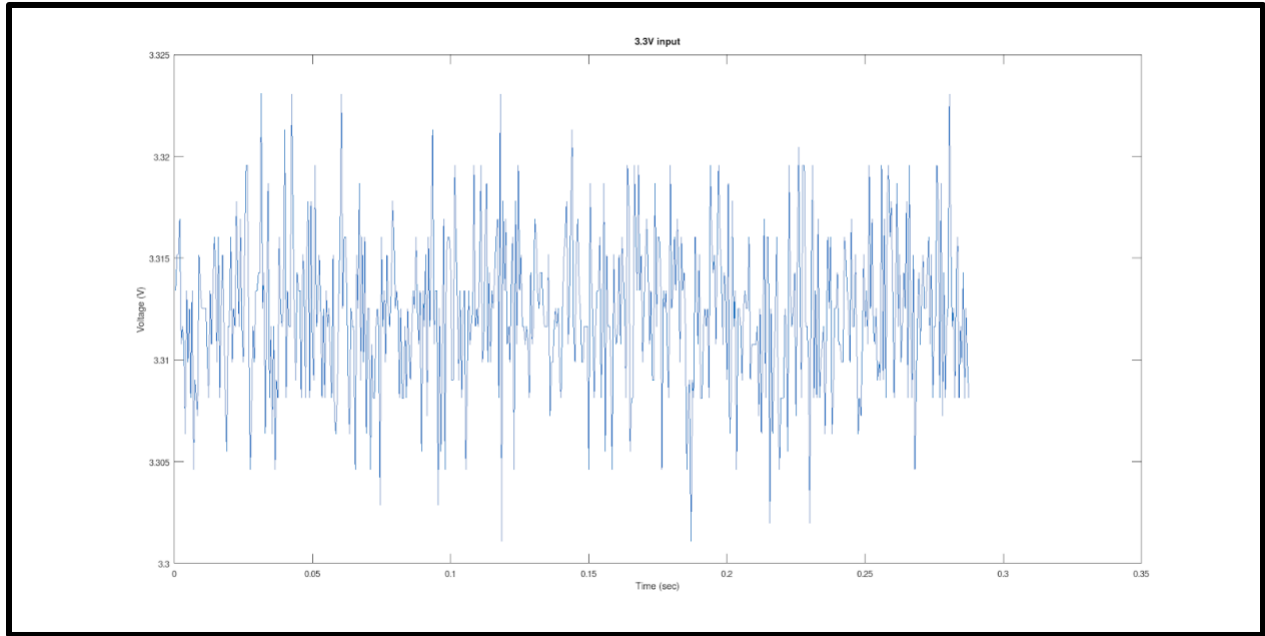


Figure 7-1: A graph of 3.3V ADC input centered around 3.3 V

7.2.2 Wave input

Next, to ensure non-constant inputs were being accurately received and stored, a function generator was connected to the ADC input. The function generator, an Instek GFG-8219A, was set to a sine wave at approximately 100 Hz, with an amplitude of 1.8V and a DC offset of 1.8V, graphed in Figure 7-2. The sine wave graphed was expected to match this description, and it roughly did, indicating that the implementation we prepared for reading out from the 2 kHz ADC was working as expected.

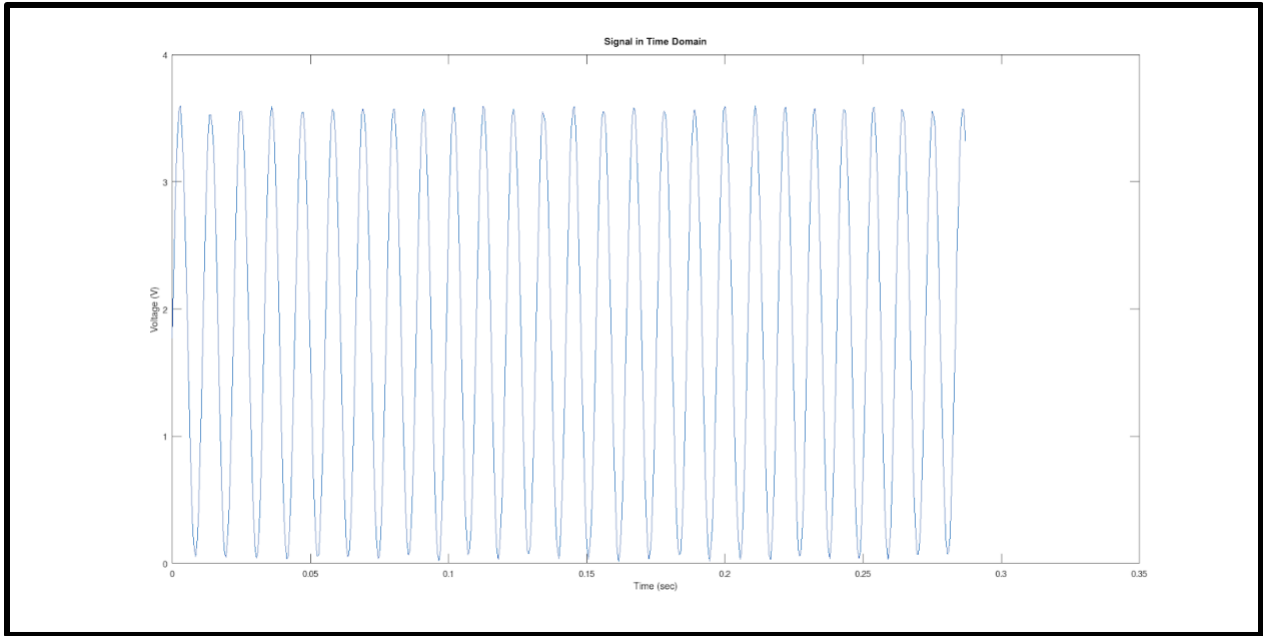


Figure 7-2: A graph of the sine wave input specified above

7.3 Adaptation of the software for the task

7.3.1 Multiple ADC channels

In order to meet the requirements of the project, the inherited software needed to be altered in order to support a higher sampling rate and more than one channel of inputs. Zephyr makes such functionality rather easy to accomplish for the peripheral application itself, as its ADC-reading function requires the specification of the channel being read. The ADC channel specifications were placed in an array which is iterated across when the ADC sample software event is triggered, reading from each channel and storing their value in memory one after another.

The ADC sample software event is set using the `k_timer` interface also supplied by Zephyr, which is initialized before any samples are taken. This timer runs off the system clock and repeats after a specified length of time. Since we intend to sample at 2 kHz, this timer was set to go off every 500 microseconds. It is possible for this timer to go off again even if the ADC sample function has not completed, meaning setting this timer to run too quickly or having a sampling function which is too inefficient can result in erroneous data. However, it functions

properly otherwise. The function called when the timer event is raised can be seen in Figure 7-3, with the `adc_channels` array holding the Zephyr specification of the ADC channels used.

```
void adc_sample(struct k_work *item) {
    int ret;
    static int cnt = 0;
    uint16_t buf;
    struct adc_sequence sequence = {
        .buffer = &buf,
        /* buffer size in bytes, not number of samples */
        .buffer_size = sizeof(buf),
    };

    if (adc_samples == 0) {
        adc_samples = k_malloc(sizeof(*adc_samples));
    }

    //if (adc_dev) {
    if (adc_channels) {
        //LOG_INF("Starting ADC Read");
        for (size_t i = 0U; i < ARRAY_SIZE(adc_channels); i++) {
            (void)adc_sequence_init_dt(&adc_channels[i], &sequence);

            ret = adc_read(adc_channels[i].dev, &sequence);
            if (ret) {
                LOG_INF("ADC Read Failed with code %d\n", ret);
            }
            //printf("%d\n", m_sample_buffer[i]);
            //LOG_INF("ADC raw value: %d from Channel %d\n", m_sample_buffer[i], adc_channels[i].channel_id);
            LOG_INF("ADC raw value: %d from Channel %d\n", buf, adc_channels[i].channel_id);
            //adc_samples->data[cnt++] = m_sample_buffer[i];
            adc_samples->data[cnt] = (uint8_t) (buf & 0x00ff);
            adc_samples->data[cnt+1] = (uint8_t) ((buf >> 8) & 0x000f + i << 4);
            cnt = cnt + 2;

            if (cnt >= UART_BUF_SIZE) {
                cnt = 0;
                adc_samples->len = UART_BUF_SIZE;
                //LOG_INF("Data put in UART Buffer: %d \n", adc_samples->data);
                k_fifo_put(&fifo_uart_rx_data, adc_samples);
                adc_samples = k_malloc(sizeof(*adc_samples));
            }
        }
    }
}
```

Figure 7-3: The function which samples each ADC channel and writes the data to memory.

To explain the Zephyr function calls within this code excerpt: `adc_sequence_init_dt` enables the ADC channel passed to it, `adc_read` writes the value from the channel into `sequence.buffer`, and `k_fifo_put` stores the values in a FIFO buffer which the Bluetooth transmission function reads from. As for the global variables, `adc_channels` is an array containing the Zephyr data for each channel, `adc_samples` is a 40-byte buffer used to set up the Bluetooth packets, and `buf` is a 10-byte buffer of 16-bit unsigned integers that `adc_read` stores values into.

While our use case makes it unlikely (albeit possible) that any data are lost or received in an incomplete form, for the sake of versatility the uppermost 4 bits of the ADC data were used to indicate which channel the datum was read from. Accordingly, the data processing script was also adapted to read these 4 bits, mask them out from the value, and then use them to sort the

data into a 2D array, each row of which constitutes the data from each channel. Each row is then graphed individually in a subplot of a larger figure.

For the purpose of testing that these multiple channels can be read accurately without attributing data points to the wrong channels or electrically interfering with each other's readings, each ADC input was connected to a particular electrical signal. Specifically, channels A2 and A4 were connected to a sine wave identical to the one tested in 7.2.2, A1 was connected to a DC voltage of 3.3V, A0 was connected to a DC voltage of 1.275V, and A3 was connected to a DC voltage of 2.54V. Running the data collection script should result in each of these signals being graphed, with some room for error due to noise, and this can be seen in Figure 7-4.

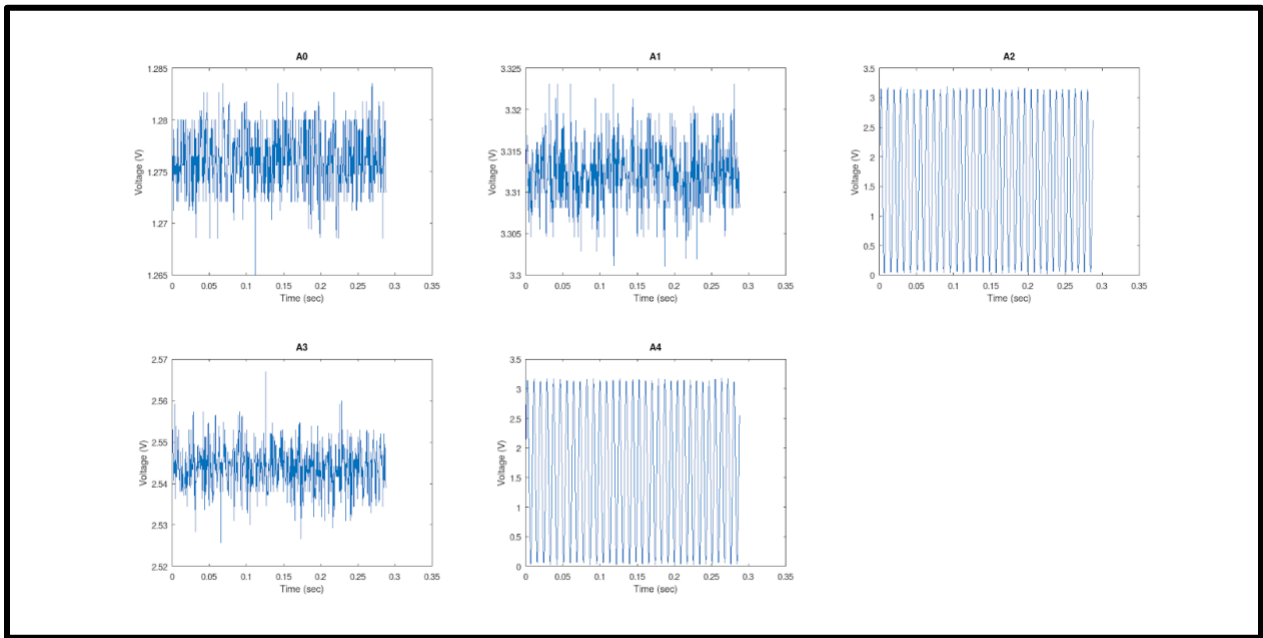


Figure 7-4: A graph of the 5 ADC inputs, with A0 through A2 on the top row and A3 & A4 on the bottom row

7.3.2 Further optimization

The accuracy of the ADC itself can be improved using oversampling, which Zephyr makes available as an option that can be set for any given ADC channel. The oversampling option is set to the log base 2 of the number of samples averaged within one sample period, although the frequency of these is still limited by the acquisition and conversion times.

Alternatively, oversampling can be implemented manually by increasing the sampling rate on the peripheral board and setting up the sample function to do the averaging manually. These approaches could each have different impacts on accuracy and efficiency, and the software implementation has been tested against the ADS1292 for the former. In the code, this was implemented using a for loop within the `adc_sample` function that can be seen in Figure 7-5. This oversamples every ADC channel being sampled as quickly as the CPU allows, and therefore is more accurate when the noise is less correlated. For our purposes the noise was considered to be approximately uncorrelated, however depending on the context an alternative approach may be preferable.

```
uint32_t avg = 0;
for (size_t j = 0U; j < (1 << SOFT_SAMPLES); j++) {
    (void)adc_sequence_init_dt(&adc_channels[i], &sequence);
    ret = adc_read(adc_channels[i].dev, &sequence);
    if (ret) {
        printk("ADC Read Failed with code %d\n", ret);
        LOG_INF("ADC Read Failed with code %d\n", ret);
    }
    avg += buf;
}
avg = avg >> SOFT_SAMPLES;

adc_samples->data[cnt] = (uint8_t) (avg & 0x00ff);
adc_samples->data[cnt+1] = (uint8_t) (((avg & 0x0f00) >> 8) + (i << 4));
cnt = cnt + 2;
```

Figure 7-5: The altered sampling code, which writes an average of $2^{\text{SOFT_SAMPLES}}$ samples into memory instead of a single ADC read. The division and multiplication done with `SOFT_SAMPLES` is done by bit-shifting according to in order to minimize the overhead introduced by this approach.

The ENOB of the software oversampling implementation was calculated from the measured SINAD using the same methodology as described in section 6.4.3. Compared to the ADS1292's effective 17.9668 bits, the nRF52840 ADC without any oversampling exhibited 11.438 effective bits. But, when averaging across 32 samples per data point—the maximum we could use without compromising our overall sampling rate of 2 kHz—using the software oversampling, it achieved 14.611 effective bits. These results indicate that while the accuracy of the ADC on the nRF52840 can be improved, even in the best-case scenario the potential of this is limited in comparison to the ADS1292.

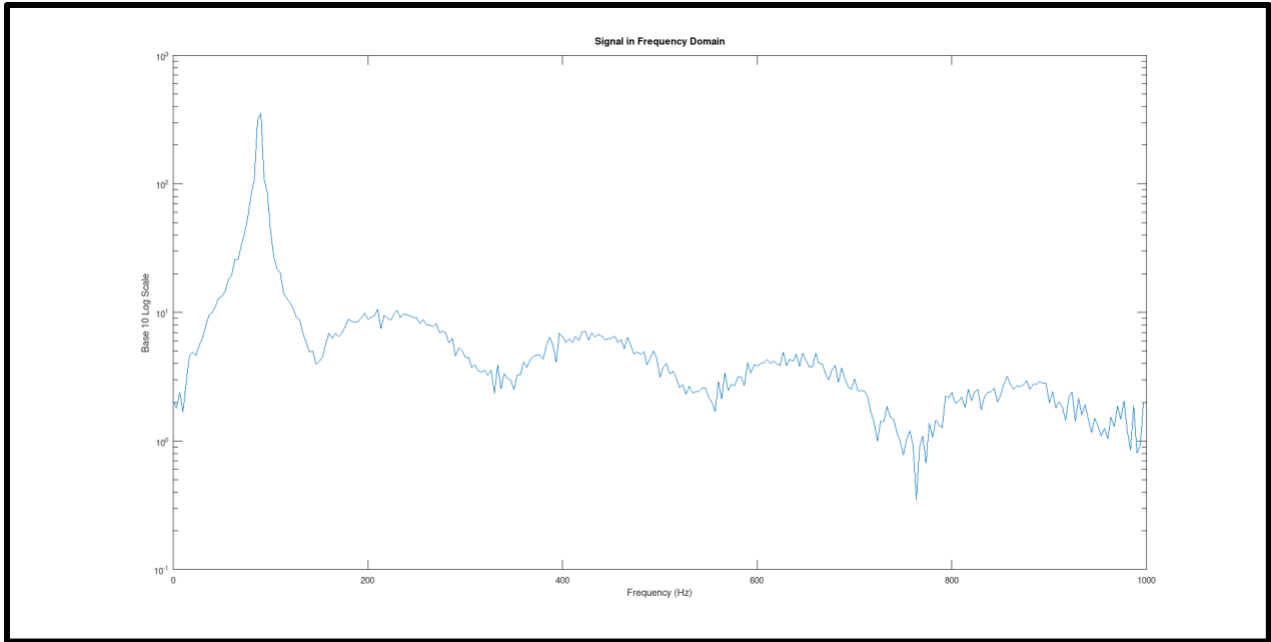


Figure 7-6: A graph of the ADC output with no oversampling in the frequency domain

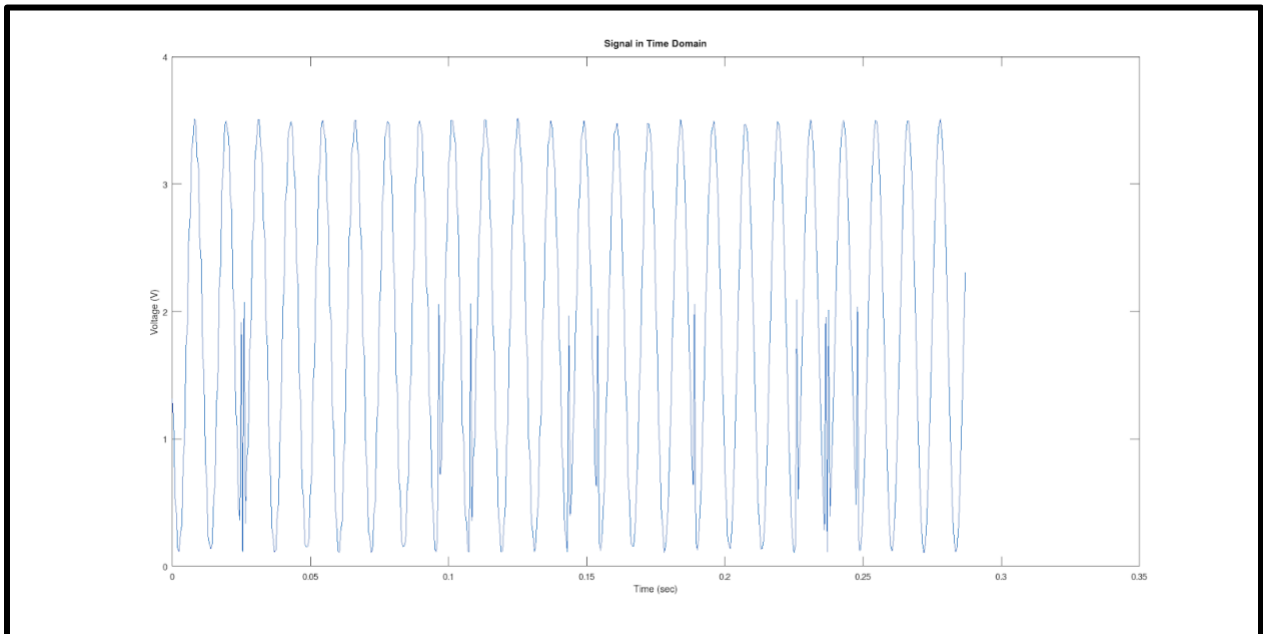


Figure 7-7: A graph of the ADC output oversampled at 32 times the sampling rate in the time domain; compare to Figure 7-2

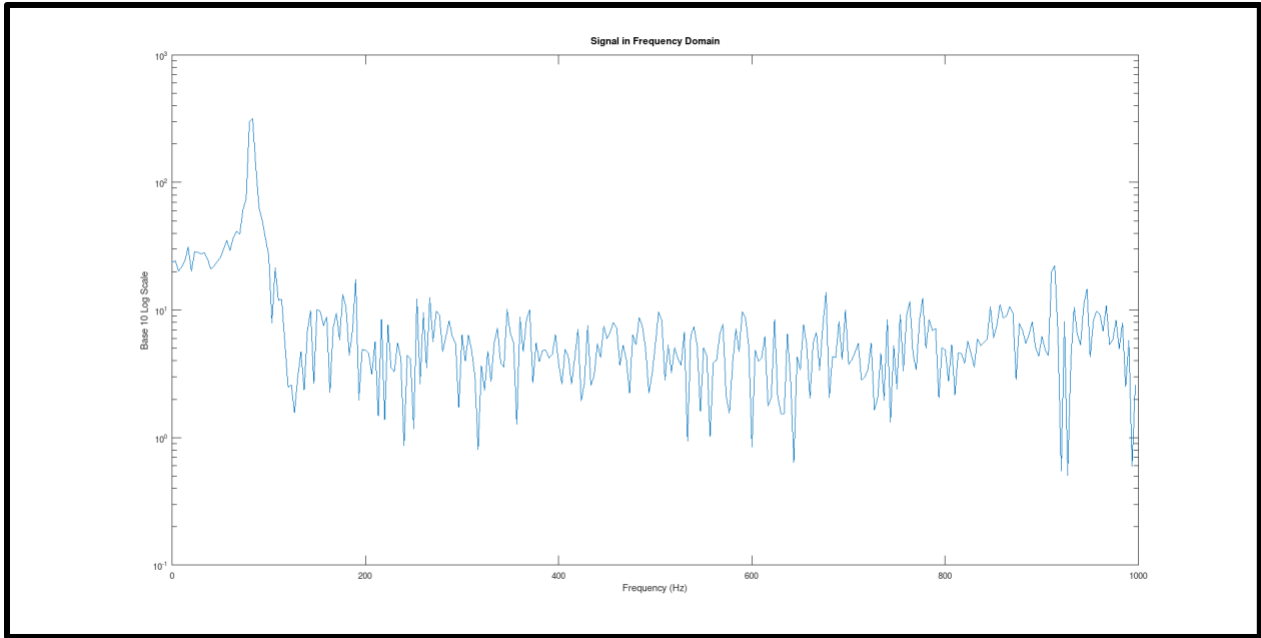


Figure 7-8: A graph of the ADC output oversampled at 32 times the sampling rate in the frequency domain

Additionally, in the design options section of this paper, the maximum viable sampling rate was calculated using the number of BLE transmissions per second presuming that this frequency was inversely proportional to our connection interval. However, the BLE protocol also supports transmitting more than one packet per connection interval. This is a useful feature to take advantage of since it opens up the possibility of transmitting more than 5 channels of data while maintaining a high sampling rate. Additionally, it could allow for a higher sampling rate to be transmitted through BLE with any potential oversampling being done off-line. Implementing this functionality was outside the scope of this project but is brought up here as a point of reference for future improvements on this device.

7.4 Integration with analog front-end

Once the software was sufficiently functional, the outputs of 4 EMG channels were connected to the pins of the ADC to ensure the basic testing was sufficient. While this is a less rigorous test than those with a known input, it should result in 4 graphs that appear to show EMG

signals, which can be seen in Figures 7-9 and 7-10.

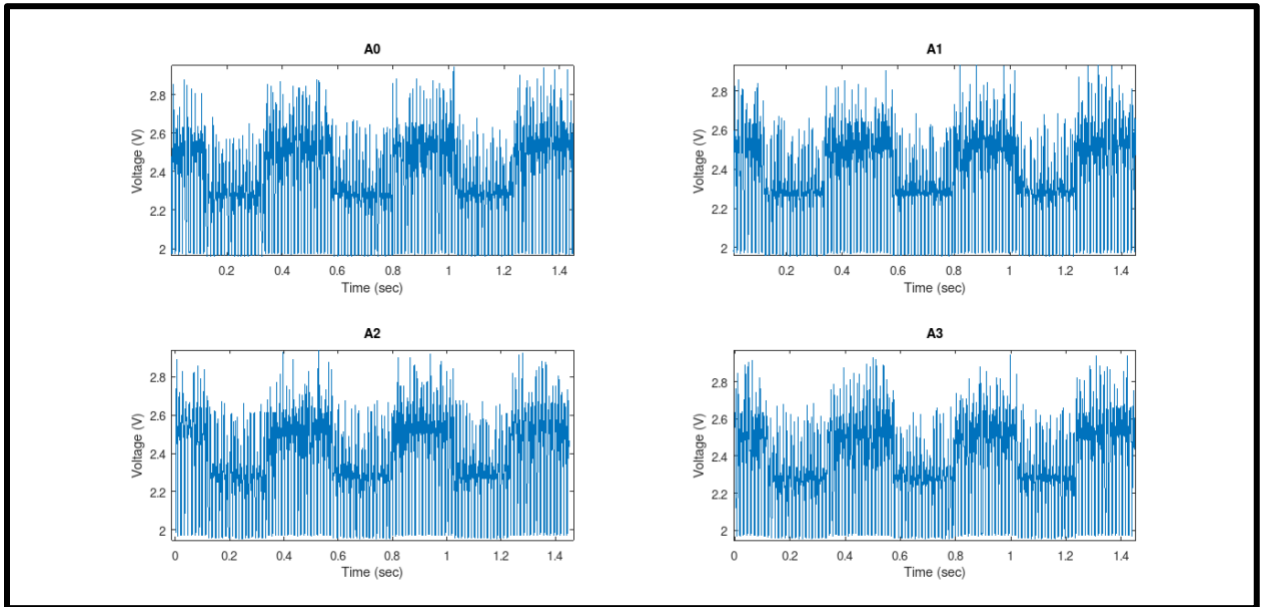


Figure 7-9: EMG output from 4 channels A0 to A3 graphed at a per-sample scale for a 2 kHz sampling rate

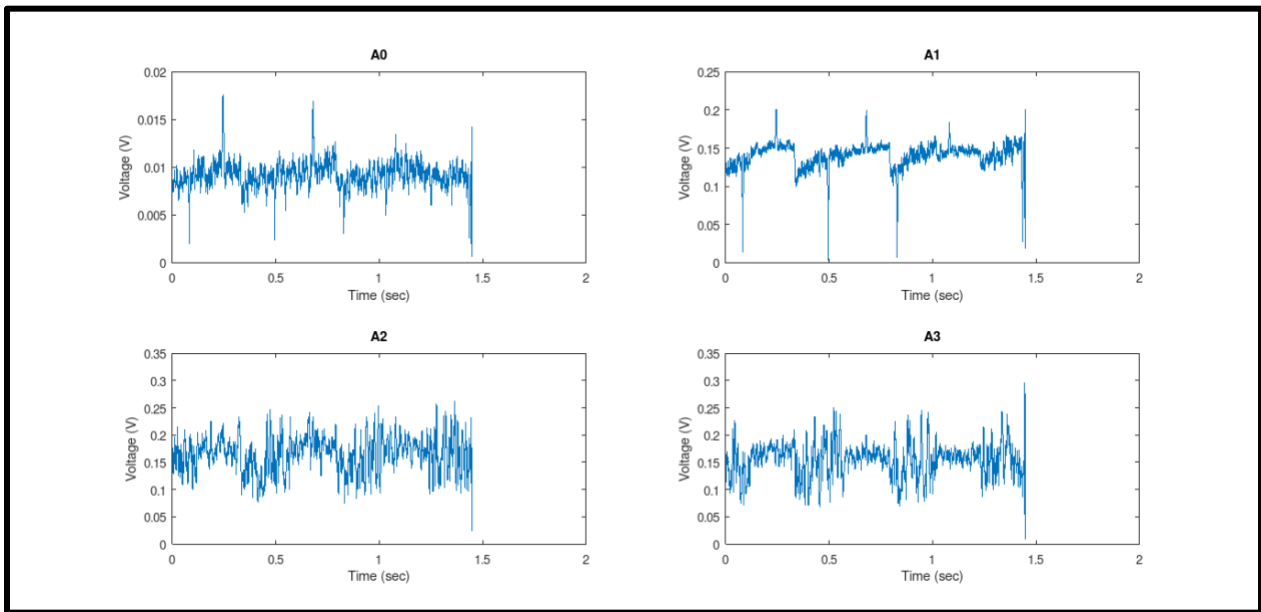


Figure 7-10: The same data from Figure 7-9, full wave rectified and smoothed by a moving RMS average with a window of 10 samples. Here one can roughly see 4 similar contractions across each of the probes.

8. Shoulder System Integration

This project aims to combine four EMG channels into an integrated wireless package on the shoulder. Using four EMG channels, the placement of each electrode must be carefully considered to ensure useful, and clear obtainable data. The team chose the four following muscles based on a variety of motions for shoulder rehabilitation:

1. Trapezius: The triangular muscles extending over the back of the neck and shoulders.
2. Pectoralis Major: The largest muscle of the anterior chest wall
3. Infraspinatus: The muscle on the surface of the scapula
4. Anterior Deltoid: The muscles connecting the upper part of the shoulder blade (scapula) to the clavicle that help move your arm forward.

Each of these muscles was previously discussed in section 2.3 and a detailed diagram of their locations is located in Figures 2-2 and 2-3. The electrodes were created using dome head screws and wired using medically insulating wire. Each channel connects to both electrodes, and there is an additional electrode used as reference, which is placed on the clavicle of the subject, a part of the shoulder with little muscle.

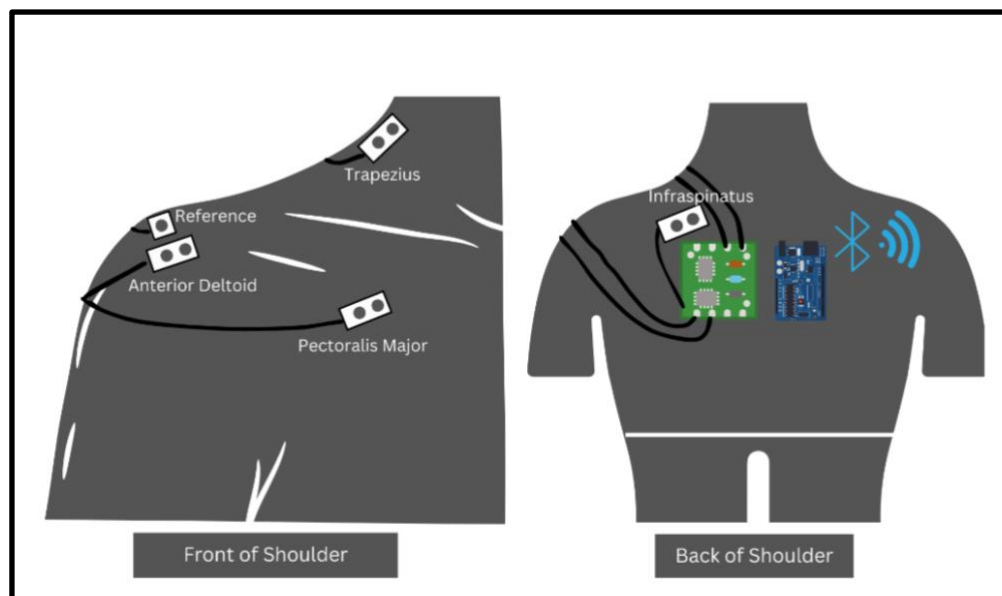


Figure 8-1: Shoulder system electrode placement

Each electrode is held in place on the inside of the strap with Velcro, which allows for electrodes to be moved according to each individual patient and their muscles. Placement flexibility allows any and all patients to use the product. For better data acquisition, a small drop of electrode gel was used for many tests, which decreases the impedance barrier between the skin and electrode.

All solder boards, microcontroller and other components are stored on the back side of the shoulder. The attachment of each electrode wire is removable, which allows for flexibility of the number of EMG channels used. The entire system is completely wireless, running completely battery operated, and communicates to the peripheral control unit through Bluetooth low energy (BLE). A picture of the completed system in use on a subject can be seen in Figure 8-2. The subject is collecting EMG data from all four muscles by extending his right arm to the side. The two solder boards, microcontroller, and batteries are mounted on an acrylic plate and attached to the back. The wires leading to each electrode come out from the inside of the shirt via a stitched hole and connect to each EMG channel. The approximate location of where 3 EMG electrodes are placed under the shirt are shown, with an additional Trapezius electrode on the front side.

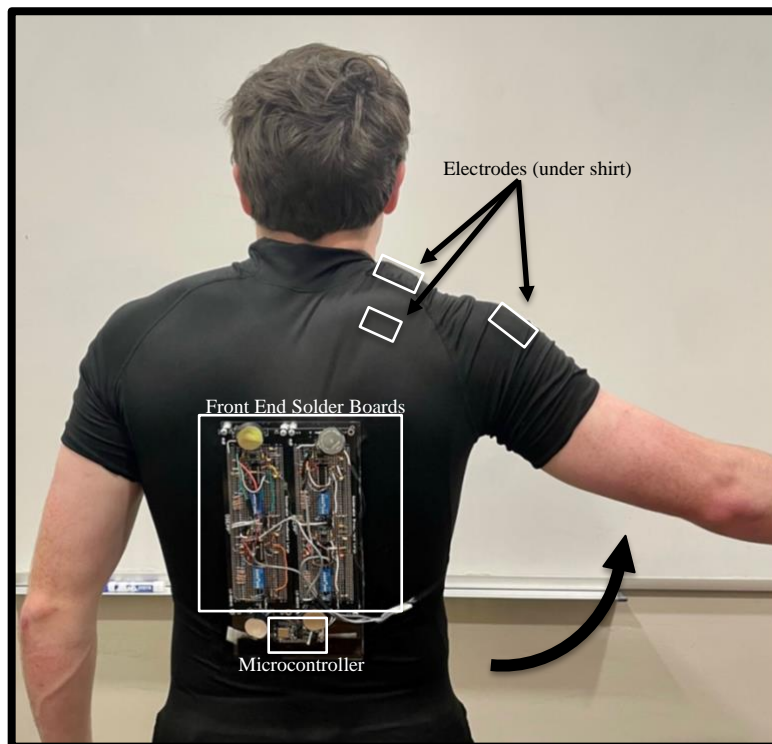


Figure 8-2: EMG shoulder sleeve in use on subject.

9. System Discussion

The completed system functions as expected based on the design goal for this project. A wireless sleeve was created that is able to collect data from multiple EMG channel leads and send data wirelessly to a receiving computer. With this, some aspects of the project were designed with a tight timeline in mind, and therefore many areas of improvement arose from the team's experimental work on this design. The design was broken down into three major sections: the EMG front end, the Nordic microcontroller Bluetooth communication, and the system package.

The EMG front end delivered almost all of the required specifications as demonstrated by data verification. Even so, the design process revealed many areas of oversight that, while functional, could have been improved if time permitted. For a wireless device, an efficient power management system is crucial, and a better-planned power supply, driven by a charge pump and more efficient voltage regulation, could have been more efficient. The analog stages also revealed a larger-than-expected total package, that could be reduced through a PCB design or a higher bit ADC for more digital control and removal of the selectable gain stage.

The shoulder system package combining the front end and the microcontroller validates the theorized design of a multi-channel EMG system, but more mechanical design work is needed to meet the end goal of a versatile and modular system that is compelling to patients. Our compression-shirt design proves the movability of electrodes, on-patient electronics housing, and a fully wireless design. The electrodes used, while functional, are also preliminary and would benefit from future research for optimal electrode size, placement, and shape for the four shoulder muscles being tested.

The microcontroller software and data processing scripts were able to deliver the required specifications of the project. The required features were also iterated on to achieve higher precision via oversampling the ADC. The most significant area for improvement in this area is the transmission of only one Bluetooth packet per connection interval; improving upon this limitation would not only allow for more data channels such as an additional EMG channel or a 6-channel IMU but would also allow for data taken at a higher sampling rate by the ADC to be

transmitted. Other areas for improvement include replacing the use of the nRF52840 ADC outright using the ADS1292 and implementing a real-time display of the data.

While this design opted for a fully analog EMG front end, the ADS1292 proved to be a possible option for future EMG systems. This option was originally not chosen due to the lack of experience with this microcontroller, the unknowns of system noise, power consumption, and overall use with EMG signals since it is designed for higher magnitude ECG applications. The research completed in our investigation showed that the advantages of the ADS1292 board are that it is all built into one microcontroller, so it is smaller, not expensive, does its own analysis, works for the range of voltages in our application, and is low noise. The disadvantages are that the software is outdated which creates problems in installation and while running, there are limitations in the number of channels and gain despite its effective number of bits and would still be connected to a microcontroller.

10. Conclusion

Our research helped us to develop a prototype shoulder mounted EMG system which with continued research could be a feasible tool for shoulder muscle monitoring. Based on product requirements specified previously, the system created either meets or delivers a path to satisfy every requirement. Through our experimentation with a variety of these device constraints, the team was able to determine parts of the system where further research could be beneficial, including:

1. The most efficient power delivery method for wireless multi-channel EMG front ends.
2. Real-time viewing of a wirelessly received EMG signal.
3. An experimental comparison between an ADS 1292 system and a 24-bit ADC system.

From a front-end standpoint, future research should consider a prototyped ADS 1292 system with its minimal noise, greater on-the-fly customization, and smaller footprint. The front end of this project was very large, so an integrated package like the ADS1292 or a PCB assembly would be the next step in making a shoulder EMG system useful in practice.

From a system level, more research and consideration of the shoulder package and EMG electrodes should be investigated. A desired option should give mobility of the electrodes when the strap is removed while being secure when placed on a subject.

With regards to the software, the system has no form of real-time display, and could be made more efficient with improvements to the Bluetooth transmission. Moreover, the software would need to be adapted if the ADS 1292 or an IMU were to be incorporated into the design.

Overall, the system created is still in a prototype phase of development and would require further research before moving to a more robust design that limits changes. Once the provided potential areas of improvement are researched, this multi-channel EMG system will provide a practical tool for shoulder recovery and monitoring and would meet the required specifications for the system.

Appendix A

The data in Table A-1 was collected to evaluate level shifter conditions when $V_{REF} = V_{IN} = 4$ to help determine the proper value of R_A needed to shift the EMG signal by 1.8V and keep the current I_D from becoming negative.

R_A	I_D
2M Ω	4.43 μ A
1.5M Ω	4.80 μ A
1M Ω	5.53 μ A
500k Ω	7.73 μ A
400k Ω	8.83 μ A
300k Ω	10.7 μ A
290k Ω	10.9 μ A
280k Ω	11.2 μ A
270k Ω	11.5 μ A
260k Ω	11.8 μ A
250k Ω	12.1 μ A
240k Ω	12.5 μ A
230k Ω	12.9 μ A
220k Ω	13.3 μ A
210k Ω	13.8 μ A
200k Ω	14.3 μ A
190k Ω	14.9 μ A
180k Ω	15.6 μ A
170k Ω	16.3 μ A
160k Ω	17.1 μ A
150k Ω	18.0 μ A

140k Ω	19.0 μ A
130k Ω	20.3 μ A
120k Ω	21.7 μ A

Table A-1: $V_{REF} = V_{IN}$, R_A must be extremely large before I_D will be zero or negative.

The data in Table A-2 was collected to evaluate level shifter conditions when $V_{REF} = 4V$, $V_{IN} = -4V$ to help determine the proper value of R_A needed to shift the EMG signal by 1.8V and keep the current I_D from becoming negative.

R_A	I_D
260k Ω	-326nA
255k Ω	-160nA
254k Ω	-126nA
253k Ω	-92.2nA
252k Ω	-57.7nA
251k Ω	-22.9nA
250k Ω	12.1nA
245k Ω	192nA
240k Ω	379nA
235k Ω	574nA
230k Ω	777nA
225k Ω	990nA
220k Ω	1.21 μ A
215k Ω	1.44 μ A
210k Ω	1.69 μ A
205k Ω	1.94 μ A
200k Ω	2.21 μ A
195k Ω	2.49 μ A

Table A-2: I_D becomes negative between 250k Ω and 251k Ω , as shown in red.

The data in Table A-3 was collected to evaluate level shifter conditions when $V_{REF} = 4V$, $V_{IN} = 0$ to help determine the proper value of R_A needed to shift the EMG signal by 1.8V and keep the current I_D from becoming negative.

R_A	I_D
810k Ω	-11.2nA
809k Ω	-7.87nA
808k Ω	-4.50nA
807k Ω	-1.13nA
806k Ω	2.25nA
805k Ω	5.64nA
800k Ω	22.7nA
700k Ω	416nA
600k Ω	939nA
500k Ω	1.67 μ A
400k Ω	2.77 μ A
350k Ω	3.56 μ A
340k Ω	3.74 μ A
330k Ω	3.94 μ A
320k Ω	4.15 μ A
310k Ω	4.37 μ A
300k Ω	4.61 μ A
290k Ω	4.86 μ A
280k Ω	5.13 μ A
270k Ω	5.42 μ A
260k Ω	5.73 μ A
250k Ω	6.07 μ A

240k Ω	6.44 μ A
230k Ω	6.84 μ A
220k Ω	7.27 μ A
210k Ω	7.75 μ A
200k Ω	8.27 μ A
190k Ω	8.85 μ A
180k Ω	9.49 μ A

Table A-3: I_D becomes negative between 806k Ω and 807k Ω , as shown in red.

Appendix B

The MATLAB script below is used to plot the theoretical frequency response of the instrumentation amplifier, based on parameters Rg, R1, and Cg, which are set within the script.

```
function iamp_stage_v01
% Components.
Rg = 2600;
R1 = 24.7E3;
Cg = 5E-6;
% Frequency values at which to evaluate.
f = 0:0.01:200;
w = 2*pi*f;
fdata = [5,10,20,50,100,140,180,200];
mag_data =
[13.72340426,27.51937984,44.8,61.47540984,61.40684411,62.40310078,61.64122137
,62.890
625];
phase_data = [64.8,64.8,51.84,21.6,21.6,0,0,0];
% Frequency response.
H = 1 + ( 2*R1 ./ (Rg + (1./(1j*w*Cg))) );
figure(1)
% Plot magnitude only.
%plot(fdata,mag_data,':b.')
title('Ideal and recorded magnitude response')
hold on
plot(f, abs(H), 'k')
% Passband gain line.
Hpass = 1 + ( 2*R1 ./ Rg );
hold on, plot([f(1) f(end)], [Hpass Hpass], 'k--'), hold off
box('off')
xlabel('Frequency (Hz)')
ylabel('Magnitude Response')
title('Wireless EMG I-Amp Circuit')
legend('Ideal')
%legend('Recorded data','Ideal')
Return
```

Appendix C

MATLAB Code Used to Calculate ENOB

```
1 a = table2array(practice3); %Reading Data from Excel Spreadsheet and Converting it to an Array
2 a = str2double(a);
3 DFT = fft(a-mean(a)); %Taking the DFT of the Data Minus the Mean of the Data
4 DFT = abs(DFT(1:(length(DFT)/2 + 1))); %Taking the Absolute Value and Only First Half of the DFT
5 figure(1)
6 semilogy(DFT(2:end)) %Plotting the DFT
7 title('Signal in Frequency Domain')
8 xlabel('Data Points')
9 ylabel('Base 10 Log Scale')
10 Fsamp = 2000; %Setting the Sampling Frequency
11 M = length(a); %Number of Points in Data
12 t = [0:length(a)-1]/Fsamp; %Setting Time for X Axis
13 figure(2) %Plotting the Signal in Time Domain
14 plot(t,a)
15 title('Signal in Time Domain')
16 xlabel('Time (sec)')
17 ylabel('Voltage (V)')
18 Vpp = peak2peak(a); %Finding the Peak to Peak Voltage of the Signal
19 %fullScale = 5; %The full scale range of the ADC
20 RMS = rms(a-mean(a)); %Finding the RMS Voltage of the Signal Minus its Mean
21 Amp = RMS*sqrt(2); %Estimating the Amplitude of the Fitted Signal
22 [~,i] = max(DFT); %Finding the data point of the fundamental frequency
23 Freq = ((i-1)*Fsamp)/M; %Estimating the Frequency of the Fitted Signal
24 a = a-mean(a);
25 fun = @(phase)(Amp*sin((2*pi*Freq*t)+phase))-a;
26 x0 = 0; %Guessing the Phase to be 0
27 x = lsqnonlin(fun,x0); %Estimating the Phase of the Fitted Signal
28 figure(3)
29 plot(t,a,'--',t,Amp*sin((2*pi*Freq*t)+x),'b-') %Plotting the Fitted Signal on top of the Collected Signal
30 title('Collected Signal and Fitted Signal in Time Domain')
31 legend('Data','Best fit')
32 xlabel('Time (sec)')
33 ylabel('Amp*sin((2*pi*Freq*t)+phase)')
34 fit = Amp*sin((2*pi*Freq*t)+x); %The fitted signal
35 fit = fit'; %Taking transpose of fitted signal data to make it a column array
36 error = a-fit; %Finding the Error of the Fitted Signal
37 figure(4)
38 plot(t,error) %Plotting the Error of Fitted Signal
39 title('Error of the Collected Signal and Fitted Signal in Time Domain')
40 xlabel('Time (sec)')
41 ylabel('Amp*sin((2*pi*Freq*t)+phase)')
42 sum = 0;
43 for n = 1:M
44     sum = sum + ((a(n)-fit(n))^2); %Taking Sum of (Signal Minus Fitted Signal) Squared
45 end
46 NAD = sqrt((1/M)*sum); %Calculating NAD
47 Arms = ((Vpp)/2)/(sqrt(2)); %Calculating Arms
48 SINAD = Arms/NAD; %Calculating SINAD
49 realSINAD = SINAD*10; %Converting SINAD to Right Units
50 ENOB = (realSINAD-1.76)/(6.02); %Calculating ENOB
```


Appendix D

MATLAB function `butter_hi_design.m`, which is used to calculate component values for designing a low pass Butterworth filter. Instructions for using the script can be found within the comments of the function.

```
function H = butter_hi_design(f, Fc, A, Stage1, Stage2, Stage3, Stage4, Stage5)
%
% H = b_hi_des(f, Fc, A, Stage1[, Stage2[, Stage3[, Stage4[, Stage5]]])
%
% Helps design an electronic circuit to build even-order, high-pass
% Butterworth filters of orders 2, 4, 6, 8, 10. Plots the magnitude of
% the resulting frequency response.
% See [Thomas Kugelstadt, "Chapter 16: Active
% Filter Design Techniques," Literature Number SLOA088, Texas Instruments
% Incorporated, Post Office Box 655303, Dallas, Texas 75265, 2001.
% Excerpted from "Op Amps for Everyone," Literature Number SLOD006A,
% Texas Instruments. Available on the Internet at: http://www.ti.com].
%
% f: Frequency axis (Hertz) for all calculations and plotting (vector).
% A: Overall circuit gain (>=1). Applied in 1st stage.
% Fc: Desired cutoff frequency in Hertz (scalar).
% StageX: Up to 5 StageX arguments (one per stage) are permitted. For each stage,
% StageX is a vector of 1-4 elements, corresponding to C1, C2,
% R1 and R2, respectively. C1 must be supplied (in Farads) and
% is the first vector element. If a second argument is supplied,
% then it is C2 (in Farads). If C2 is not supplied, it is set
% equal to C1. If
% a third argument is supplied, it is R1 (Ohms). If not supplied,
% it is set as required to form a Butterworth filter. If a fourth
% argument is supplied, it is R2 (Ohms). If not supplied, it is
% set as required to form a Butterworth filter.
%
% H: Resulting (complex-valued) frequency response corresponding to the
```

```

% frequency axis f.
%
% USAGE RECOMENDATIONS: To build a filter, initially call script with only
% C1 and C2 specified for each stage. Use the recommended
% R1 and R2 values to find R1's and R2's that are manufactured. Call the
% script a second time with all values to see the resultant nominal frequency
% response.

% Table of ai values. For even-order Butterworth, all bi values equal 1.
aiTable = [1.4142 NaN NaN NaN NaN; % For 1-stage filter.
           1.8478 0.7654 NaN NaN NaN; % For 2-stage filter.
           1.9319 1.4142 0.5176 NaN NaN; % For 3-stage filter.
           1.9616 1.6629 1.1111 0.3902 NaN; % For 4-stage filter.
           1.9754 1.7820 1.4142 0.9080 0.3129]; % For 5-stage filter.

% Determine the number of stages.
Nstage = nargin - 3;
if Nstage<1 | Nstage>5, error("Must have 1-5 stages."); end
if A<1, error("'A' must be >= 1."); end

% Extract/develop parameters for each stage and build the frequency response.

H = ones( 1, length(f) ); % Initialize frequency response to unity.
w = 2*pi*f; % Convert to radian frequency.
MagBig = A; % Cascade passband gain.

for S = 1:Nstage

    if S>1, A = 1; end % Set gain to one after first stage.

    % Prepare to parse parameter vector.
    eval(['Param = Stage' int2str(S) ';']); % Copy parameters to a scratch vector.
    if length(Param)<1, error(['Stage ' int2str(S) ' parameter list < 1.']); end;

```

```

if length(Param)>4, error(['Stage ' int2str(S) ' parameter list > 4.']); end;
ai = aiTable(Nstage,S);

% Parse parameter vector.
% C1.
C1 = Param(1);
% C2.
if length(Param)>1, C2 = Param(2); else, C2 = C1; end
% R1.
if length(Param)>2, R1 = Param(3);
elseif A==1
    R1 = ( C1+C2 ) / ( 2*pi*Fc*ai*C1*C2 );
else
    a = ((2*pi*Fc)^2) * C1*C2*C2*(1-A);
    b = -ai * 2*pi*Fc * C1*C2;
    c = C1 + C2;
    R1 = ( -b - sqrt(b*b - 4*a*c) ) / (2*a);
end
% R2.
if length(Param)>3, R2 = Param(4);
else, R2 = 1 / ( ((2*pi*Fc)^2)*R1*C1*C2 ); end

% Print component values.
fprintf('Stage %d: C1=%e F, C2=%e F, R1=%e Ohms, R2=%e Ohms\n', S, C1, C2, R1, R2);

% Update frequency response.
a = ( R2*(C1+C2) + R1*C2*(1-A) ) ./ (R1*R2*C1*C2);
b = 1 ./ (R1*R2*C1*C2);
Hstage = A ./ ( 1 + ( a./(j*w) ) + ( b./(-w.*w) ) );
H = H .* Hstage;
end

% Now, plot the frequency response magnitude.

```

```
plot( f, abs(H) )
xlabel('Frequency in Hertz')
ylabel('Frequency Response Magnitude')

L1 = find( abs(H) >= (MagBig*sqrt(2)/2) );
hold on, plot([f(L1(1)) f(L1(1))], [0 MagBig], 'm'), hold off
Thing = sprintf('Cut-off at %0.2f Hz, Passband Gain = %0.2f', f(L1(1)), MagBig);
text( max(f)/5, max(abs(H))/3, Thing);
title('Butterworth High-Pass Filter');

figure(gcf);

return
```

Appendix E

MATLAB function `butter_lo_design.m`, which is used to calculate component values for designing a low pass Butterworth filter. Instructions for using the script can be found within the comments of the function.

```
function H = butter_lo_design(f, Fc, A, Stage1, Stage2, Stage3, Stage4, Stage5)
%
% H = b_lo_des(f, Fc, A, Stage1[, Stage2[, Stage3[, Stage4[, Stage5]]])
%
% Helps design an electronic circuit to build even-order, low-pass
% Butterworth filters of orders 2, 4, 6, 8, 10. Plots the magnitude of
% the resulting frequency response.
% See [Thomas Kugelstadt, "Chapter 16: Active
% Filter Design Techniques," Literature Number SLOA088, Texas Instruments
% Incorporated, Post Office Box 655303, Dallas, Texas 75265, 2001.
% Excerpted from "Op Amps for Everyone," Literature Number SLOD006A,
% Texas Instruments. Available on the Internet at: http://www.ti.com].
%
% f: Frequency axis (Hertz) for all calculations and plotting (vector).
% A: Overall circuit gain (>=1). Applied in 1st stage.
% Fc: Desired cutoff frequency in Hertz (scalar).
% StageX: Up to 5 StageX arguments (one per stage) are permitted. For each stage,
% StageX is a vector of 1-4 elements, corresponding to C1, C2,
% R1 and R2, respectively. C1 must be supplied (in Farads) and
% is the first vector element. If a second argument is supplied,
% then it is C2 (in Farads). If C2 is not supplied, it is set
% equal to C1. If
% a third argument is supplied, it is R1 (Ohms). If not supplied,
% it is set as required to form a Butterworth filter. If a fourth
% argument is supplied, it is R2 (Ohms). If not supplied, it is
% set as required to form a Butterworth filter.
%
% H: Resulting (complex-valued) frequency response corresponding to the
```

```

% frequency axis f.
%
% USAGE RECOMENDATIONS: To build a filter, initially call script with only
% C1 and C2 specified for each stage. Use the recommended
% R1 and R2 values to find R1's and R2's that are manufactured. Call the
% script a second time with all values to see the resultant nominal frequency
% response.

% Table of ai values. For even-order Butterworth, all bi values equal 1.
aiTable = [1.4142 NaN NaN NaN NaN; % For 1-stage filter.
           1.8478 0.7654 NaN NaN NaN; % For 2-stage filter.
           1.9319 1.4142 0.5176 NaN NaN; % For 3-stage filter.
           1.9616 1.6629 1.1111 0.3902 NaN; % For 4-stage filter.
           1.9754 1.7820 1.4142 0.9080 0.3129]; % For 5-stage filter.

% Determine the number of stages.
Nstage = nargin - 3;
if Nstage<1 | Nstage>5, error("Must have 1-5 stages."); end
if A<1, error("'A' must be >= 1."); end

% Extract/develop parameters for each stage and build the frequency response.

H = ones( 1, length(f) ); % Initialize frequency response to unity.
w = 2*pi*f; % Convert to radian frequency.
MagBig = A; % Cascade passband gain.

for S = 1:Nstage

    if S>1, A = 1; end % Set gain to one after first stage.

    % Prepare to parse parameter vector.
    eval(['Param = Stage' int2str(S) ';']); % Copy parameters to a scratch vector.
    if length(Param)<1, error(['Stage ' int2str(S) ' parameter list < 1.']); end;

```

```

if length(Param)>4, error(['Stage ' int2str(S) ' parameter list > 4.']); end;
ai = aiTable(Nstage,S);

% Parse parameter vector.
% C1.
C1 = Param(1);
% C2.
if length(Param)>1, C2 = Param(2); else, C2 = C1; end
% R1.
if length(Param)>2, R1 = Param(3);
else
    a = ((2*pi*Fc)^3) * C2 * ( C1 + (1-A)*C2 );
    b = -ai * C2 * ((2*pi*Fc)^2);
    c = 2*pi*Fc;
    R1 = ( -b - sqrt(b*b - 4*a*c) ) / (2*a);
end
% R2.
if length(Param)>3, R2 = Param(4);
else, R2 = 1 / ( ((2*pi*Fc)^2)*R1*C1*C2 ); end

% Print component values.
fprintf('Stage %d: C1=%e F, C2=%e F, R1=%e Ohms, R2=%e Ohms\n', S, C1, C2, R1, R2);

% Update frequency response.
a = C1*(R1+R2) + (1-A)*R1*C2;
b = R1 * R2 * C1 * C2;
Hstage = A ./ ( 1 + ( a*j*w ) - ( b*w.*w ) );
H = H .* Hstage;
end

% Now, plot the frequency response magnitude.
plot( f, abs(H) )
xlabel('Frequency in Hertz')

```

```
ylabel('Frequency Response Magnitude')

L1 = find( abs(H) <= (MagBig*sqrt(2)/2) );
hold on, plot([f(L1(1)) f(L1(1))], [0 MagBig], 'm'), hold off
Thing = sprintf('Cut-off at %0.2f Hz, Passband Gain = %0.2f', f(L1(1)), MagBig);
text( max(f)/5, max(abs(H))/3, Thing);
title('Butterworth Low-Pass Filter');

figure(gcf);

return
```


References

- Al Ghatri, M., Lindsay, J. (2012, February 7). *A Brief Review: History to Understand Fundamentals of Electrocardiography*. Journal of Community Hospital Internal Medicine Perspectives. [Full article: A brief review: history to understand fundamentals of electrocardiography \(tandfonline.com\)](https://doi.org/10.1177/0898010112447888)
- American Academy of Orthopedic Surgeons. (2022). *Rotator cuff and shoulder conditioning program - orthoinfo - Aaos*. OrthoInfo. <https://orthoinfo.aaos.org/en/recovery/rotator-cuff-and-shoulder-conditioning-program/>
- Analog Devices, Inc. (2022). AD8422: Low Power, Precision Instrumentation Amplifier Datasheet (Rev. 0). Analog Devices. <https://www.analog.com/media/en/technical-documentation/data-sheets/ad8422.pdf>
- Ang, W.T., Khosla, P.K., Riviere, C.N. (2003). *Design of all-accelerometer inertial measurement unit for tremor sensing in hand-held microsurgical instrument*. 2003 IEEE International Conference on Robotics and Automation, Taipei, Taiwan, pp. 1781-1786 vol.2, doi: 10.1109/ROBOT.2003.1241852.
- Beshara P, Chen JF, Read AC, Lagadec P, Wang T, Walsh WR. *The Reliability and Validity of Wearable Inertial Sensors Coupled with the Microsoft Kinect to Measure Shoulder Range-of-Motion*. *Sensors*. 2020; 20(24):7238. <https://doi.org/10.3390/s20247238>
- BionIT Labs. (2023, January 13). *EMG: The signal that gives you an hand!*. BionIT Labs Turning Disabilities Into New Possibilities. <https://bionitlabs.com/emg-signals/>
- Bluetooth Special Interest Group. (2023, January 19). *Core Specification 5.4*. <https://www.bluetooth.com/specifications/specs/core-specification-5-4/>
- Britannica, T. Editors of Encyclopaedia (2023, April 21). pectoralis muscle. Encyclopedia Britannica. <https://www.britannica.com/science/pectoralis-muscle>

- Cadogan, M. (2022, January 30). *ECG Lead Positioning*. Life in the Fast Lane. [ECG Lead positioning • LITFL • ECG Library Basics](#)
- Chang, K. M., Liu, P. T., & Wei, T. S. (2022). Electromyography Parameter Variations with Electrocardiography Noise. *Sensors (Basel, Switzerland)*, 22(16), 5948. <https://doi.org/10.3390/s22165948>
- Chong, H. J., Kwon, C.-K., Kang, H.-J., & Kim, S. J. (2016). Analysis of upper arm muscle activation using surface electromyography signals during drum playing. *Journal of Exercise Rehabilitation*, 12(3), 188–193. <https://doi.org/10.12965/jer.1632562.281>
- Clancy, E. A., Rajotte, K. Wooding, A. Li, J. McDonald, E. Huang, X. Farrell, R. T. (2023). *Power Consumption and Maximum Number of Supported Nodes for BLE Biosensor Applications*. Accepted for publication.
- Crompton, R. H., Tangen, C., Cummings, S. W., Wood, B. (2023, September 5). human muscle system. Encyclopedia Britannica. <https://www.britannica.com/science/human-muscle-system>
- Davies, J. H. (2008). Embedded Electronic Systems and Microcontrollers. In *MSP430 Microcontroller Basics* (pp. 1–16, 393-396). Newnes, Burlington MA. ISBN: 978-0-7506-8276-3
- De Luca, C. J., Gilmore, L. D., Kuznetsov, M., & Roy, S. H. (2010). *Filtering the surface EMG signal: Movement artifact and baseline noise contamination*. *Journal of biomechanics*, 43(8), 1573–1579. <https://doi.org/10.1016/j.jbiomech.2010.01.027>
- Edwards, P. K., Kwong, P. W., Ackland, T., Wang, A., Donnelly, C. J., & Ebert, J. R. (2021). Electromyographic Evaluation of Early-Stage Shoulder Rehabilitation Exercises Following Rotator Cuff Repair. *International Journal of Sports Physical Therapy*, 16(6). <https://doi.org/10.26603/001c.29513>
- Energizer. (n.d.). *Product datasheet - energizer*. Energizer Product Data Sheet. Energizer: St. Louis, Missouri. <https://data.energizer.com/pdfs/nh22-175.pdf>

- Farina, D., & Holobar, A. (2016). Characterization of human motor units from surface EMG decomposition. *Characterization of Human Motor Units From Surface EMG Decomposition*, Proceedings of the IEEE 104(2), 353–373.
<https://doi.org/10.1109/jproc.2015.2498665>
- Fiore, M. J. (2021). *Operational Amplifiers & Linear Integrated Circuits: Theory and Application*. James Fiore. Utica, New York. ISBN13: 978-1796856897.
- Freehill, M. T., Murray, I. R., Calvo, E., Lädemann, A., & Srikumaran, U. (2023). Shoulder Surgery Postoperative Immobilization: An International Survey of Shoulder Surgeons. *Biology*, 12(2), 291. <https://doi.org/10.3390/biology12020291>
- Gallina, A., Disselhorst-Klug, C., Farina, D., Merletti, R., Besomi, M., Holobar, A., Enoka, R. M., Hug, F., Falla, D., Sjøgaard, K., McGill, K., Clancy, E. A., Carson, R. G., van Dieën, J. H., Gandevia, S., Lowery, M., Besier, T., Kiernan, M. C., Rothwell, J. C., ... Hodges, P. W. (2022). Consensus for experimental design in Electromyography (CEDE) project: High-density surface electromyography matrix. *Journal of Electromyography and Kinesiology*, 64, 102656–102656. <https://doi.org/10.1016/j.jelekin.2022.102656>
- Gao, Shuo, Gong, J., Chen, B., Zhang, B., Luo, F., Yerabakan, M. O., Pan, Y., & Hu, B. (2022). Use of Advanced Materials and Artificial Intelligence in Electromyography Signal Detection and Interpretation. *Advanced Intelligent Systems*, 4(10).
<https://doi.org/10.1002/aisy.202200063>
- Girard, Tony. (1995). *Understanding Effective Bits, Application Note*. Signatec Corp Application Note AN95091. [Microsoft Word - Understanding Effective Bits.doc \(fastcomtec.com\)](https://www.fastcomtec.com/microsoft-word-understanding-effective-bits.doc)
- Goncu-Berk, G., & Tuna, B. G. (2021). The Effect of Sleeve Pattern and Fit on E-Textile Electromyography (EMG) Electrode Performance in Smart Clothing Design. *Sensors (Basel, Switzerland)*, 21(16), 5621. <https://doi.org/10.3390/s21165621>
- Hardwarebee. (2022, December 29). *Understanding charge pump*. Understanding Charge Pump.
<https://hardwarebee.com/charge-pump/>

- HSS Physicians. (2019). *Rotator cuff tears, injuries and treatments: HSS*. Hospital for Special Surgery. https://www.hss.edu/condition-list_rotator-cuff-injuries.asp
- IEEE Instrumentation and Measurement Society. (2011, January 14). *IEEE Standard for Terminology and Test Methods for Analog-to-Digital Converters*. IEEE Instrumentation and Measurement Society IEEE Std 1241-2010. [IEEE Std 1241™-2010, IEEE Standard for Terminology and Test Methods for Analog-to-Digital Converters \(iastate.edu\)](#)
- Jamaluddin, F. N., Ahamad, S. A., Mohd Noor, S. B., & Wan Hasan, W. Z. (2014). *Flexible bio-signals channels acquisition system for ECG and EMG Application*. 2014 IEEE Student Conference on Research and Development. Penang, Malaysia. <https://ieeexplore.ieee.org/abstract/document/7072996/>
- Johns Hopkins University, The Johns Hopkins Hospital, and Johns Hopkins Health System. (2021, August 8). *Electrocardiogram*. JHM. <https://www.hopkinsmedicine.org/health/treatment-tests-and-therapies/electrocardiogram>
- Johns Hopkins University, The Johns Hopkins Hospital, and Johns Hopkins Health System. (2023, April 24). *Electromyography (EMG)*. JHM. <https://www.hopkinsmedicine.org/health/treatment-tests-and-therapies/electromyography-emg>
- Klabunde, R.E. (2022, September 29). *Electrocardiogram Standard Limb Leads (Bipolar)*. Cardiovascular Physiology Concepts. [CV Physiology | Electrocardiogram Standard Limb Leads \(Bipolar\)](#)
- Kugelstadt, Thomas. (2003). Chapter 16. *Active Filter Design Techniques*. Op Amps for Everyone (Second Edition). <https://doi.org/10.1016/B978-075067701-1/50019-5>.
- Lee, S., & Kruse, J. (2008). Biopotential electrode sensors in ECG/EEG/EMG systems. *Analog Devices*, 200, 1-2.

Martinek R, Ladrova M, Sidikova M, Jaros R, Behbehani K, Kahankova R, Kawala-Sterniuk A. *Advanced Bioelectrical Signal Processing Methods: Past, Present, and Future Approach—Part III: Other Biosignals*. *Sensors*. 2021; 21(18):6064. <https://doi.org/10.3390/s21186064>

Maxim Integrated. (2019, June 24). *How to Calculate ENOB for ADC Dynamic Performance Measurement*. Maxim Integrated Application Note 6854. [App Note 6854: How to Calculate ENOB for ADC Dynamic Performance Measurement \(analog.com\)](#)

Mayfield Clinic. (2018, April). *Electromyography (EMG) & nerve conduction studies*. Electromyography (EMG) & Nerve Conduction Studies, Mayfield Brain & Spine Cincinnati, Ohio. <https://mayfieldclinic.com/pe-emg.htm#:~:text=An%20EMG%20FNCS%20is%20the,in%20the%20arms%20or%20legs.>

Mayo Clinic Staff. (2019, May 21). *Electromyography (EMG)*. Mayo Clinic. <https://www.mayoclinic.org/tests-procedures/emg/about/pac-20393913#:~:text=EMG%20results%20can%20reveal%20nerve,that%20cause%20muscles%20to%20contract.>

McManus, L., De Vito, G., & Lowery, M. M. (2020). Analysis and Biophysics of Surface EMG for Physiotherapists and Kinesiologists: Toward a Common Language With Rehabilitation Engineers. *Frontiers in neurology*, 11, 576729. <https://doi.org/10.3389/fneur.2020.576729>

MonolithicPower. (2022, July 6). *Operational Amplifiers*. Monolithic Power. [Operational Amplifier Basics, Types and Uses| Article | MPS \(monolithicpower.com\)](#)

Murthy, V. K., Grove, T. M., Harvey, G. A., & Haywood, L. J. (1978). Clinical Usefulness of ECG Frequency Spectrum Analysis. *Proceedings of the Annual Symposium on Computer Application in Medical Care*, 610–612.

- Ng, J. K., Kippers, V., & Richardson, C. A. (1998). Muscle fibre orientation of abdominal muscles and suggested surface EMG electrode positions. *Electromyography and clinical neurophysiology*, 38(1), 51–58.
- Nordic Semiconductor (2021, November 22) *nRF52840 Product Specification v1.7* (pp. 380-386). https://infocenter.nordicsemi.com/pdf/nRF52840_PS_v1.7.pdf
- Pahlm, O., Wagner, G.S. (2008, June 25). *Proximal Placement of Limb Electrodes: A Potential Solution for Acquiring Standard Electrocardiogram Waveforms from Monitoring Electrode Positions*. *Journal of Electrocardiology*. [Proximal placement of limb electrodes: a potential solution for acquiring standard electrocardiogram waveforms from monitoring electrode positions - ScienceDirect](https://doi.org/10.1016/j.jelectcard.2008.06.001)
- Power Stream. (2023). *PowerStream li-ion button cell LIR2450 Data Sheet*. Lithium ion Rechargeable (secondary) Coin Cells from PowerStream: Orem, Utah. <https://www.powerstream.com/p/Lir2450.pdf>
- Raez, M. B., Hussain, M. S., & Mohd-Yasin, F. (2006). Techniques of EMG signal analysis: detection, processing, classification and applications. *Biological procedures online*, 8, 11–35. <https://doi.org/10.1251/bpo115>
- Rathnapriya, S., Manikandan, V. *Remaining Useful Life Prediction of Analog Circuit Using Improved Unscented Particle Filter*. *J Electron Test* 36, 169–181 (2020). <https://doi.org/10.1007/s10836-020-05870-9>
- Roland, T., Amsuess, S., Russold, M. F., & Baumgartner, W. (2019). *Ultra-Low-Power Digital Filtering for Insulated EMG Sensing*. *Sensors* (Basel, Switzerland), 19(4). <https://doi.org/10.3390/s19040959>
- Silicon Labs. (2020, April 3) *Improving ADC Resolution by Oversampling and Averaging*. <https://www.silabs.com/documents/public/application-notes/an118.pdf>
- Song, M.-S., Kang, S.-G., Lee, K.-T., & Kim, J. (2019). *Wireless, Skin-Mountable EMG Sensor for Human–Machine Interface Application*. *Micromachines*, 10(12), 879. <https://doi.org/10.3390/mi10120879>

Spectra Symbol. (n.d). *Flex Sensor*. Spectra Symbol Data Sheet. [FLEX SENSOR DATA SHEET '10 \(SPARKFUN KIT\).ai \(adafruit.com\)](#)

Texas Instruments. (2020, April). *ADS129x Low-Power, 2-Channel, 24-Bit Analog Front-End for Biopotential Measurements*”, Texas Instruments Data Sheet. [ADS129x Low-Power, 2-Channel, 24-Bit Analog Front-End for Biopotential Measurements datasheet \(Rev. C\)](#)

Texas Instruments. (n.d.). *LM27762*. LM27762 data sheet, product information and support | TI.com. <https://www.ti.com/product/LM27762>

Varacallo, M., Bitar, Y. E., & Mair, S. D. (2023). *Comprehensive shoulder evaluation strategies - STATPEARLS - NCBI bookshelf*. Comprehensive Shoulder Evaluation Strategies. <https://www.ncbi.nlm.nih.gov/books/NBK538309/>